COMPREHENSIVE STUDY OF SIMPLIFIED MODELS FOR THERMAL SIZE EFFECTS INDUCED BY LOCALIZED HEATING IN CRYSTALLINE SOLIDS

by

Amir Abdolhosseinzadeh

B.S., Mechanical Engineering, University of Tabriz, 2016

M.S., Mechanical Engineering, K. N. Toosi University of Technology, 2019

Submitted to the Institute for Graduate Studies in
Science and Engineering in partial fulfillment of
the requirements for the degree of
Doctor of Philosophy

Graduate Program in Mechanical Engineering

Boğaziçi University

2025

ACKNOWLEDGEMENTS

I would like to express my deepest gratitude to all those who have supported me throughout the course of my doctoral research and made this thesis possible.

First and foremost, I would like to thank my supervisor, Assoc. Prof. Dr. Nazli Donmezer, for her guidance, support, and unwavering belief in my abilities. Her expertise, insightful feedback, and encouragement have been invaluable in shaping the direction and quality of my research.

I would also like to extend my thanks to the members of my dissertation committee, for their time, constructive suggestions, and commitment to improving my work.

I am profoundly grateful to my wife, Sahar, whose constant love, understanding, and unwavering support have been a foundation throughout this journey. Her patience, encouragement, and belief in me kept me going even during the toughest times. This achievement is as much hers as it is mine.

I am also deeply grateful to my family for their continuous support and encouragement. To my parents and my brother, thank you for your sacrifices, wisdom, and constant belief in my potential.

ABSTRACT

COMPREHENSIVE STUDY OF SIMPLIFIED MODELS FOR THERMAL SIZE EFFECTS INDUCED BY LOCALIZED HEATING IN CRYSTALLINE SOLIDS

High-performance nano- and microscale devices are increasingly used in advanced electronic and optical applications. The importance of accurate thermal characterization increases as their performance improves, mainly due to localized heating-induced size effects. These effects occur when the dimensions of the heated region approach the phonon mean free path, causing deviations from classical diffusive heat transport. Traditional Fourier-based models cannot adequately explain the thermal behavior under these conditions, necessitating phonon-based models, such as the solution of the phonon Boltzmann transport equation (BTE). In this thesis, we address the computational challenges of modeling thermal transport under localized heating using full Boltzmann Transport Equation (BTE), which is computationally intensive. A mesoscopic approach, such as that of Finite Volume Discrete Ordinates Method (FVDOM) and Kinetic Collective Model (KCM), is employed to evaluate their accuracy among other available methods like Monte Carlo (MC) and Lattice Boltzmann (LBM). Incorporating phonon properties from ab initio simulations further improves the accuracy of thermal predictions. KCM and gray FVDOM are compared for their capability to capture size-dependent heat transport and suitability for microscale applications. In addition, FVDOM is used to develop a semi-empirical correlation for the thermal spreading resistance, taking advantage of its numerical stability over mesh-sensitive models. Using a realistic heat generation profile in an AlGaN/GaN HEMT, we demonstrated the significance of non-diffusive transport and temperature-dependent material properties. It is evident from these findings that efficient mesoscopic models with physically accurate input are required for thermal design of advanced electronic devices.

ÖZET

KRISTAL YAPILARDA ISINMA ILE TETIKLENEN TERMAL BOYUT ETKILERI IÇIN BASITLEŞTIRILMIŞ MODELLERIN KAPSAMLI ÇALIŞMASI

Yüksek performanslı nano ve mikroskala cihazlar, gelişmiş elektronik ve optik uygulamalarda giderek daha fazla kullanılmaktadır. Bu cihazların artan performansı, özellikle yerel ısıtma kaynaklı termal boyut etkileri nedeniyle, hassas termal karakterizasyonu kritik hâle getirmektedir. Isıtılan bölgelerin boyutları fononların ortalama serbest yoluna yaklaştığında, klasik difüzyonel ısı iletimi yetersiz kalmakta ve fonon tabanlı modellere ihtiyaç duyulmaktadır. Bu çalışma, yerel ısıtma sonucu oluşan termal boyut etkilerini analiz etmek amacıyla, Fonon Boltzmann Taşıma Denklemi'nin (BTE) çözümüne dayalı Sonlu Hacim Ayrık Yönler Yöntemi (FVDOM) ile Kinetik Kolektif Model'i (KCM) temel almaktadır. FVDOM ve KCM kullanılarak, Monte Carlo yönteminin rastlantısallığından ve aşırı sadeleştirilmiş varsayımlarından kaçınılmış; daha deterministik ve hassas çözümler elde edilmiştir. Ab-initio hesaplamalarla fonon özellikleri yüksek doğrulukla belirlenmiş, termal analizlerin doğruluğunu artırmıştır. KCM ve gri FVDOM, mikroskala ısı taşınımının modellenmesindeki elde ettikleri ve fonon özelliklerinin elde edilmesine uygunlukları açısından karşılaştırılmıştır. FVDOM, ağ bağımlılığı daha düşük olduğu için, termal yayılma direncine yönelik yarı-ampirik bir korelasyon geliştirilmesinde tercih edilmiştir. Ayrıca, AlGaN/GaN HEMT cihazında yerel ısıtma etkileri, gerçek ısı üretim profilleri ile modellenmiştir. Son olarak, sıcaklığa bağlı fonon özelliklerinin KCM'ye entegre edilmesiyle modelleme doğruluğu artırılmıştır. Elde edilen bulgular, yayınımsal olmayan ısı taşınımı ve sıcaklığa bağlı malzeme özelliklerinin, yeni nesil mikroskala cihazların güvenilir termal tasarımı için temel olduğunu ortaya koymaktadır.

TABLE OF CONTENTS

ACKNOWLEDGEMENTS . . . iii
ABSTRACT . . . iv
ÖZET . . . v
LIST OF FIGURES . . . viii
LIST OF TABLES . . . xv
LIST OF SYMBOLS . . . xvi
LIST OF ACRONYMS/ABBREVIATIONS . . . xix
1. INTRODUCTION . . . 1
1.1. Thermal Size Effects . . . 1
1.2. Dominant Heat Carriers in Crystalline Lattices: Phonons . . . 4
1.3. Characterization of Thermal Size Effects . . . 8
1.3.1. Experimental Approaches . . . 8
1.3.2. Theoretical Approaches . . . 12
1.3.2.1. Atomistic Simulations . . . 13
1.3.2.2. Mesoscale Techniques . . . 14
1.4. Phonon Boltzmann Transport Equation . . . 16
2. MOTIVATION . . . 22
3. KINETIC COLLECTIVE MODEL . . . 24
3.1. Theory and Numerical Implementation . . . 24
3.2. Model Geometry and Material Properties . . . 27
3.2.1. Verification Study . . . 27
3.2.2. Validation Study . . . 29
3.3. Results . . . 30
3.3.1. Verification Study . . . 30
3.3.2. Validation Study . . . 32
3.4. Conclusion . . . 34
4. FINITE VOLUME DISCRETE ORDINATES METHOD . . . 36
4.1. FVDOM Approach and Numerical Implementation . . . 36

4.2. Assumptions in Deriving FVDOM vs. KCM from phonon BTE 39
4.3. FVDOM for Thin Film Materials: Validation Study 40
4.4. Model Geometry and Thermophysical Properties 42
4.5. Results 44
4.5.1. Case Study 1: $T_{top} = 310K$ 44
4.5.2. Case Study 2: Volumetric Heat Generation 45
4.6. Conclusion 47
5. THERMAL SPREADING RESISTANCE OF LOCALIZED HEATING . . . 49
5.1. Model Geometry and Thermophysical Properties 49
5.2. Results 50
5.3. Conclusion 57
6. APPLICATION TO REAL DEVICE 59
6.1. Model Geometry and Thermophysical Properties 59
6.2. Ab-initio Simulations 61
6.3. Results 65
6.3.1. KCM vs. FVDOM 65
6.3.2. KCM with Temperature Dependent Properties 70
6.4. Conclusion 72
7. CONCLUSIONS AND FUTURE RESEARCH 74
REFERENCES 77
APPENDIX A: NUMERICAL IMPLEMENTATION AND PARAMETERS . 90
APPENDIX B: PHONON THERMAL TRANSPORT PROPERTIES 108
APPENDIX C: COPYRIGHT PERMISSIONS 128

LIST OF FIGURES

Figure 1.1. The cross section of an operating AlGaN/GaN HEMT showing a thermal hotspot. Reprinted by permission from AIP Publishing [2]. License number: 6065431094328. 1

Figure 1.2. (a) The thermal conductivity of single-crystal silicon layers of varying thicknesses (b) Temperature distribution of AlGaN/GaN/Si HEMTs in the presence of hotspot formation. Reprinted by permission from AIP Publishing and Springer Nature [9, 10]. License number: 6066910392520-606691076076. 3

Figure 1.3. (a) Acoustic Phonon (In-phase motion) (b) Optical Phonon (Out-of-phase motion). 4

Figure 1.4. Phonon dispersion curve for a crystalline solid, showing acoustic and optical branches. Reprinted by permission from John Wiley and Sons [12]. License number: 6066990880399. 5

Figure 1.5. Phonon density of states ($g(\omega)$) for a typical crystalline material. Reprinted by permission from Springer Nature [13]. License number: 6066991079532. 5

Figure 1.6. An illustration of different scattering mechanisms for phonons. (a) Phonon-boundary scattering. (b) Phonon-impurity scattering. (c) Phonon–phonon scattering. Reprinted by permission from John Wiley and Sons [14]. License number: 6065440241489. 6

Figure 1.7. Silicon thin-film thickness-dependent nondimensional cross-plane thermal conductivity at 300 K, as determined by theoretical and experimental methods. Reprinted by permission from APS Publishing [15–18]. License number: RNP/25/JUL/093425. 8

Figure 1.8. Thin film thermal conductivity of Si obtained from theoretical approach, TDTR experiment and literature. Reprinted by permission from APS Publishing [25]. License number: RNP/25/JUL/093423. 9

Figure 1.9. Channel temperature rise for multi-finger MOSFET devices measured by Raman thermometry and simulations; insets show images of IR imaging [27]. 11

Figure 1.10. Computational methods for thermal characterization of materials based on length and time scale. 12

Figure 1.11. (a) The simulation domain in AEMD (b) Decay of the temperature profile in AEMD (c) The simulation domain in NEMD (d) Comparison of size-dependent thermal conductivity in AEMD and NEMD. Reprinted by permission from APS Publishing [30]. License number: RNP/25/JUL/093426. 13

Figure 1.12. Comparison of phase lag calculated with the phonon BTE and values obtained experimentally. Reprinted by permission from Elsevier publising [35]. License number: 6067040604423. 15

Figure 1.13. (a) Schematic of the thermal domain (b) Comparison of temperature profiles obtained by continuum scale electrothermal simulation and BTE models across the 2-DEG channel. Reprinted by permission from AIP Publishing [2]. License number: 6065431094328. . . 19

Figure 1.14. Stationary temperature profiles along the cross sections indicated in the top figures (a) Large circular heater at 200 K (b) Small circular heater at 200 K (c) Large circular heater at 100 K, and (d) Small linear heater at 200 K. Reprinted by permission from APS Publishing [59]. License number: RNP/25/JUL/093348. . . . 20

Figure 3.1. Geometry of the verification problem along with the boundary conditions and cutlines. 27

Figure 3.2. Schematic of the 2D model along with the boundary conditions used for investigating boundary-induced size effects. 30

Figure 3.3. Temperature distribution along the (a) Y-line and b) X-line obtained from KCM when Top boundary is set to 310 K. 31

Figure 3.4. Temperature distribution along the (a) Y-line and b) X-line obtained from KCM when heat flux boundary condition is applied. . 31

Figure 3.5. Temperature distribution along the (a) Y-line and b) X-line obtained from KCM when heat generation boundary condition is applied. 32

Figure 3.6. a) Temperature contour of KCM solution for 1 μm Si b) temperature profile along x direction obtained from KCM and Fourier solutions. 33

Figure 3.7. Non-dimensional thin film thermal conductivity of Si calculated from the current model validated by the DFT simulations of Zeng et al. [63]. 34

Figure 4.1. a) Spatial and (b) angular discretization of the phonon BTE by FVDOM. 37

Figure 4.2. Non-dimensional thin film thermal conductivity of Si obtained from the FVDOM and KCM models validated by the DFT simulations of Zeng et al. [63]. 42

Figure 4.3. Geometry of the performance study along with the boundary conditions and cutlines. 42

Figure 4.4. Temperature contours obtained for the temperature boundary condition using (a) Fourier and (b) KCM methods for the first case study. 44

Figure 4.5. Temperature distribution along the (a) Y-line and b) X-line obtained from KCM, Fourier, and FVDOM methods for the first case study. 45

Figure 4.6. Temperature contours obtained for the heat generation boundary condition from (a) Fourier and b) KCM methods for the second case study. 46

Figure 4.7. Temperature distribution along the (a) Y-line and b) X-line obtained from KCM, Fourier, and FVDOM methods for the second case study. 47

Figure 5.1. Volumetric self-heating and applied boundary conditions in the GaN domain. 49

Figure 5.2. Maximum BTE and Fourier temperature difference, varying with heating power with ($Kn_L = 0.4$, $Kn_t = 0.8$, $Kn_b = 10$). 51

Figure 5.3. Dimensionless temperature distribution along the vertical symmetry line obtained from current FVDOM and MC [69] methods ($Kn_L = 0.01$, $Kn_t = 0.2$, $Kn_a = 1$, $Kn_b = 10$). 52

Figure 5.4. a) Maximum dimensionless temperature wrt. film thickness ($Kn_L = Kn_a = 0.5$) b) Localized heating resistance wrt. domain length ($Kn_a = 1$, $Kn_b = 10$) obtained from the current FVDOM simulations. 55

Figure 5.5. Residual thermal spreading resistance varying with heat generation a) length ($Kn_b = 10$, $Kn_L = 0.01$) and b) Residual thermal spreading resistance varying with heat generation length for different heat generation thicknesses. 56

Figure 6.1. a) The schematic of the AlGaN/GaN HFET used for numerical simulations and b) simplified model. 60

Figure 6.2. Realistic heat distribution applied in simulation models. 61

Figure 6.3. Flowchart for calculating phonon thermal transport properties of Wurtzite GaN using DFT simulations. 62

Figure 6.4. Wurtzite GaN bulk thermal conductivity obtained from the present study and literature (Garg et al. [79] , Liu et al. [80] , Simon et al. [81]). 62

Figure 6.5. Wurtzite GaN nonlocal length as a function of temperature from ab-initio simulations. 63

Figure 6.6. Non-dimensional thin film thermal conductivity of Wurtzite GaN obtained from the KCM and FVDOM simulations validated by the FDTR results of Freedman et al. [82]. 64

Figure 6.7. Temperature contours obtained with the realistic heating profile from (a) FVDOM and b) KCM methods. 66

Figure 6.8. Temperature distribution along the (a) X-line and b) Y-line obtained from FVDOM and KCM methods. 67

Figure 6.9. Temperature contours obtained from KCM method with the realistic heating profile for (a) constant and b) temperature-dependent properties. 70

Figure 6.10. Temperature distribution along the (a) X-line and (b) Y-line obtained from KCM method for constant and temperature-dependent properties. 71

Figure A.1. COMSOL interface for implementing the equations of the KCM model. 92

Figure C.1. First page of copyright permission for Figure 1.1 and 1.13. 128

Figure C.2. Second page of copyright permission for Figure 1.1 and 1.13. . . . 129

Figure C.3. First page of copyright permission for Figure 1.2 (a). 130

Figure C.4. Second page of copyright permission for Figure 1.2 (a). 131

Figure C.5. First page of copyright permission for Figure 1.2 (b). 132

Figure C.6. Second page of copyright permission for Figure 1.2 (b). 133

Figure C.7. First page of copyright permission for Figure 1.4. 134

Figure C.8. Second page of copyright permission for Figure 1.4. 135

Figure C.9. First page of copyright permission for Figure 1.5. 136

Figure C.10. Second page of copyright permission for Figure 1.5. 137

Figure C.11. First page of copyright permission for Figure 1.6. 138

Figure C.12. Second page of copyright permission for Figure 1.6. 139

Figure C.13. Copyright permission for Figure 1.7. 140

Figure C.14. Copyright permission for Figure 1.8. 141

Figure C.15. Copyright permission for Figure 1.9. 142

Figure C.16. Copyright permission for Figure 1.11. 143

Figure C.17. First page of copyright permission for Figure 1.12. 144

Figure C.18. Second page of copyright permission for Figure 1.12. 145

Figure C.19. Copyright permission for Figure 1.14. 146

LIST OF TABLES

Table 1.1. Different experimental thermal characterization methods [28]. . . . 11

Table 3.1. Geometry characteristics for the large domain. 28

Table 3.2. Thermophysical properties used in FEM simulations. 29

Table 4.1. Geometry characteristics for the small domains. 43

Table 6.1. Thermophysical properties of GaN used for numerical simulations. 64

Table 6.2. Comparison of localized heating resistance obtained from FVDOM, Fourier simulations and semi-empirical relation. 69

Table A.1. Model geometry, material properties, and boundary conditions used for KCM verification simulations. 90

Table A.2. Model geometry, material properties, and boundary conditions used for KCM performance analysis. 90

Table A.3. Model geometry, material properties, and boundary conditions used for simulations of developing semi-empirical relation for localized heating resistance. 91

Table A.4. Model geometry, material properties, and boundary conditions used for real device simulation. 91

LIST OF SYMBOLS

a	Heat generation length
b	Heat generation thickness
C	Specific heat
$C(f_\lambda)$	Linearized collision operator
D_x	Heat generation length
D_y	Heat generation thickness
e_0	Equilibrium energy density
e	Energy density
e_i	Directional energy density
e_i^w	Directional energy density coming from west face
e_i^e	Directional energy density coming from east face
e_i^n	Directional energy density coming from north face
e_i^s	Directional energy density coming from south face
f	Phonon distribution function
f_λ^{eq}	Bose-Einstein distribution at local equilibrium
$g(\omega)$	Phonon denisty of states
$\overline{\overline{G}}_\lambda$	Weight function
k	Bulk thermal conductivity
$\overrightarrow{k}$	Wave vector
k_λ	Thermal conductivity of the λ mode
k_{kin}	Kinetic thermal conductivity
k_{coll}	Collective thermal conductivity
Kn	Knudsen number
Kn_L	Knudsen number along the domain length
Kn_t	Knudsen number along the domain thickness
Kn_a	Knudsen number along the heat generation length
Kn_b	Knudsen number along the heat generation thickness
L	Film thickness

$L \times t$	Rectangle heat generation area
l	Nonlocal length
L_x	Domain length
L_y	Domain thickness
P	Heating power
p	Proportion of phonons that undergo specular reflection
$\overrightarrow{p}$	Momentum density
q'''	Volumetric energy generation
$\dot{Q}$	Power dissipation density
$\overrightarrow{q}$	Heat flux
R	Thermal spreading resistance
R_F	Difussive thermal spreading resistance
$R_{1D,t}$	Thermal resistance of cross-plane ballistic effects
$R_{1D,0}$	1D diffusive thermal resistance
S_N	Quadrature set
S_i	Direction cosine
S_{ix}	x component of the direction cosine
S_{iy}	y component of the direction cosine
T_0	Initial temperature
$\Delta T_{\max}$	Maximum temperature difference
v	Phonon group velocity
$\overrightarrow{v}_\lambda$	Group velocity of the λ mode
α'	Nonlocal coefficient
$\hbar$	Reduced Planck constant
$\overrightarrow{\beta}_\lambda$	Weight function
$\overrightarrow{\gamma}_\lambda$	Weight function
θ	Dimensionless temperature
Λ	Phonon mean free path
$\overline{\overline{\Pi}}$	Flux of the crystal momentum
$\sum$	Switching factor

τ	Heat flux relaxation time
τ_c	Collective mean free time
ω_λ	Frequency of the λ mode
$\omega(\overrightarrow{k})$	Phonon dispersion relationship
ω	Frequency
$\Delta\Omega_i$	Solid angle associated with direction i

LIST OF ACRONYMS/ABBREVIATIONS

2DEG	Two Dimensional Electron Gas
AlGan/Gan	Aluminum Gallium Nitride / Gallium Nitride
BTE	Boltzmann Transport Equation
DOS	Density of States
DOM	Discrete Ordinate Method
FDTR	Frequency-Domain Thermoreflectance
FEM	Finite Element Method
FinFETs	Fin Field-Effect Transistors
FVDOM	Finite Volume Discrete Ordinates Method
GK	Galerkin
HEMTs	High Electron Mobility Transistors
KCM	Kinetic Collective Model
LBTE	Linearized Boltzmann Transport Equation
LUS	Linear Upwind Scheme
MC	Monte Carlo
MD	Molecular Dynamics
MFP	Mean Free Path
MFT	Mean Free Time
μ-TDTR	Micro-scale Time-Domain Thermoreflectance
NEGF	Non-Equilibrium Green's Function
QUICK	Quadratic Upwind Interpolation for Convective Kinematics
RTA	Relaxation Time Approximation
SMART	Sharp and Monotonic Algorithm for Realistic Transport
SThm	Scanning Thermal Microscopy
WBG	Wide Band Gap

1. INTRODUCTION

1.1. Thermal Size Effects

Rapid advancement of microfabrication technology has made it possible to mass-produce electronic devices with sub-micrometer features. As a result, microelectronic devices such as transistors, diodes, microprocessors, and solar cells have become integral parts of modern electronics [1]. The ever increasing miniaturization and performance increase of these devices leads to enhanced surface-volume ratios, modified heat-transfer pathways, reduced thermal performance, and even quantum effects. It is imperative to understand these effects to address the performance challenges in these devices. Among these, thermal effects is one of the most significant effect that can adversely affect the performance and reliability and should be given special attention especially for high power operations of devices.

Microelectronic devices generate varying levels of heat during operation, as shown in Figure 1.1 [2].

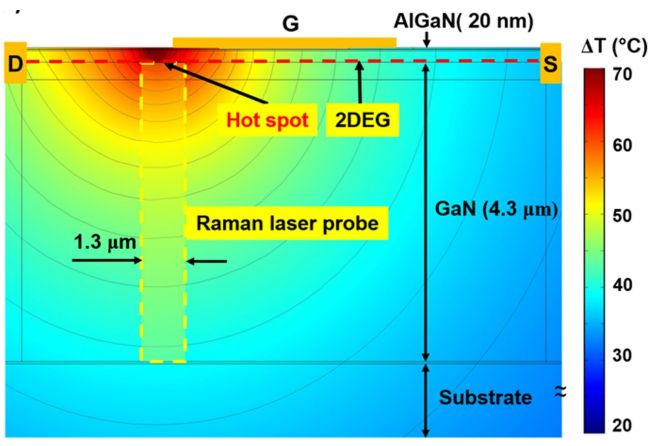

Figure 1.1. The cross section of an operating AlGaN/GaN HEMT showing a thermal hotspot. Reprinted by permission from AIP Publishing [2]. License number: 6065431094328.

Previous studies show that high temperatures reduce efficiency, increase failure rates, and shorten the useful life of devices. For instance, temperature and reliability are directly correlated in GaN devices [3]. In these devices, the mean time to failure decreases exponentially with temperature: approximately 6 million hours at $225°C$ and less than 1 million hours at $250°C$. These problems can be solved through effective thermal management of devices. The integration of heterogeneous devices, such as power electronics and LEDs, further complicates the thermal analysis. For example, in high-power LED arrays, thermal crosstalk can lead to deviations between the actual and measured junction temperatures, affecting performance and reliability [4].

To overcome these challenges, a holistic approach is required that incorporates accurate thermal modeling, transient behavior analysis, and physical design optimization [5]. The use of advanced cooling techniques, such as vapor chambers, microchannel cooling, and two-phase flow systems, offers promising solutions but introduces additional manufacturing and reliability concerns [5]. In the move to sub-five-nanometer nodes, advanced metrology, computational modeling, and material innovation become crucial to efficiently managing heat and ensuring the longevity of the device [5,6]. The design of a suitable thermal management method is possible with detailed thermal characterization of these devices with complex geometries and physics [5], [7].

In modern microelectronics, thermal characterization presents significant challenges due to the small dimension of the devices. In order to resolve temperature gradients across features smaller than 100 nm, micro-scale time-domain thermoreflectance (μ-TDTR) and scanning thermal microscopy (SThM) are essential [6]. However, these techniques do have some significant drawbacks such as expensive equipment, difficult setup requirements, and low resolution for deeply embedded layers. A viable alternative that allows for the predicted analysis of heat dispersion without the need for intrusive observations is thermal modeling. Modeling can successfully replicate thermal behavior in multilayered devices like as FinFETs (Fin Field-Effect Transistors), where complicated geometries make it challenging to detect heat generation and maximum temperatures. However, popular thermal modeling techniques based on classical

Fourier's law are not sufficient to characterize thermal transport in these devices due to presence of thermal size effects.

Microelectronic devices have features such as channel lengths, film thicknesses, and gate lengths, often below 100 nm. As these dimensions approach the mean free paths of the dominant heat carriers, typically 10 to 300 nm in silicon [8], thermal transport is slowed down. For example, the thermal conductivity can be reduced up to 70% in silicon layers thinner than 50 nm [8]. Additionally, physical phenomena like extremely localized hotspot formation due to Joule heating slows down the thermal transport. These effects, named thermal size effects, highlights the presence of non-continuum effects and thus deviation from classical heat conduction assumptions [6]. Figure 1.2a represents the reduced thermal conductivity of a silicon layer and how it changes with thickness, whereas Figure 1.2b demonstrates how hotspot formation in a typical GaN HEMT can increase the temperature as a result of self-heating effects [9, 10]. Future thermal models must account for these effects by understanding the transport physics of dominant heat carriers in device materials.

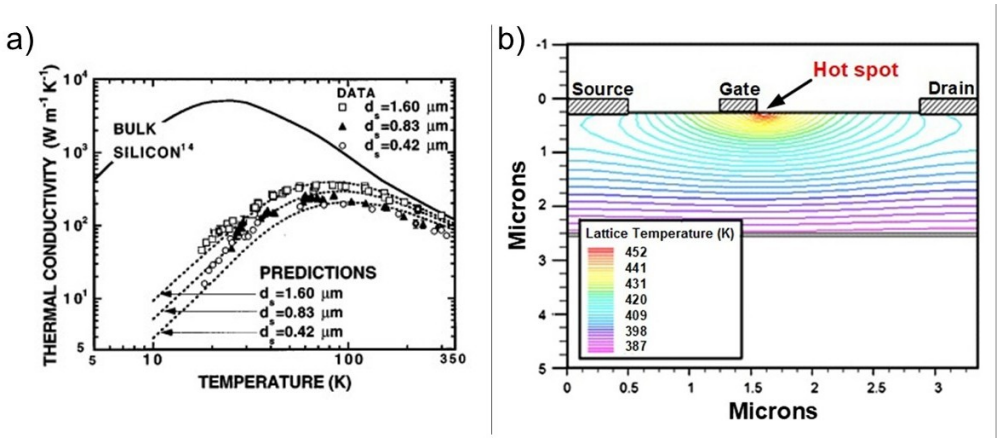

Figure 1.2. (a) The thermal conductivity of single-crystal silicon layers of varying thicknesses (b) Temperature distribution of AlGaN/GaN/Si HEMTs in the presence of hotspot formation. Reprinted by permission from AIP Publishing and Springer Nature [9, 10]. License number: 6066910392520-606691076076.

1.2. Dominant Heat Carriers in Crystalline Lattices: Phonons

In crystalline materials, the collective vibrations of atoms, called phonons, play a significant role in determining their thermal and mechanical properties. A phonon is the smallest unit of vibrational energy in a crystal lattice, representing a quantized mode of lattice vibration. Phonons fundamentally govern the thermal behavior of solid materials, dictating properties such as heat capacity, thermal conductivity, and thermal expansion [11]. These quantized lattice vibrations transmit energy through crystal structures via interactions with other phonons, defects, and material interfaces.

There are two types of phonons: acoustic and optical types based on their vibrational patterns. As shown in Figure 1.3a, atoms move unidirectionally in a one-dimensional lattice as a result of neighboring atoms vibrating in phase, facilitating the propagation of sound waves and heat through the lattice. Optical phonons, on the other hand, occur in lattices with multiple atoms per unit cell, in which neighboring atoms vibrate out of phase, as shown in Figure 1.3b, where the alternating atoms of a diatomic lattice move in opposite directions; induced electric dipoles can interact with electromagnetic waves, such as infrared light.

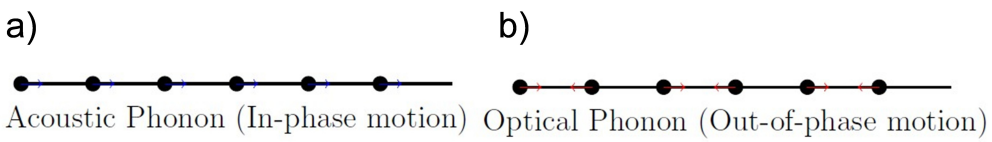

Figure 1.3. (a) Acoustic Phonon (In-phase motion) (b) Optical Phonon (Out-of-phase motion).

The phonon dispersion relates the frequency (ω) of phonons to their wave vector ($\vec{k}$). A typical phonon dispersion curve for a crystalline material is shown in Figure 1.4, emphasizing the difference between the acoustic and optical branches. Lower-frequency acoustic branches involve in-phase atomic vibrations, whereas higher-frequency optical branches involve out-of-phase vibrations in multi-atom unit cells [12]. Thermal properties such as heat capacity and conductivity are determined by the phonon dispersion

relation $\omega(\vec{k})$, where acoustic phonons exhibit linear dispersement near $\vec{k} = 0$, and optical phonons exhibit a finite frequency near $\vec{k} = 0$ [11].

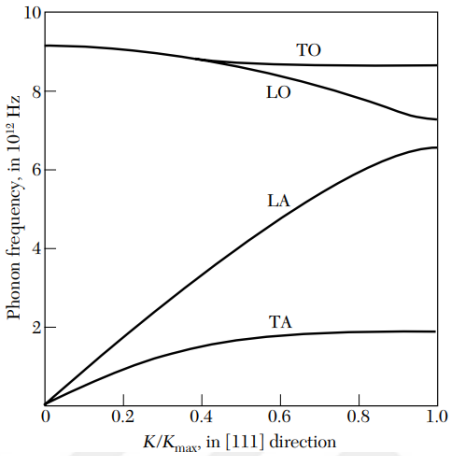

Figure 1.4. Phonon dispersion curve for a crystalline solid, showing acoustic and optical branches. Reprinted by permission from John Wiley and Sons [12]. License number: 6066990880399.

Phonon density of states (DOS), $g(\omega)$, quantifies the number of modes available at a given frequency as shown in Figure 1.5. It is also essential for understanding thermal transport and heat capacity in materials.

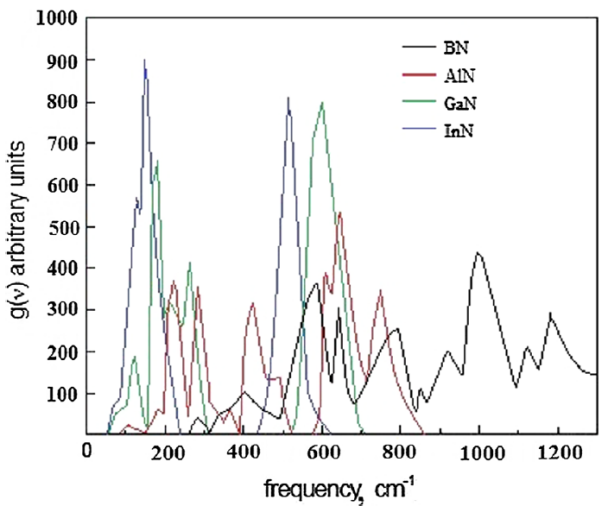

Figure 1.5. Phonon density of states ($g(\omega)$) for a typical crystalline material. Reprinted by permission from Springer Nature [13]. License number: 6066991079532.

Lifetime and energy transfer capacity of phonons are determined by their interactions with other phonons and energy carriers. Phonon relaxation is the decay of a phonon mode as a result of scattering events, such as phonon-phonon interactions, phonon-defect scattering, or phonon-boundary scattering, which determine the phonon mean free path (MFP) and relaxation time, τ. Phonon-phonon scattering can occur via fusion or fission events. In fission a high-energy phonon transfers its energy to two or more lower-energy phonons in order to conserve energy and momentum, whereas in fusion two or more phonons interact to generate a higher-energy phonon.

Different scattering mechanisms are shown in Figure 1.6 [14]. This figure shows that phonon-phonon scattering includes both normal and Umklapp processes. In normal scattering, the total crystal momentum is conserved within the first Brillouin zone, and although it redistributes phonons, it does not impede the overall heat flow. Umklapp scattering, on the other hand, has a momentum transfer that exceeds the Brillouin zone, causing phonon momentum to be reversed and thermal conductivity to be limited.

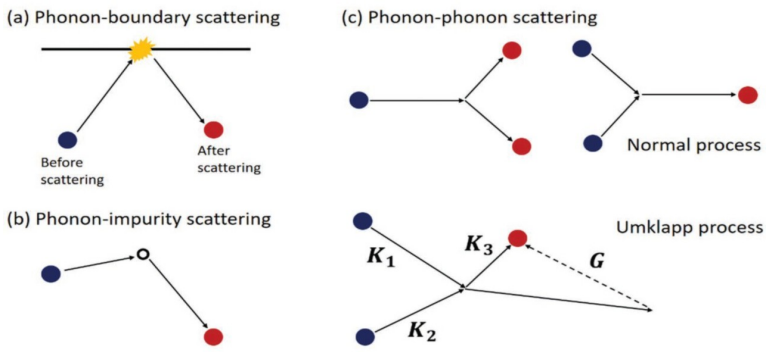

Figure 1.6. An illustration of different scattering mechanisms for phonons. (a) Phonon-boundary scattering. (b) Phonon-impurity scattering. (c) Phonon–phonon scattering. Reprinted by permission from John Wiley and Sons [14]. License number: 6065440241489.

The average time a phonon travels before a relaxation event is known as the phonon relaxation time, τ. The thermal transport properties of materials are determined by these phonon relaxation events. According to kinetic theory of phonons

thermal conductivity in crystalline materials is expressed as $\kappa = \frac{1}{3} C_v v_g^2 \tau$, where C_v is the volumetric heat capacity, v_g is the group velocity of phonons, and τ is the average phonon relaxation time. The average distance a phonon travels before a relaxation event is known as the phonon MFP, and it is defined as $\Lambda = v_g \tau$. In diffusive transport, phonons undergo frequent scattering events leading to a random walk-like energy transfer, typical in bulk materials at high temperatures. When uninterrupted, the energy transport and relaxation events of the phonons lead to the bulk thermal properties of the material.

When the movement of phonons are affected by physical barriers, other energy carriers, or defects thermal properties of the materials significantly changes. Since phonons can not relax effectively through interactions with other phonons they start showing ballistic behavior. In a thin film with a thickness less than the phonon MFP thermal conductivity is significantly affected due to these ballistic effects and scattering at the boundaries [12, 13]. Figure 1.7 shows the silicon thin film's thickness-dependent nondimensional cross-plane thermal conductivity as determined by experimental and numerical techniques [15–18].

Another example where phonon-phonon relaxation is interrupted is localized hotspots. In these regions diffusive thermal transport of phonons is significantly altered with continuous energy addition to phonons in a small region. IBM researchers observed temperatures exceeding 1050 K in graphene devices subjected to electrical stress, with metallic electrodes acting as heat sinks [19]. Using continuum models, factors such as ballistic phonon transport, mode-specific phonon relaxation, and temperature-dependent degradation of thermal conductivity are not taken into account, leading to an underestimate of highly localized temperatures, such as 1050 K observed experimentally in graphene devices. In another example a GaN-based HEMT, for instance, experiences severe thermal degradation under ballistic transport regimes, where phonon MFPs exceed hotspot dimensions [20]. According to recent studies, even 100-nanometer hotspots can significantly affect local thermal resistance, accelerating device failure [21, 22].

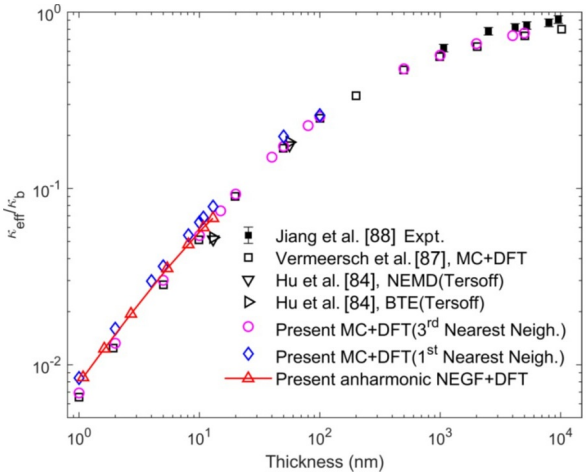

Figure 1.7. Silicon thin-film thickness-dependent nondimensional cross-plane thermal conductivity at 300 K, as determined by theoretical and experimental methods. Reprinted by permission from APS Publishing [15–18]. License number: RNP/25/JUL/093425.

To address the thermal problems associated with new generation electronic devices and extend their lifespan, the thermal transport regimes (either ballistic or diffusive) in different regions of the devices needs to be determined. Knudsen number ($Kn = \frac{\Lambda}{L}$), derived by comparing MFP (Λ) to characteristic length (i.e. film thickness, hotspot size etc.) (L), is an important parameter for identifying heat transfer regimes—differentiating between diffusive ($Kn \ll 1$) and ballistic ($Kn \gg 1$) phonon transport [23]. Theoretical models and experimental techniques can be used to analyze the existence and magnitude of thermal size effects. In the following section, we provide an overview of these methods, highlighting their key principles, advantages, and limitations.

1.3. Characterization of Thermal Size Effects

1.3.1. Experimental Approaches

A range of advanced experimental methods are used to characterize the thermal size effects. These include of infrared (IR) thermography, time-domain thermoreflectance (TDTR), frequency-domain thermoreflectance (FDTR), micro-Raman spec-

troscopy, and the 3ω technique. Each technique has specific advantages in terms of resolution, material suitability, and its ability to capture localized heating effects.

Pump-probe techniques, such as TDTR and FDTR use two laser pulses: a pump pulse to heat the sample and a probe pulse to monitor its time-dependent response. Thermophysical properties like thermal conductivity, thermal diffusivity, and interface thermal resistance are measured using these techniques. TDTR uses reflectance variations to precisely examine thermal properties. With a temporal resolution of picoseconds and a spatial resolution of $\sim$1 μm, it is especially useful for characterizing interfaces and multilayers. Figure 1.8 illustrates the reduced thermal conductivity of silicon thin films as determined by TDTR measurements and theoretical calculations, due to thermal size effects. FDTR using modulated lasers to work with complicated materials was used to analyze the thermal characteristics of a 100 nm layer of aluminum oxide [24].

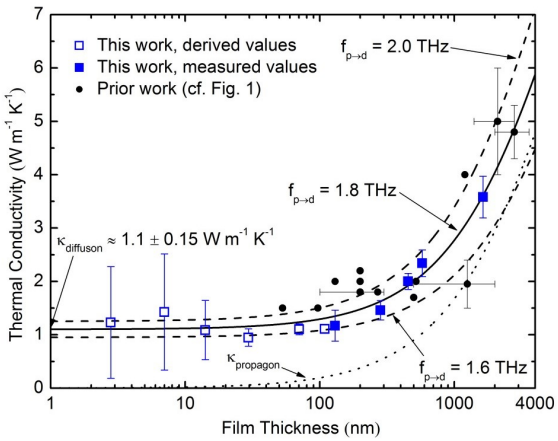

Figure 1.8. Thin film thermal conductivity of Si obtained from theoretical approach, TDTR experiment and literature. Reprinted by permission from APS Publishing [25]. License number: RNP/25/JUL/093423.

The 3ω method measures the thermal conductivity by passing an alternating current through a metal line that serves both as a heater and thermometer. In thin films and dielectrics, where phonon-boundary scattering may significantly decrease thermal conductivity, this method works especially well. For example, in silicon thin

films (20 nm to 1 μm), the 3ω technique has showed lower thermal conductivity due to boundary scattering [26]. However, its ability to probe the temperature of highly localized hotspots is limited, as its spatial resolution is approximately 10 μm, which may be insufficient to capture fine-scale thermal variations in micro- and nanoscale regions.

In the micro-Raman spectroscopy system, sample is excited by a Raman laser on a substrate. A spectrometer then analyzes the scattered light to determine the temperature reduction of the measured location. This temperature rise can be used to obtain the thermal conductivity of the specimen or the temperature rise due to thermal size effects, depending on the nature of equipment. Although this method works best with materials that are Raman-active, it may be constrained by the requirement for particular optical characteristics.

Finally infrared (IR) thermography as shown in Figure 1.9, which provides non-contact temperature mapping with a resolution usually in the a few micrometer range. IR thermography complements existing methods for examining thermal size effects in materials under localized heating because it is useful for larger-scale samples and allows for the real-time visualization of thermal gradients. Looking at the Figure 1.9, temperature rise at the hotspot of a metal–oxide–semiconductor field-effect transistor (MOSFET) was evaluated and compared using three methods—Raman thermometry, a theoretical thermal model, and infrared thermography—to assess their accuracy and consistency in characterizing localized heating [27]. The results reveal each method's strengths and limitations for capturing thermal size effects in microelectronics.

The material and the type of thermal size effects under investigation determine the technique to be used. Because of electrical interference, the 3ω technique performs poorly on conductors but well on thin films and dielectrics. For Raman-active materials, Micro-Raman provides high-resolution temperature mapping, whereas IR thermography allows more comprehensive temperature mapping across wider regions. With FDTR being easier to set up and TDTR providing better temporal resolution,

both are perfect for interfaces and multilayers. These methods can be used to investigate thermal size effects, such as boundary scattering or phonon confinement, which intensify under localized heating conditions.

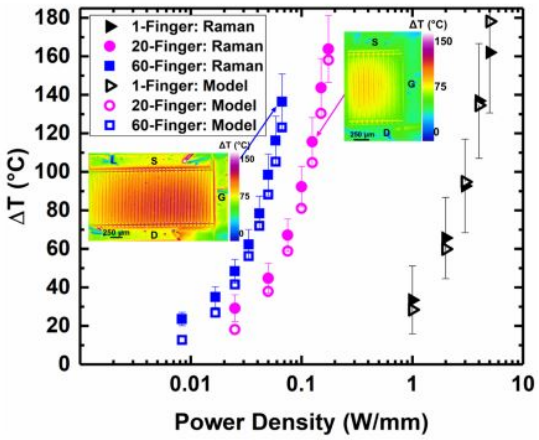

Figure 1.9. Channel temperature rise for multi-finger MOSFET devices measured by Raman thermometry and simulations; insets show images of IR imaging [27].

Table 1.1 compares experimental techniques for thermal characterization by resolution and material suitability. Since experiments are limited in feasibility and resolution, theoretical approaches are essential for predicting thermal properties and providing microscopic insight into phonon-phonon scattering, including normal and Umklapp processes.

Table 1.1. Different experimental thermal characterization methods [28].

Technique	**Resolution**	**Suitable Materials**
3ω	$\sim$10 μm	Thin films, dielectrics
Micro-Raman	$\sim$1 μm	2D materials
IR Thermography	$\sim$5 μm	Bulk materials, composites
TDTR	$\sim$1 μm	Multilayers, metals
FDTR	$\sim$1 μm	Thin films, composites

1.3.2. Theoretical Approaches

Thermal characterization using theoretical methods in the ballistic regime allows us to analyze size-dependent thermal properties without requiring complex experimental setups. Figure 1.10 shows a hierarchical framework of simulation techniques that spans broad spatial and temporal scales, emphasizing how many approaches are positioned within this multiscale environment.

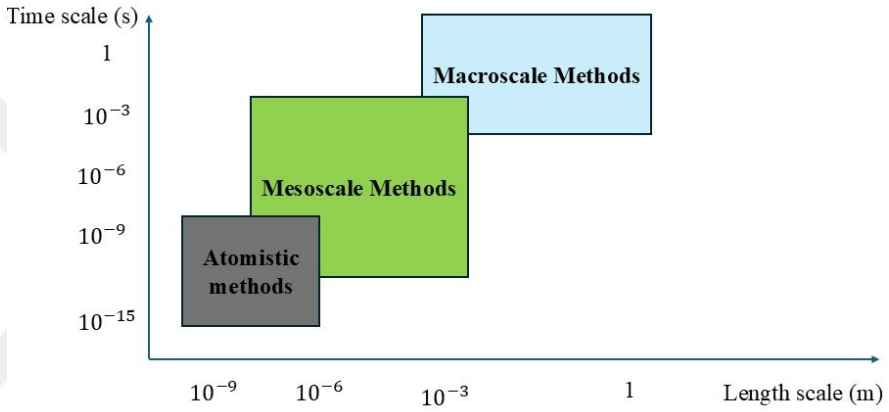

Figure 1.10. Computational methods for thermal characterization of materials based on length and time scale.

According to this figure there are two major categories into which microscopic modeling approaches for heat transfer can be typically classified: atomistic (which includes ab-initio, non-equilibirium green's function, molecular dynamics) and mesoscale (numerical solution of simplified Boltzmann transport equation). When choosing a phonon transport modeling strategy, it is important to consider accuracy, computational efficiency, and system-specific applicability, especially when comparing atomistic and mesoscale methods.

The next section discusses atomistic and mesoscale modeling approaches in detail, outlining their underlying principles, typical applications, and the specific advantages they offer for thermal characterization, as well as the limitations and challenges associated with each method.

1.3.2.1. Atomistic Simulations. An atomistic simulation is a simulation in which the atomic-scale interactions and dynamics are explicitly considered, such as ab-initio methods, non-equilibrium Green's function (NEGF), and molecular dynamics (MD), providing detailed insights into heat conduction mechanisms at the atomic level. Size effects such as phonon-boundary scattering are captured by MD employing equilibrium (EMD) or non-equilibrium (NEMD) techniques for thin films and nanowires [29]. Whereas NEMD uses temperature gradients to calculate thermal conductivity, EMD uses the Green-Kubo method. The approach-to-equilibrium molecular dynamics (AEMD) method results from Sheng et al. [30] are shown in Figure 1.11 to demonstrate how molecular dynamics simulations may capture transient and size-dependent heat transfer at the nanoscale. Using this method, the simulation domain is first separated into hot and cold areas, then thermal conductivity is extracted by tracking the temperature relaxation that follows. The figure illustrates the significant impact of system length and the shift from ballistic to diffusive heat transport regimes by comparing the temperature evolution and size-dependent thermal conductivity derived from AEMD and steady-state NEMD simulations.

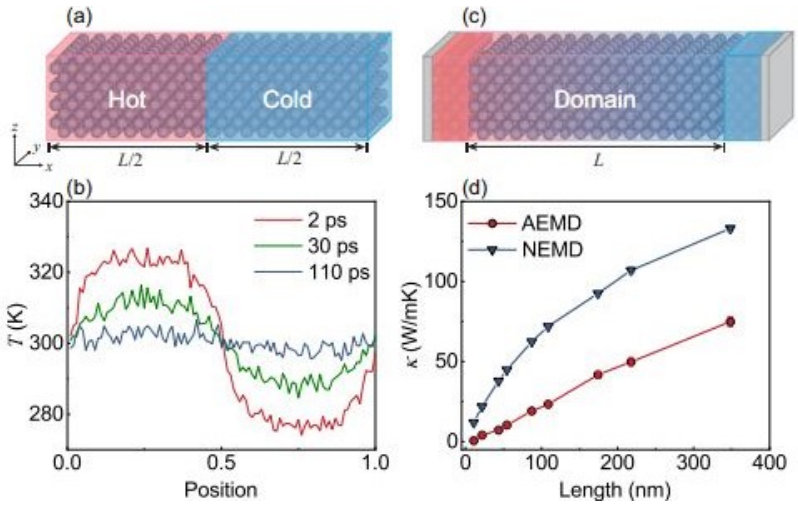

Figure 1.11. (a) The simulation domain in AEMD (b) Decay of the temperature profile in AEMD (c) The simulation domain in NEMD (d) Comparison of size-dependent thermal conductivity in AEMD and NEMD. Reprinted by permission from APS Publishing [30]. License number: RNP/25/JUL/093426.

Ballistic transport and interface effects are simulated using NEGF method and the scattering matrix approach, which are appropriate for materials such as graphene and Si/Ge superlattices [31, 32]. By capturing nanoscale heat flow and interfacial scattering, these methods provide a more accurate representation of thermal transport in systems where classical diffusive models break down, allowing for better prediction of device performance under extreme conditions.

Without the need for experimental settings, NEMD and NEGF are able to capture non-equilibrium temperature distributions and ballistic effects in localized heating scenarios, such as hot spots in nanostructures. However, NEGF and scattering matrix approaches are restricted to extremely tiny domains, while MD necessitates precise interatomic potentials. Density Functional Theory (DFT) cannot be used to model localized heating because of its computational cost, small system size limits, and equilibrium assumptions. Although DFT provides information that can be used in other methods, it cannot handle the non-equilibrium, nanoscale dynamics associated with localized thermal processes. Therefore, MD and NEGF are more practical despite their respective limitations.

1.3.2.2. Mesoscale Techniques. A mesoscale theoretical approach bridges atomistic and continuum models to study complex microstructures and heterogeneous materials, balancing accuracy and computational efficiency at nanometer-to-micrometer scales. For thermal conductivity (κ) in thin films or nanowires (e.g., silicon), the Boltzmann Transport Equation (BTE) models phonon transport, accounting for scattering mechanisms [33]. BTE effectively captures ballistic-diffusive regimes and size effects in systems from 100 nm to millimeters, especially with recent machine learning enhancements for faster phonon predictions [34]. It can be solved numerically or with the relaxation time approximation (RTA), which captures thermal conductivity reduction in nanoscale systems, such as 50 nm-diameter nanowires.

A direct comparison of phonon BTE simulations with experimental phase lag data collected from FDTR measurements on silicon (Figure 1.12) shows strong agreement

[35]. Experimental results (black circles) match BTE predictions using both Broido and Holland models, whereas simulations excluding optical phonons systematically deviate, emphasizing the importance of accurate scattering mechanisms and phonon properties. Based on this agreement across a broad range of modulation frequencies, the BTE approach can be used to model microscale, non-diffusive thermal transport in silicon.

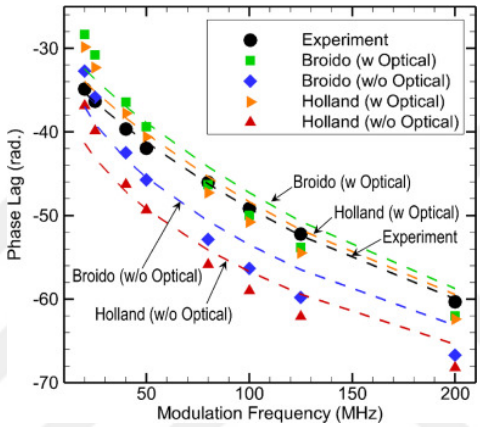

Figure 1.12. Comparison of phase lag calculated with the phonon BTE and values obtained experimentally. Reprinted by permission from Elsevier publising [35]. License number: 6067040604423.

The dielectric continuum model provides computational efficiency for micrometer-scale systems by treating materials as continua with effective thermal characteristics and estimating κ in thin films (such as polymers) by solving heat conduction equations with ballistic corrections [36]. For the second group of modeling approaches, TTM simulates electron-phonon relaxation in metals under ultrafast heating, addressing size-dependent relaxation times, while the BTE models heat dissipation from localized sources (e.g., a laser spot in a silicon film), capturing non-equilibrium dynamics and size effects [37]. Heat flow from a hot spot in a microelectronic device is modeled using Finite Element Methods (FEM), which incorporate size-dependent features by solving heat conduction equations.

Atomistic techniques like as MD are computationally demanding and can only be used on tiny systems (1–10 nm), despite offering high-fidelity details at the nanoscale.

The accuracy of BTE is higher than that of the dielectric continuum model, which sacrifices precision in favor of phenomenological simplicity, and Two-Temperature Model (TTM), which is less effective for insulators because it depends on electron-phonon coupling. However, BTE requires phonon properties from ab-initio or experimental data. Experimental studies on size effects have validated the effectiveness of multiscale methods, which bridge these scales by combining mesoscale models like BTE or FEM with atomistic inputs (e.g., from Ab-initio).

Multiscale approaches integrating BTE with atomistic inputs are recommended for their ability to balance accuracy and scalability while addressing complex nanoscale interactions. Multiscale BTE-based models will likely dominate as computational power and machine learning tools improve, supported by their increasing use in semiconductor nanostructure studies and experimental validation of thermal transport. Because of its listed capabilities this thesis concentrates on the challenges and advances in phonon Boltzmann Transport Equation solution to characterize thermal size effects. Theory of phonon Boltzmann Transport Equation is discussed in further detail in the next section.

1.4. Phonon Boltzmann Transport Equation

Phonon BTE describes the dynamics of phonons. By solving phonon BTE, we can study how phonons propagate and scatter within a material and get insights into its thermal behavior. The BTE allows the analysis of key thermal properties such as thermal conductivity and thermal resistance by accounting for scattering mechanisms, including phonon-phonon interactions, phonon-electron interactions, and boundary scattering. As an expression of the phonon BTE, the phonon distribution function (f) [38],

$$\frac{\partial f}{\partial t} + \overrightarrow{v} \cdot \nabla f = \left[\frac{\partial f}{\partial t}\right]_{scatt} + q^{'''}, \tag{1.1}$$

describes the statistical occupancy of phonon states, capturing how phonons propagate, scatter, and interact within a material under non-equilibrium conditions. The phonon distribution function and phonon group velocity are represented by f and v in this equation. The volumetric energy generation is expressed by $q^{'''}$ if any. On the right-

hand side, the scattering term accounts for changes in the distribution function caused by collisions between phonons, isotopes, electrons, crystal defects, and boundaries. The distribution function f is affected by the position, direction, frequency, and polarization of the phonons.

The complexity of the BTE makes it difficult to obtain exact analytical solutions. Generally, analytical approaches are limited to simplified cases or specific approximations, such as the relaxation time approximation, and provide solutions only for certain geometries and boundary conditions. To solve the BTE directly, various approximations and efficient numerical methods have been developed. In the past, these approximations have been applied to semiconductor thermal modeling [39, 40]. The phonon Boltzmann transport equation can be solved using techniques including Monte Carlo (MC), Finite Volume Discrete Ordinates Method (FVDOM) and Kinetic Collective Model (KCM).

The MC solution of the phonon BTE is a stochastic computational technique that predicts thermal conductivity and heat flow in materials by simulating phonon transport following the random trajectories and scattering events of individual phonons. Peterson [41], Mazumder and Majumdar [42], Wong et al. [43], Wang and Murthy [44], Mittal [45,46], and Shao et al. [47] suggest MC thermal simulations of nanoscale devices are more flexible and cost-effective than direct quantum simulations. Recently, hybrid Monte Carlo-diffusion simulations were used to examine the thermal spreading resistance (a resistance to heat flow arises when heat spreads from a small area to a larger one due to geometric mismatch) in GaN HEMTs under localized heating, capturing the ballistic-diffusive heat transport influenced by substrate thickness and heat source dimensions [48, 49]. Although these models are primarily based on surface heat flux conditions, they highlight the need to extend the approach to localized volumetric heat generation in order to obtain more accurate thermal predictions. Meanwhile, statistical noise, the use of random number generation, and simplistic assumptions are limitations of MC simulations that might lower their accuracy when simulating complex thermal transport [50].

FVDOM uses a different methodology to solve the phonon BTE by discretizing the angular space of phonons into specific directions. This provides insight into the directional dependence of thermal conductivity and phonon transport properties. Developed by Chandrasekhar [51] for neutron transport and later refined by Lathrop and Carlson [52], FVDOM has since been applied to radiative heat transfer [53, 54] and phonon transport [55].

With a symmetric AlGaN/GaN high-electron-mobility transistor (HEMT), Chatterjee et al. studied the effect of electrical bias and subcontinuum thermal transport [2]. A three-dimensional electrothermal model incorporating ballistic-diffusive thermal transport at subcontinuum levels was used to conduct thermal imaging. Under two different gray assumptions for the phonon MFP, the temperature distribution for the BTE domain in Figure 1.13a was solved using the phonon group velocity, specific heat, and relaxation time. Figure 1.13b illustrates the temperature distributions. Combined approaches indicate that heat localization and subcontinuum-level thermal conduction are interconnected, and channel temperature cannot be calculated solely using continuum principles. These findings underscore the importance of considering nanoscale transport effects when designing high-power HEMTs. Accurately capturing such phenomena is essential for predicting device reliability and optimizing thermal management strategies.

The typical use of simple assumptions, such as the gray approximation for phonon mean free paths, which ignores the full spectrum and polarization dependence of phonon transport, is the limitation of FVDOM. This simplification represents a significant gap in the literature, especially when it comes to simulating non-equilibrium processes and localized heating in nanoscale devices. By integrating ab-initio simulations with FVDOM, we overcome this constraint in our study and allow accurate, mode-resolved phonon parameters, including relaxation times, group velocity, and specific heat, to be directly integrated into the FVDOM framework. When simulating complex heat transport events outside of the gray approximation, this integration improves FVDOM's physical fidelity and predictive accuracy.

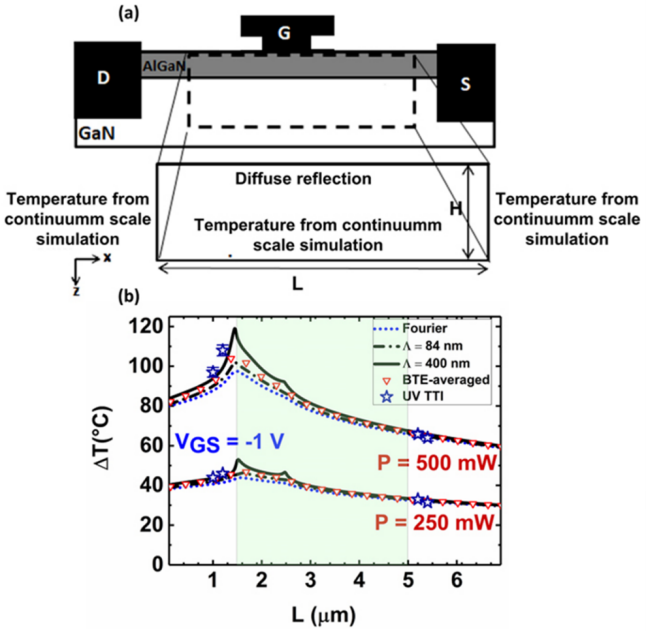

Figure 1.13. (a) Schematic of the thermal domain (b) Comparison of temperature profiles obtained by continuum scale electrothermal simulation and BTE models across the 2-DEG channel. Reprinted by permission from AIP Publishing [2]. License number: 6065431094328.

KCM introduced in 2014 by de Tomas et al. simplifies the linearized BTE and extends Fourier's law [56, 57] by including memory and non-local effects into heat transport at small spatial and temporal scales. KCM aims to unify two perspectives: microscopic phonon behavior, where they move and interact independently with boundaries, and macroscopic interactions, where heat flows mimic hydrodynamic flow. KCM consists of normal (N) and resistive (R) collision operators ($C = N + R$), which are used to calculate the scattering matrix [58].

In the past KCM framework was used to study Non-diffusive thermal transport in silicon between 100 and 300 K [59] as shown in Figures 1.14a-d. According to their results, significant deviations from Fourier's law depend on both size and geometry.

A review of earlier research on the solution of phonon BTE using the KCM method shows an important gap in the scenarios with the heat generation, especially for localized heating in nanoscale devices, which our study attempts to fill. KCM

avoids stochastic variability and computationally demanding sampling of MC while offering accuracy comparable to FVDOM for some material systems. This is achieved by simulating both kinetic and collective phonon-transport regimes, offering a balance between computational efficiency and accuracy. However, KCM accuracy is strongly dependent on exact input parameters, including phonon dispersion relations, and may not be as reliable as FVDOM in complicated geometries or highly anisotropic materials where accurate phonon scattering mechanisms are essential.

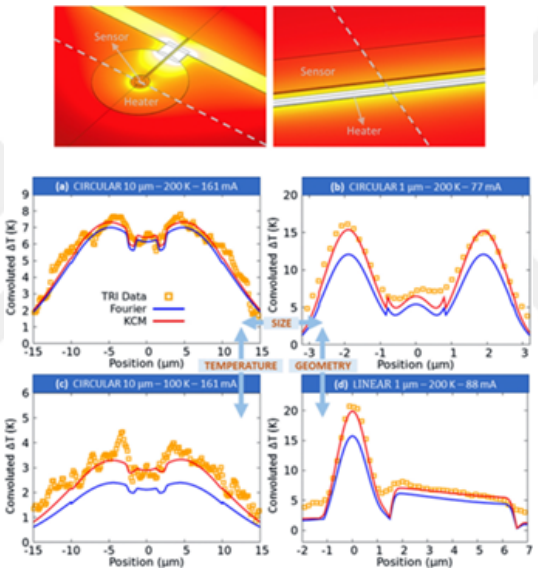

Figure 1.14. Stationary temperature profiles along the cross sections indicated in the top figures (a) Large circular heater at 200 K (b) Small circular heater at 200 K (c) Large circular heater at 100 K, and (d) Small linear heater at 200 K. Reprinted by permission from APS Publishing [59]. License number: RNP/25/JUL/093348.

For semiconductor thermal modeling, KCM and FVDOM are more widely used and user-friendly due to their computational efficiency, ease of implementation, and superior ability to handle complex boundary conditions and capture collective phonon transport effects. However, although being flexible and cost-effective for nanoscale devices, MC simulations' reliance on stochastic processes necessitates careful convergence checks and may produce less stable results, which restricts their applicability to routine engineering applications.

Currently, there is a lack of comprehensive studies on simulating thermal size effects caused by localized heating using the KCM method, which leaves a critical gap in understanding collective phonon dynamics in such conditions. Furthermore, FVDOM frequently relies on inconsistent phonon properties, making it unreliable for predicting nanoscale thermal transport. Finally, thermal spreading resistance models are typically based on heat flux boundary conditions and do not account for the heat generation scenarios common in modern devices. To fill these gaps, this research applies KCM to localized heating scenarios, optimizes phonon property inputs for accurate FVDOM simulations, and extends semi-empirical relation for thermal spreading resistance that takes into consideration localized volumetric heat generation under thermal size effects. This will result in a set of efficient, practical tools for predicting thermal size effects without the need for expensive simulations.

2. MOTIVATION

Modern electronics face significant challenges in managing heat due to the rapid reduction in device size and the increase in power densities. At micro- and nanoscales, thermal size effects cause transport to deviate from continuum predictions, impacting performance and reliability. Designing thermally efficient electronic devices requires accurate modeling of these phenomena. Due to the multiscale and multiphysics nature of this problem, full-scale simulations using first-principles or detailed numerical methods are computationally infeasible for regular design. Simplified models are efficient but their accuracy, especially for localized volumetric heating, is poorly documented.

The goal of this thesis is to find an accurate simple method to estimate the thermal size effects caused by localized heating resistance in electronic devices. Such a technique would enhance thermal design procedures in both industry and academia by lowering simulation complexity and costs. To achieve this, we study the common mesoscale models, KCM and FVDOM, and compare them with each other.

The following are the specific objectives of this study:

- Extending the KCM method to address problems involving localized volumetric heating.
- Performance analysis of the KCM method and compare it with the FVDOM solution.
- Investigate and suggest the most suitable thermal properties to be used in these simulations.
- Suggest a semi-empirical relationship to quantify the extent of the thermal size effects.

The accuracy of KCM and FVDOM is assessed in Chapters 3 and 4 using numerical simulations, and strategies for improving model performance are discussed.

The concept of thermal spreading resistance is introduced in Chapter 5, where a semi-empirical formula is proposed to quantify localized heating resistance. The numerical method and semi-empirical relation are used in Chapter 6 for realistic simulations of GaN HEMT, incorporating temperature-dependent phonon properties from first-principles calculations to improve simulation accuracy.

3. KINETIC COLLECTIVE MODEL

The KCM provides a potential framework for investigating thermal size effects since it addresses heat tranport at the nanoscale and successfully combines kinetic and collective phonon transport mechanisms. In this chapter, we build a thermal model to investigate thermal size effects caused by localized heating using KCM. To test the accuracy of the model we compare the results for a common device with Fourier. However, since Fourier's solution models only diffusive transport, only cases without size effects from localized heating are considered for accurate comparison. We do this by analyzing a sufficiently large domain where size effects due to localized heating and boundary scattering are negligible. Meanwhile, the validity of KCM for thin film thermal conductivity prediction is also evaluated by comparing it to a more accurate theoretical approach. The KCM approach will be discussed in the section that follows, along with details of the simulation processes, governing equations, and numerical solutions.

3.1. Theory and Numerical Implementation

KCM divides thermal conductivity into two distinct regimes: kinetic and collective. The kinetic conductivity is determined by the contributions of each phonon independently, whereas collective conductivity is determined by the interactions of all phonons together. This model provides a valuable approach for studying thermal transport in real-world materials by integrating individual phonon behavior and collective interactions [60]. Collective behavior emerges from the coupling of modes driven by N processes, resulting in R collisions between phonons of different modes. Therefore, all modes have the same collision mean free time (MFT), referred to as the collective MFT, τ_c.

The transition between these regimes is governed by a switching factor $\sum \in [0, 1]$, which quantifies the relative dominance of normal versus resistive (Umklapp + impurity

+ boundary) scattering. To rigorously understand how both kinetic and collective contributions to thermal conductivity emerge in real materials, it is essential to return to the microscopic foundations of heat transport. This begins with the phonon BTE equation, from which a hydrodynamic heat equation—analogous to the Navier-Stokes equation—can be systematically derived.

To derive the hydrodynamic heat equation, we begin with the linearized BTE, which governs the evolution of the nonequilibrium phonon distribution function under external perturbations as [61]

$$\frac{\partial f_\lambda}{\partial t} + \overrightarrow{v}_\lambda \cdot \overrightarrow{\nabla} f_\lambda = C(f_\lambda) \tag{3.1}$$

where $\overrightarrow{v}_\lambda$ is the group velocity of the λ-phonon mode (wave vector $\overrightarrow{k}$ and polarization s) and $C(f_\lambda)$ is the linearized collision operator acting on the distribution function. By multiplying Eq 3.1 by $\hbar\omega_\lambda$ (phonon energy) and $\hbar k_\lambda$ (phonon momentum), we can obtain the transport equations for energy and momentum given by

$$\frac{\partial e}{\partial t} + \overrightarrow{\nabla} \cdot \overrightarrow{q} = 0, \tag{3.2}$$

$$\frac{\partial \overrightarrow{p}}{\partial t} + \overrightarrow{\nabla} \cdot \overline{\overline{\Pi}} = \int \hbar \overrightarrow{k}_\lambda C(f_\lambda)\, d\lambda \tag{3.3}$$

in which $e = \int \hbar\omega_\lambda f_\lambda d\lambda$ is energy density, $\overrightarrow{q} = \int \hbar\omega_\lambda \overrightarrow{v}_\lambda f_\lambda d\lambda$ is the heat flux, $\overrightarrow{p} = \int \hbar \overrightarrow{k}_\lambda f_\lambda d\lambda$ is the momentum density, and $\overline{\overline{\Pi}} = \int \hbar \overrightarrow{k}_\lambda \overrightarrow{v}_\lambda f_\lambda d\lambda$ is the flux of the crystal momentum. By using Eq 3.3, we can describe how momentum changes when a phonon drifts and scatters.

For the solution of this problem, an expansion of the phonon distribution function in terms of macroscopic variables is suggested. Specifically, for finite Knudsen numbers, the non-equilibrium perturbations that depend on the heat flux $\overrightarrow{q}$ and its first derivatives in time and space are treated as independent variables

$$f_\lambda = f_\lambda^{eq} + \overrightarrow{\beta}_\lambda \cdot \overrightarrow{q} + \overrightarrow{\gamma}_\lambda \cdot \frac{\partial \overrightarrow{q}}{\partial t} + \overline{\overline{G}}_\lambda : \overrightarrow{\nabla} \overrightarrow{q} \tag{3.4}$$

here ${f_\lambda}^{eq}$ is the Bose-Einstein distribution at local equilibrium, $\overrightarrow{\beta}_\lambda$, $\overrightarrow{\gamma}_\lambda$, and $\overline{\overline{G}}_\lambda$ are unknown weight functions depending on the phonon mode to be determined; the :

symbol indicates a double contraction of tensor indexes. Two consistency equations ensure that Eq. 3.4 preserves the definitions of physical quantities: the first maintains the heat flux, and the second ensures no energy is added because of $\frac{\partial \overrightarrow{q}}{\partial t}$ as

$$\int \hbar\,\omega_\lambda\,\overrightarrow{v}_\lambda\,\overrightarrow{\beta}_\lambda\,d\lambda \;=\; \mathrm{I}, \tag{3.5}$$

$$\int \hbar\,\omega_\lambda\,\overrightarrow{v}_\lambda\,\overrightarrow{\gamma}_\lambda\,d\lambda \;=\; 0. \tag{3.6}$$

By using Eq 3.4, we substitute into the expressions for energy density e, heat flux $\overrightarrow{q}$, momentum $\overrightarrow{p}$, and momentum flux $\overline{\overline{\Pi}}$. As a result of this substitution, the momentum and momentum flux can be expressed in terms of q and T, the temperature appearing in ${f_\lambda}^{eq}$, which can then be substituted into Eq 3.3 to yield a heat flux equation as [61]

$$\vec{q} = -\tau\frac{\partial \vec{q}}{\partial t} - \kappa\nabla T + \ell^2\Big[\nabla^2\vec{q} + \alpha'\nabla(\nabla\cdot\vec{q})\Big] \tag{3.7}$$

where κ is the bulk thermal conductivity, τ is the heat flux relaxation time, l is the nonlocal length, and α' is a nonlocal coefficient. These intrinsic size-independent coefficients are determined by the weights. In KCM simulations, the previously derived transport equation (Eq. 3.7) must be solved together with the energy equation as

$$c\frac{dT}{dt} + \nabla\cdot\vec{q} = \dot{Q} \tag{3.8}$$

at the same time. In Eq 3.8, c and $\dot{Q}$ represent specific and volumetric heat generation, respectively.

In the following section, we first present the detailed model geometry, including the dimensions and boundary conditions, along with the material properties used for numerical verification of the KCM method. This verification is carried out by comparing the KCM results with the classical Fourier solution in domains where thermal size effects are negligible, providing a baseline for assessing model accuracy. Next, we outline the methodology for validating the KCM in scenarios where boundary-induced size effects become significant. This involves a comparison with thin-film thermal conductivity predictions obtained through a well-established theoretical approach reported in the literature, allowing us to evaluate the capability of the KCM to capture non-classical heat transport phenomena.

3.2. Model Geometry and Material Properties

3.2.1. Verification Study

By first simulating large domains without size effects, the accuracy of the KCM model can be verified by comparing the resulting temperature profiles with Fourier solution. To verify KCM model in simulation of domains with localized heat generation, we build a simple 2-dimensional model. The corresponding problem geometry and the lines used to plot the temperature distributions along the y and x axes are shown in Figure 3.1.

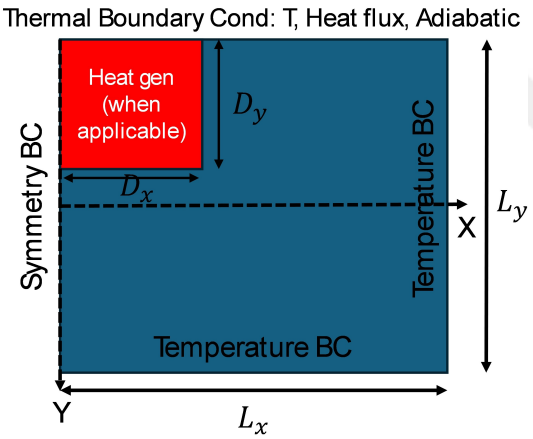

Figure 3.1. Geometry of the verification problem along with the boundary conditions and cutlines.

To minimize computational costs for KCM numerical simulations, only the right half of the domain shown in Figure 3.1 is modeled, with an axisymmetric boundary condition applied to the left boundary. Numerical verification of the KCM is performed in three different scenarios: (1) set the top boundary to 310 K, (2) apply a prescribed heat flux to top boundary, and (3) introduce volumetric heat generation with an adiabatic condition at the top boundary. The geometric characteristics for the large domains used for verification are presented in Table 3.1. These scenarios are designed to test the KCM under a variety of thermal boundary conditions, ensuring its accuracy across different boundary and heating configurations.

Table 3.1. Geometry characteristics for the large domain.

	Large domain
Total heat generation power $[W]$	1000
$L_x[\mu m]$ (domain length)	500
$L_y[\mu m]$ (domain height)	1000
$D_x[\mu m]$ (length of heat generation)	200
$D_y[\mu m]$ (height of heat genereraion)	200

The energy and transport equations (Eqs 3.8 and 3.7) required for KCM simulations are integrated into COMSOL Multiphysics software, where boundary conditions (BCs) and mesh generation are handled using the software's tools. A normal and tangential component of the heat flux (q_t and q_n) are defined at the boundaries as [62]

$$q_t = -Cl\,\nabla q_t \cdot n, \tag{3.9}$$

$$q_n = 0. \tag{3.10}$$

When the boundary condition is symmetric, the normal component of the heat flux (q_n) is set to zero, while when the boundary condition is prescribed, it is set to the total power of heat generation. A slip boundary condition is used for the tangential component, where C is defined as [62]

$$\mathrm{C} = \frac{1+p}{1-p} \tag{3.11}$$

in which p represents the proportion of phonons that undergo specular reflection at the boundaries. In these simulations, p is set to zero to represent fully diffusive reflection at the boundaries.

Finite element simulations in COMSOL rely on two parameters obtained from ab-initio simulations: the non-local length and bulk thermal conductivity. The thermophysical properties of the material are derived from the results of ab-initio simulations. For the verification of KCM, we initially used the non-local length and thermal conductivity of silicon as specified in the literature as listed in Table 3.2 [59]. Figure A.1

illustrates how to implement the energy and heat transport equations in the COMSOL software.

Table 3.2. Thermophysical properties used in FEM simulations.

	Si [59]
Nonlocal length $[nm]$	185
Thermal conductivity $[W/m.K]$	150

The non-local length can be considered as the average MFP of the material. KCM limits angular discretization to the x and y directions, requiring fine spatial discretization, resulting in a high number of mesh elements. A mesh independence study was conducted on the domain shown in Figure 3.1, and 618,223 quadrilateral elements were found to be sufficient. A detailed description of the KCM verification model can be found in Table A.1, including its geometry, boundary conditions, material properties, and mesh specifications.

3.2.2. Validation Study

Next, a two-dimensional model is created to assess the accuracy of the KCM in scenarios that include boundary-induced size effects, as illustrated in Figure 3.2. To isolate the size effects along the x-direction, the length in the y-direction (L_y) is set sufficiently large, effectively eliminating any thermal size effects along that axis and enabling the model to represent an infinite domain in both the y-direction and the plane corresponding to the xy axes. A uniform heat flux is established along the x-direction by imposing adiabatic boundary conditions on the top and bottom surfaces while maintaining different temperatures at the left and right boundaries. This configuration allows for a controlled evaluation of the KCM's ability to capture the influence of boundaries on thermal transport, particularly in confined geometries, and provides a direct comparison with theoretical thin-film thermal conductivity predictions.

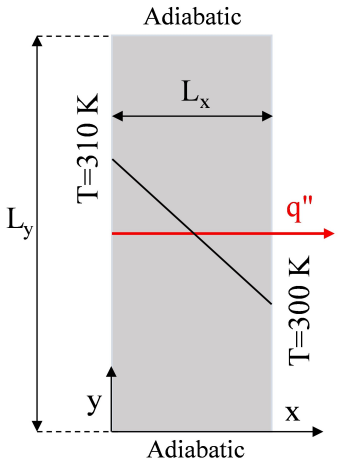

Figure 3.2. Schematic of the 2D model along with the boundary conditions used for investigating boundary-induced size effects.

A correct evaluation of the reduced thermal conductivity requires that heat transport be strictly limited to the x-direction. In order to achieve this, it is necessary to make sure that the heat flux stays uniform for any y-value. A parametric analysis on a silicon film with 1 μm thickness and different heights showed that to limit heat transfer in the y direction, the domain height must be at least ten times the film thickness. Using Fourier's law, the reduced thermal conductivity of any film thickness is found as

$$k_{tf} = -\overrightarrow{q''}\frac{L_x}{\Delta T} \tag{3.12}$$

where ΔT and L_x are the initial temperature difference in the x-direction and the thin film thickness, respectively. The reduced heat flux, $\overrightarrow{q''}$, is determined as

$$\overrightarrow{q''} = q''_x\,\overrightarrow{i} + q''_y\,\overrightarrow{j}. \tag{3.13}$$

3.3. Results

3.3.1. Verification Study

When applying the temperature boundary condition, the top boundary is set to 310 K, while the other boundaries remain 300 K. Considering boundary size effects are minimal in larger domains, the temperature distribution should closely match the one derived from the Fourier solution. As illustrated in Figure 3.3, the temperature

distributions along both the y and x directions are in good agreement.

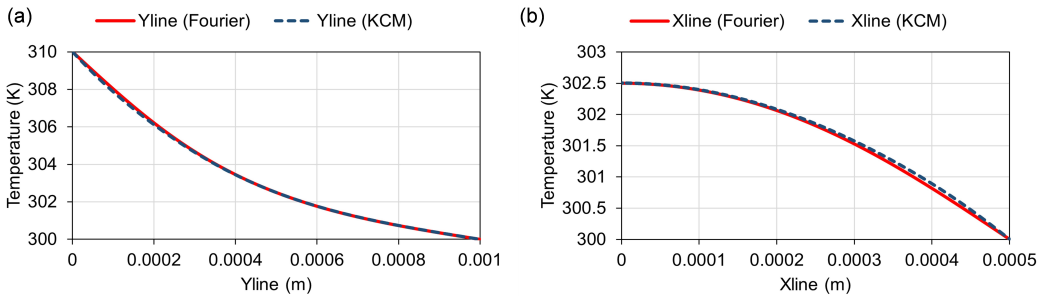

Figure 3.3. Temperature distribution along the (a) Y-line and b) X-line obtained from KCM when Top boundary is set to 310 K.

Next, a heat flux boundary condition is applied. As shown in Figure 3.4, the maximum temperature for both solutions is around 302 K, and the temperature distributions are similar. Hence, when analyzing heat transfer in larger domains, the KCM solution converges towards the Fourier solution.

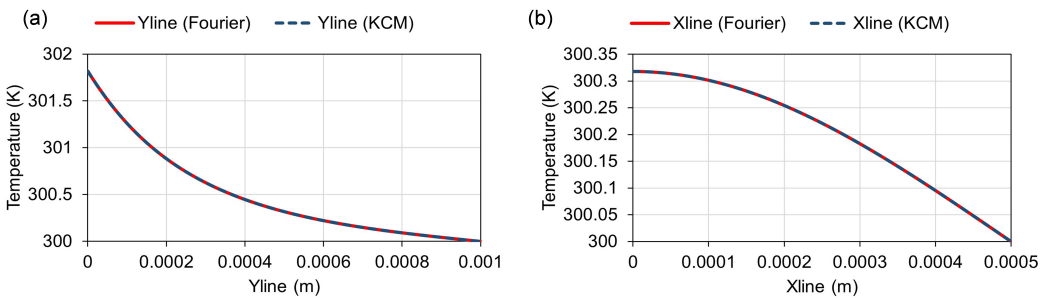

Figure 3.4. Temperature distribution along the (a) Y-line and b) X-line obtained from KCM when heat flux boundary condition is applied.

Finally, using the geometric characteristics listed in Table 3.2, a volumetric heat generation is applied to the domain. Both the KCM and Fourier solutions are computed under identical conditions, and the resulting maximum temperature and overall temperature distribution are found to match closely. This close agreement demonstrates the ability of the KCM to accurately reproduce classical thermal behavior in scenarios where size effects are negligible, thereby verifying the numerical implementation of the method.

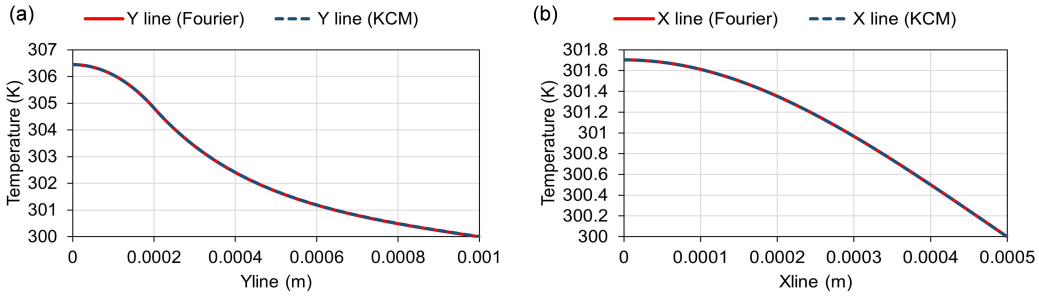

Figure 3.5. Temperature distribution along the (a) Y-line and b) X-line obtained from KCM when heat generation boundary condition is applied.

3.3.2. Validation Study

To implement Fourier's law to estimate thin-film thermal conductivities, the temperature distribution must first be obtained using a 2D Fourier solver. Afterwards, the phonon properties listed in Table 3.2 are utilized to determine the temperature distribution within the generated model using the KCM method. The temperature contour generated by the KCM model is shown in Figure 3.6a. Fourier and KCM temperature profiles are plotted along the horizontal centerline ($y = \frac{L_y}{2}$) and presented in Figure 3.6b. This figure shows that the KCM temperature gradient is shallower than predicted by the Fourier model. KCM behaves like a boundary-jump profile, while the Fourier profile remains unchanged by changing film thickness. It occurs because of boundary-induced size effects that prevent some phonons from efficiently transferring their energy along the x-axis. In Figure 3.6b, the slope of the temperature profile represents the horizontal heat flux. Using KCM model, heat flux along the x direction is reduced across the domain, as depicted in the figure.

The reduced thermal conductivity is finally compared with literature values. The KCM simulations for the current model, which has a domain thickness of $L_x = 1\ \mu m$ and $L_y = 10\ \mu m$, used 171,065 mesh elements. Due to the KCM method's high sensitivity to mesh resolution, we were only able to simulate domain thicknesses between $L_x = 0.1$ and $10\ \mu m$. The thermal conductivity of the thin film was estimated using the heat flux values of simulations and domain thicknesses in Eq 3.12.

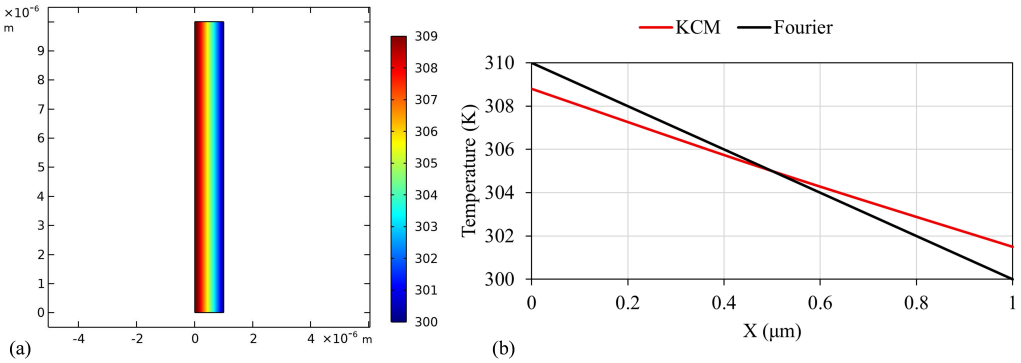

Figure 3.6. a) Temperature contour of KCM solution for 1 μm Si b) temperature profile along x direction obtained from KCM and Fourier solutions.

To make a comparison with previous studies, we computed the non-dimensional thin-film bulk thermal conductivity. Figure 3.7 presents the non-dimensional thermal conductivity predicted by the current KCM model, along with results from DFT simulations available in the literature, plotted against domain thickness. Both predictions show a constant trend of increasing thermal conductivity with film thickness due to reduced boundary scattering at higher thicknesses, approaching the bulk value at greater thicknesses (above$\sim$ 10000 nm.).

Size-dependent heat transport is accurately captured by the KCM technique, as evidenced by the overall agreement between the two curves. However, the KCM predictions are slightly less than the values reported in the literature for thicknesses between 100 and 1000 nm. For example, the KCM estimation of non-dimensional thermal conductivity is around 23% less than the one provided by the literature for film thicknesses of 100 nm. These discrepancies can be attributed to several factors, including the use of the gray approximation in phonon modeling, which neglects spectral variations in phonon properties, and the inherent limitations of the spatial and angular discretization used in the KCM simulations. Despite these minor differences, the results demonstrate that the KCM is capable of capturing the essential physics of boundary-limited thermal transport and provides a reasonable approximation of size-dependent conductivity trends.

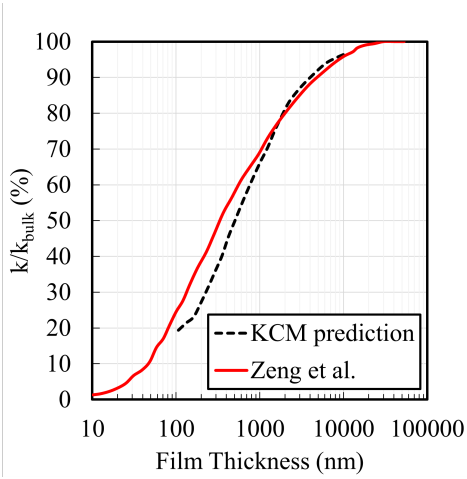

Figure 3.7. Non-dimensional thin film thermal conductivity of Si calculated from the current model validated by the DFT simulations of Zeng et al. [63].

3.4. Conclusion

In this chapter, KCM model is developed to investigate thermal problems with localized heat generation. First, the model is verified by simulating large domains with negligible size effects, and comparing the temperature profiles to Fourier's predictions. Next, the accuracy of the method for problems with thermal size effects is assessed through comparison with data from the literature. Main conclusions are summarized as follows:

- KCM is relatively easy to integrate into existing finite element solvers due to its compatibility with standard mesh generation tools.
- Angular and spatial discretizations are coupled in the KCM model, making it highly sensitive to nonlocal lengths and thin-film thicknesses, requiring an extremely fine mesh.
- A comparison of Fourier and KCM simulations shows that KCM performs well in investigations of heat transfer in materials with different boundary conditions in large domains.
- Using ab initio simulations, the KCM technique accurately predicted thermal size effects, showing overall agreement with the data from the literature. However, it slightly underestimated the thermal conductivity at thicknesses of 100-1000 nm,

for example, approximately 23% lower than the value reported in the literature for 100 nm thicknesses.

Here, we demonstrated the accuracy of the KCM model for a large domain; in the following chapter, we will evaluate its performance when localized heating effects are present. Meanwhile, another focus of the next chapter is using the popular technique FVDOM to investigate size effects induced by localized heating and compare its performance with KCM.

4. FINITE VOLUME DISCRETE ORDINATES METHOD

In this chapter, we introduce the gray FVDOM and compare its performance with KCM in solving problems with thermal-size effects caused by localized heating. Simulations with the same geometry and properties is repeated in smaller domains using temperature and heat generation boundary conditions for the performance test of KCM. In gray FVDOM simulations, this comparison provides valuable information for determining appropriate phonon properties. The FVDOM approach and its numerical simulation technique will be covered in the following section.

4.1. FVDOM Approach and Numerical Implementation

Similar to KCM, FVDOM starts with the phonon BTE given by

$$\frac{\partial e}{\partial t} + \overrightarrow{v_g} \cdot \nabla e = \left(\frac{\partial e}{\partial t}\right)_{\text{scatt}} + q'''. \tag{4.1}$$

In the gray model, all phonons share a uniform mean free path and a single group velocity v_g, regardless of their frequency or direction. The relaxation time approximation τ is used as a simplification in phonon transport theory. It defines the effective relaxation time as the average interval between successive scattering events, in order to characterize phonon scattering [64]. As a result of this approximation, phonon distribution functions gradually decay into local equilibrium energies e_0 through exponential decay. By applying the relaxation time approximation, Eq 4.1 can be rewritten as

$$\frac{\partial e}{\partial t} + \overrightarrow{v_g} \cdot \nabla e = \frac{e - e_0}{\tau} + q''' \tag{4.2}$$

in which the equilibrium energy density e_0 can be related to the lattice temperature T under the constant specific heat assumption C, allowing the lattice energy to be expressed linearly in temperature and providing a direct link between microscopic phonon energy and macroscopic thermal behavior such as

$$e_0 = CT. \tag{4.3}$$

It is possible to establish a relationship between phonon properties and a material's bulk thermal conductivity in the diffuse regime using kinetic theory as

$$k = \frac{1}{3} C v_g^2 \tau. \tag{4.4}$$

Both the group velocity and the relaxation time are essential for solving Eq 4.2. In general, the group velocity of the dominant phonon mode v_g is determined first and then applied to Eq 4.4. FVDOM in the numerical solution of Eq 4.2 is obtained by spatial and angular discretization separately, as illustrated in Figure 4.1. Control volume discretization is used for the spatial domain, and discrete ordinates are used for the angular domain represented in Figure 4.1. In Figure 4.1a, P represents the energy density at the central node, while the remaining terms denote the energy densities at neighboring nodes.

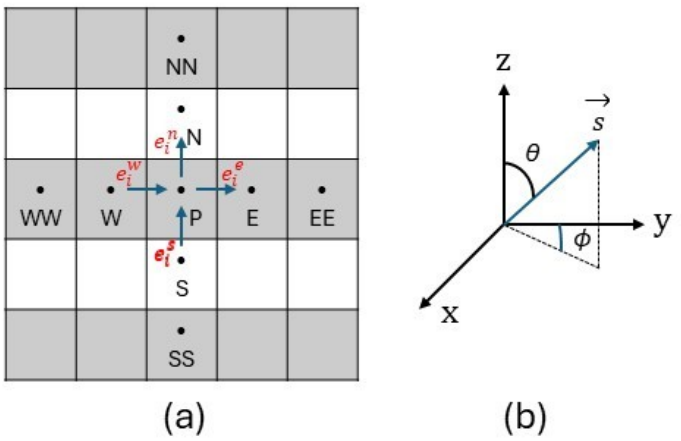

Figure 4.1. a) Spatial and (b) angular discretization of the phonon BTE by FVDOM.

In FVDOM, at each lattice point, the angular space is divided into solid angles, enabling phonon propagation. The steady-state equation for gray phonon transport, Eq 4.2, can be discretized in angular space as [65]

$$\overrightarrow{s_i} \cdot \nabla(v_{g_i}\, e_i) = \frac{e_i^0 - e_i}{\tau} + q_i'''. \tag{4.5}$$

In this context, $\overrightarrow{s_i}$ (Figure 4.1a) represents the unit vector in direction i, while v_{gi} denotes the phonon velocity in that direction. Discrete values of e are stored at the cell centroids and are represented as e_i in direction i. The specific phonon propagation

directions depend on the selected angular discretization scheme. Angular discretization can be achieved using S_N quadratures or control angle methods. In S_N quadratures, when the unit vector along direction i is given as $\overrightarrow{s_i} = (\mu_i, \gamma_i, \xi_i)$, all directions $\overrightarrow{s_i} = (\pm\mu_i, \pm\gamma_i, \pm\xi_i)$ are also included in the quadrature. The total number of directions in an S_N quadrature, M, is determined using the formula $M = N(N+2)$. Here, the weights are determined by several constraints, such as

$$\sum_{m=1}^{M} w_i = 4\pi. \tag{4.6}$$

Even with few quadratures, higher-order S_N weights must preserve the first and second moments, with the first-moment condition satisfied when

$$\sum_{m=1}^{M} |\mu_i \, w_i| = \pi. \tag{4.7}$$

Rotational invariance can be achieved by incorporating the conservation of the second moment. Further, the use of these quadratures has been demonstrated to mitigate the impact of ray effects resulting from an insufficient number of phonon propagation. Here, the second moment condition is defined as

$$\sum_{m=1}^{M} \left|\mu_i^2 \, w_i\right| = \pi. \tag{4.8}$$

Using S_N quadratures to solve the phonon BTE, the lattice energy, e, and temperature T can be determined from directional energies, e_i, as

$$4\pi e^0 = C(T - T_{\text{ref}}) = \sum_{m=1}^{M} e_i \, w_i. \tag{4.9}$$

In the control angle discretization method, each octant is subdivided into M = N$\theta\times$ Nϕ uniform solid angles. As shown in Figure 4.1b, θ and ϕ represent the polar and azimuthal angles, respectively. The directional unit vector, $\overrightarrow{s_i}$, for each solid angle is (Figure 4.1b) defined as

$$\overrightarrow{s_i} = \sin(\theta_i)\sin(\phi_i)\,\vec{i} + \sin(\theta_i)\cos(\phi_i)\,\vec{j} + \cos(\theta_i)\,\vec{k}. \tag{4.10}$$

Eq. 4.5 when integrated over the discrete angular control volume yields to

$$\overrightarrow{S_i} \cdot \nabla(v_{g_i}\, e_i) = \frac{e_i^0 - e_i}{\tau}\, \Delta\Omega_i + q_i'''\, \Delta\Omega_i \tag{4.11}$$

where $\overrightarrow{S_i}$ is the direction cosine and $\Delta\Omega_i$ is the solid angle associated with direction i. In this case, they can be defined by [66]

$$\overrightarrow{S_i} = \int_{\phi-\frac{\Delta\phi}{2}}^{\phi+\frac{\Delta\phi}{2}} \int_{\theta-\frac{\Delta\theta}{2}}^{\theta+\frac{\Delta\theta}{2}} \overrightarrow{s_i}\, \sin(\theta)\, d\theta\, d\phi, \tag{4.12}$$

$$\Delta\Omega_i = \int_{\phi-\frac{\Delta\phi}{2}}^{\phi+\frac{\Delta\phi}{2}} \int_{\theta-\frac{\Delta\theta}{2}}^{\theta+\frac{\Delta\theta}{2}} \sin(\theta)\, d\theta\, d\phi. \tag{4.13}$$

Directional energies can be used to determine lattice energy and temperature

$$4\pi e^0 = C(T - T_{\text{ref}}) = \sum_{m=1}^{M} e_i\, \Delta\Omega_i. \tag{4.14}$$

Spatial discretization follows angular discretization. According to Figure 4.1a, the spatial domain is divided into structured rectangular control volumes. In this case, Eq 4.11 is integrated over these control volumes, yielding

$$v_g e_i^e\, \Delta y\, S_{i,x} - v_g e_i^w\, \Delta y\, S_{i,x} + v_g e_i^s\, \Delta x\, S_{i,y} - v_g e_i^n\, \Delta x\, S_{i,y} = \frac{e^0 - e_i}{\tau}\, \Delta V\, \Delta\Omega_i + q'''. \tag{4.15}$$

$S_{i,x}$ and $S_{i,y}$ represent the x and y components of the direction cosine $\overrightarrow{S_i}$. Equation 4.15 requires directional energies at east, west, south, and north faces: e_i^e, e_i^w, e_i^s, and e_i^n, respectively. Figure 4.1a illustrates the spatial discretization of the domain along the $i(+x)$ and $i(+y)$ directions, along with the directional energies at the east, west, north, and south faces of node P. There are several ways to define these face values in the literature, including first-order upwind schemes, linear upwind schemes (LUS), Sharp and Monotonic Algorithm for Realistic Transport (SMART), and Quadratic Upwind Interpolation for Convective Kinematics (QUICK) [67].

4.2. Assumptions in Deriving FVDOM vs. KCM from phonon BTE

The KCM and DOM methods are both based on the BTE, but they approach this equation differently. The hydrodynamic approach, such as the one used in the

derivation of the KCM model, constructs an ansatz (Eq 3.4) that expands the phonon distribution function f_λ around macroscopic quantities like the heat flux q, its time derivative $\frac{\partial q}{\partial t}$, and its spatial gradients ∇q. In contrast, the DOM discretizes the angular (directional) domain and treats f_λ as a function of position, time, and discrete directions s_i. The BTE is then solved numerically at each spatial and angular node, without assuming any form for the solution. Angular dependence is handled differently as well: the hydrodynamic method integrates it out through moment equations, while DOM retains full directional resolution using angular quadrature.

In both methods, the collision operator $C(f_\lambda)$ is often simplified using the Relaxation Time Approximation (RTA). In the hydrodynamic case, this operator is projected into moment space, leading to closed-form expressions involving relaxation times and mode-weighted coefficients (e.g., $\overrightarrow{\beta}_\lambda, \overrightarrow{\gamma}_\lambda$). The DOM, on the other hand, treats the collision term directly in its differential form for each ordinate : $C(f_\lambda) = -\frac{f_\lambda - {f_\lambda}^{eq}}{\tau_\lambda}$. Regarding solution strategy, the hydrodynamic method substitutes the ansatz into the BTE, projects it onto energy and momentum spaces, and derives a closed-form macroscopic evolution equation for q, often in the form of the GK equation. DOM requires discretization of both space and angle, and then numerically solves the BTE at each point and direction, integrating afterward to compute quantities like heat flux. Each method has trade-offs: hydrodynamic models are computationally efficient, capture nonlocal and memory effects, and can handle complex geometries via finite element methods (FEM), but require approximations and may lose accuracy in ballistic regimes. DOM offers highly accurate, mode-resolved results without assumptions on the form of f_λ, but is computationally expensive and limited in geometric flexibility due to the need for dense angular discretization.

4.3. FVDOM for Thin Film Materials: Validation Study

Previous studies addressed verifying the FVDOM solution for phonon BTE in larger domains such as the method we used for KCM [67]. Then, the thermal characterization of size effects using the FVDOM method is numerically validated using the

methodologies of our previous studies [2, 67, 68]. The method employed here is similar to the one used to validate KCM in the prediction of thin-film thermal conductivity. To predict nanoscale thermal transport, an accurate estimation of the phonon MFP is essential. The value used here agrees with the reference data. However, any shift in this value may distort the match and undermine the validity of the model. We intend to resolve this problem in the following sections by incorporating phonon mean free path spectra obtained from first-principles calculations to improve the simulations' accuracy even more.

The thermal behavior of thin film materials can be predicted using the FVDOM solution of phonon BTE by solving Eq. 4.15 and simulating the problem geometry depicted in Figure 3.2. The thermal conductivity of the thin film for different film thicknesses is then determined using Eq. 3.12 after the heat flux has been calculated in the x direction. In order to solve the phonon BTE numerically, uniform quadrilateral elements are used. The ratio of phonon MFP to element size for each thickness is kept at 15 to ensure that the results are mesh-independent. In order to evaluate the ability of FVDOM to capture size effects induced by boundary scattering, the thermal conductivities predicted by KCM along with the literature values derived from theoretical methods such as DFT are added for comparison. The non-dimensional thermal conductivity for Si obtained from the FVDOM and KCM solutions of phonon BTE using the properties mentioned in Table 3.2 along with the literature values is displayed as a function of film thickness, in Figure 4.2.

The FVDOM prediction of the thermal conductivity shows good agreement with the values found in the literature, especially when it comes to capturing the size-dependent thermal conductivity with decreasing film thickness. FVDOM predictions for Si closely resemble the data from Zeng et al., particularly in the sub-micron range [63].

After validating the FVDOM method in cases involving boundary-induced size effects, the following section investigates the performance of the KCM approach under

boundary and localized heating-induced size effects by comparing its predicted thermal behavior with that obtained from the FVDOM method.

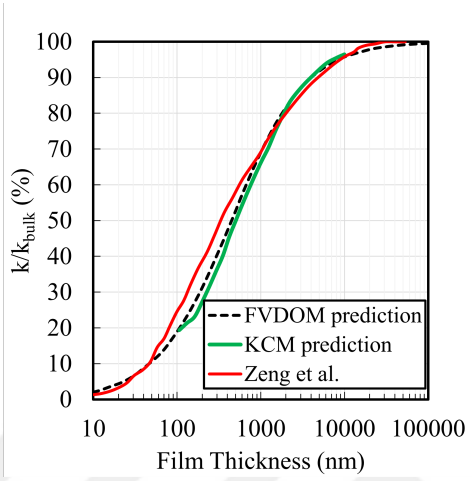

Figure 4.2. Non-dimensional thin film thermal conductivity of Si obtained from the FVDOM and KCM models validated by the DFT simulations of Zeng et al. [63].

4.4. Model Geometry and Thermophysical Properties

Next, we assess KCM performance by comparing its temperature results with FVDOM for smaller domains, using the same geometry as in Figure 4.3.

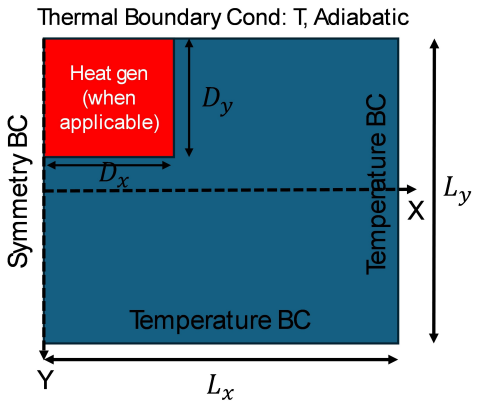

Figure 4.3. Geometry of the performance study along with the boundary conditions and cutlines.

Table 4.1 lists the geometry characteristics of the smaller domain for these simulations. The properties of silicon are used in these studies in the same way that they

are used in KCM verification simulations (Table 3.2). Equatıon 4.15 is numerically solved using the FVDOM solution of the phonon BTE with a MATLAB code that uses an iterative solver for the discretized phonon BTE (given in the Appendix A). For performance analysis, we consider the following case studies:

(i) Case study 1: $T_{top} = 310K$
(ii) Case study 2: Volumetric Heat Generation

Table 4.1. Geometry characteristics for the small domains.

	Small domain
Total heat generation power $[W]$	1000
$L_x[\mu m]$ (domain length)	0.5
$L_y[\mu m]$ (domain height)	1
$D_x[\mu m]$ (length of heat generation)	0.2
$D_y[\mu m]$ (height of heat genereraion)	0.2

The KCM performance model and the FVDOM simulation are described in full in Table A.2, which includes information on geometry, boundary conditions, material properties, and mesh details.

For mesh independence results, FVDOM requires significantly fewer spatial elements than KCM based on the mesh elements used. KCM, for example, has a quadrilateral mesh count of 826,826 while this value is only has 24,000 elements for FVDOM. FVDOM incorporates angular discretization, using S_6 quadrature with 24 directions, resulting in a total of $24{,}000 \times 24 = 576{,}000$ degrees of freedom. This combination of fewer spatial elements and directional resolution explains why the FVDOM method can achieve accurate solutions with a coarser spatial mesh compared to KCM, highlighting the trade-offs between spatial and angular resolution in different computational approaches for phonon transport modeling.

4.5. Results

4.5.1. Case Study 1: $T_{top} = 310K$

A temperature boundary condition is applied to the top boundary of a domain without heat generation, which is the first case study. As discussed previously, KCM is significantly influenced by spatial discretization. An accurate result is achieved by using a finer mesh with a larger number of cells, especially in regions with steep temperature gradients. Before comparing the temperature predictions from KCM with those from Fourier-based and FVDOM, it is instructive to first qualitatively assess the temperature fields obtained from the KCM and Fourier approaches and determine the effect of spatial resolution. The temperature contours in Figure 4.4 were obtained using the Fourier solution and the KCM method under identical boundary conditions.

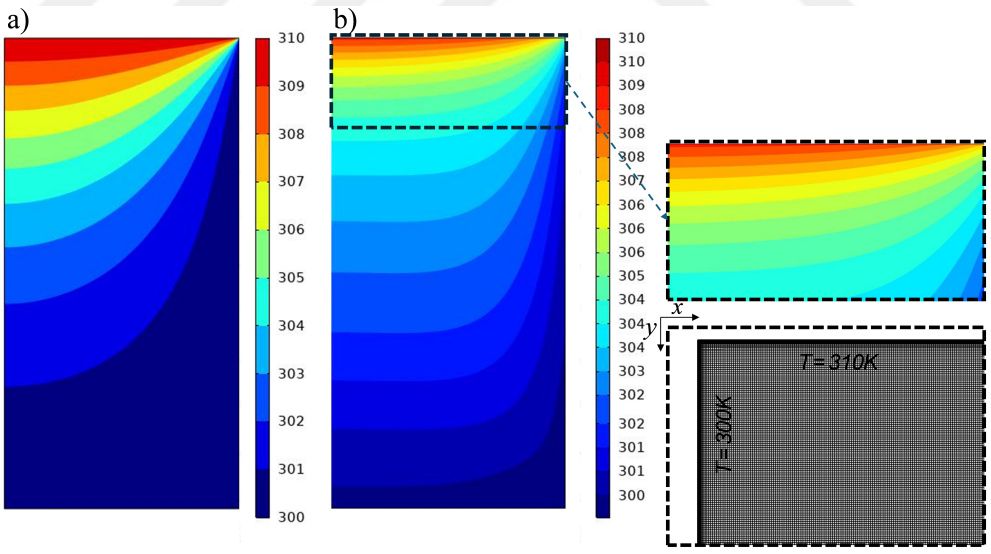

Figure 4.4. Temperature contours obtained for the temperature boundary condition using (a) Fourier and (b) KCM methods for the first case study.

It can be observed that the KCM solution requires a significantly finer mesh in order to capture the sharp temperature gradients, particularly in the upper region of the domain as shown in Figure 4.4. Due to the discrete nature of the KCM formulation and its reliance on accurate resolution of micro-scale transport phenomena, mesh size

is sensitive to micro-scale transport phenomena. By contrast, the Fourier solution is analytical and based on continuum assumptions, so it does not depend on mesh resolution and provides smooth temperature contours.

Next, temperatures of the small domain whose dimensions are shared in Table 4.1 are obtained by all three methods. The temperature distribution along the cutlines is shown in Figure 4.5.

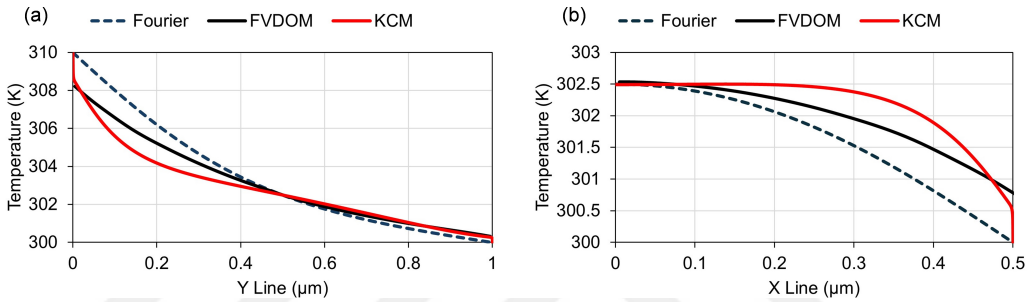

Figure 4.5. Temperature distribution along the (a) Y-line and b) X-line obtained from KCM, Fourier, and FVDOM methods for the first case study.

The FVDOM and KCM distributions along the cutlines accurately predict the temperature jumps at the top and bottom of the domain caused by boundary-induced thermal size effects. These effects are not captured by the Fourier solution, as expected. In addition, the temperature predictions of FVDOM and KCM differ slightly at the boundaries (top and bottom) where temperature boundary conditions are applied. Furthermore, there are slight discrepancies in the temperature profiles. The reason for this difference can be attributed to the fact that angular discretization is coupled with spatial discretization in KCM, a limitation that is not present in FVDOM.

4.5.2. Case Study 2: Volumetric Heat Generation

Subsequent simulations are carried out for a domain (with dimensions presented in Table 4.1) that includes a small heat generation region, using three different methods which is the second case study. Here, KCM method is further investigated under a heat generation boundary condition, similar to the previous section. As shown in Figure 4.6,

the temperature contours were obtained using the Fourier and the KCM methods, respectively, in the presence of volumetric heat generation.

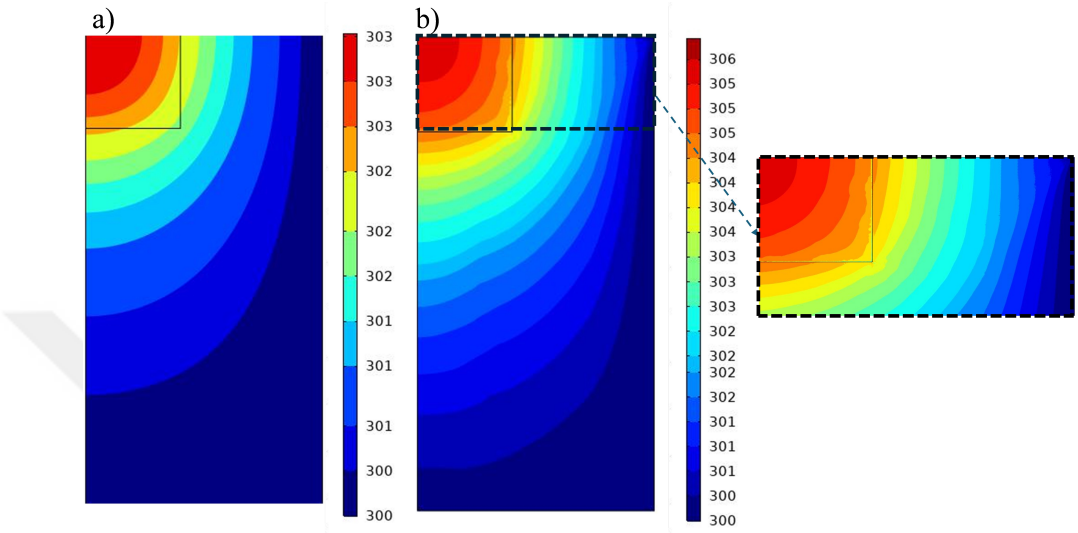

Figure 4.6. Temperature contours obtained for the heat generation boundary condition from (a) Fourier and b) KCM methods for the second case study.

Besides boundary-induced size effects, heat generation introduces additional size effects in this case. In the heat generation zone, where steep temperature gradients develop, these effects are particularly prominent. A very fine spatial discretization is required in the KCM method to accurately resolve these sharp gradients. Due to the influence of mesh resolution, the temperature contours near the heat generation region appear less smooth and more irregular compared to the Fourier solution. Despite these limitations, the KCM method can still capture the essential characteristics of the temperature field. While KCM is mesh-sensitive, it remains a valid and reliable approach when a fine mesh is used to account for heat generation-induced size effects.

The next step is to compare all three methods under heat generation boundary condition. Temperature distributions along the cutlines are shown in Figure 4.7. Due to localized heating-induced size effects, the Fourier solution tends to underestimate temperature values. KCM predicts a maximum temperature of approximately 305.5 K, which is higher than that predicted by FVDOM. For a total heat generation of 1000 W/m, the difference between the two methods is less than 1 K due to numerical errors

and difference in angular discretization approaches. Despite its small magnitude, this discrepancy can be considered negligible.

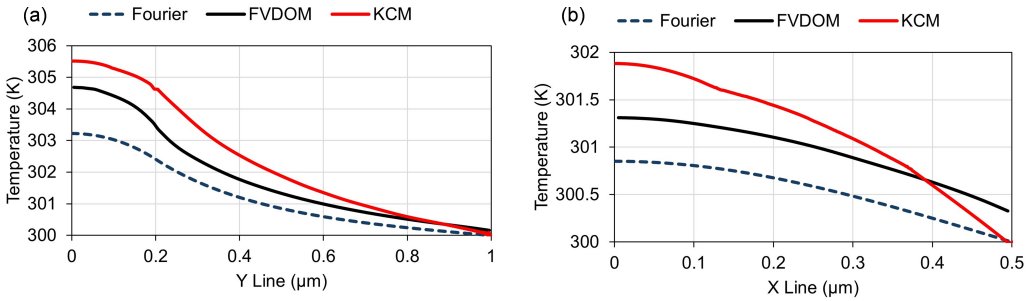

Figure 4.7. Temperature distribution along the (a) Y-line and b) X-line obtained from KCM, Fourier, and FVDOM methods for the second case study.

4.6. Conclusion

In this chapter, the performance of KCM method is investigated by comparing it with a validated FVDOM framework for scenarios that include both temperature and heat generation boundary conditions. While the KCM method offers valuable insights and integration flexibility, its high sensitivity to spatial discretization can lead to significant computational costs. The following points summarize the main conclusions:

- KCM strongly couples angular and spatial discretization, making it highly sensitive to mesh size. KCM needed over 1.5 million elements for small silicon domains, compared to only 24,000 elements used by FVDOM.
- Materials with long phonon mean free paths, require even finer meshes, which in turn leads to significantly increased computational time and resource usage in certain scenarios.
- Temperature jumps caused by boundary-induced and heat generation-induced size effects are accurately captured by FVDOM and KCM.
- In high-gradient regions and near boundaries, minor discrepancies exist, with KCM being slightly more mesh sensitive because of its angular-spatial coupling. While both methods yield comparable accuracy with differences below 1 K, FVDOM offers slightly better numerical robustness.

In the following chapter, we investigate the empirical relationship governing thermal spreading resistance. Due to the mesh resolution limitations inherent in the KCM simulation method, we used the FVDOM method to conduct a more accurate analysis. With this approach, we are able to investigate the effects of localized heating in greater detail and develop a semi-empirical model for predicting thermal spreading resistance.

5. THERMAL SPREADING RESISTANCE OF LOCALIZED HEATING

This chapter investigates the derivation of a semi-empirical relationship for thermal spreading resistance in scenarios involving localized heating. The FVDOM method is used to obtain numerical results since the KCM method is highly dependent on mesh size. As a result, an empirical correlation for thermal spreading resistance is developed based on FVDOM simulation results.

5.1. Model Geometry and Thermophysical Properties

Figure 5.1 shows a model of the 2D rectangular domain ($L_x \times L_y$) investigated in this study, with a localized heat generation region ($a \times b$). The left, right, and bottom boundaries are subjected to a temperature boundary condition of $T_0 = 300K$, while the top boundary is treated as adiabatic. A rectangular heat generation region is located near the top boundary.

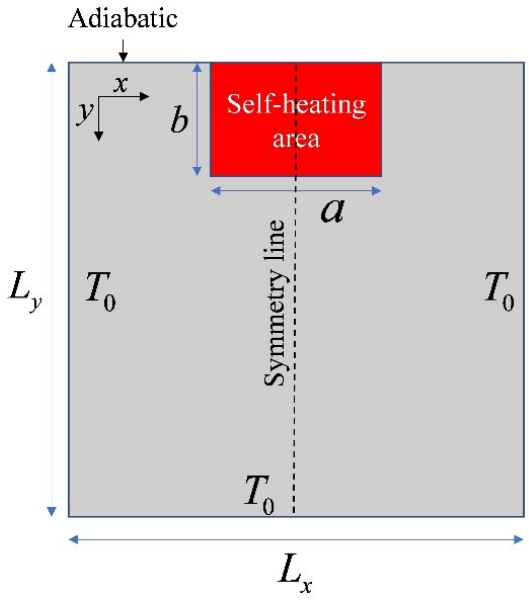

Figure 5.1. Volumetric self-heating and applied boundary conditions in the GaN domain.

Kinetic theory (Eq 4.4) is used to estimate the phonon properties from the bulk thermal conductivity, k_{bulk}. Using the thermal properties of wurtzite GaN, the study analyzes thermal size effects on GaN HEMTs. However, the results are later nondimensionalized so they can be presented independently of the material's thermophysical properties. While the phonon MFPs of wurtzite GaN range from 100 nm to 10 μm [69], an average phonon MFP reported in previous studies [49] is used in the gray model. The room-temperature thermal conductivity, specific heat, and phonon mean free path for used in this study are $k = 253\ W/m.K$, $C = 0.45\ J/g.K$, and $\Lambda = 1612\ nm$ [49], respectively. Table A.3 lists the numerical input parameters used in this simulation.

Equation 4.2 is discretized using FVDOM and then solved in MATLAB. In order to study the impact of angular discretization, three different quadrature sets (S4, S6, and S8) were used [70]. With 320,000 spatial grids, mesh independence is ensured. The initial energy density required for solving the discretized equation are derived from

$$\frac{\partial^2 T}{\partial x^2} + \frac{\partial^2 T}{\partial y^2} + \frac{q'''}{k_{\text{bulk}}} = 0 \tag{5.1}$$

which is the Fourier heat diffusion equation. The solution of Eq. 5.1 is also used for comparison purposes.

5.2. Results

To evaluate the accuracy of the simulations, the geometric parameters are selected to closely match the typical dimensions of a GaN HEMT device. These dimensions, reported in previous studies, serve as representative benchmarks, ensuring that the simulation results are directly relevant to practical device structures and can be meaningfully compared with established data: $L_x = 160\ \mu m$ and $L_y = 8\ \mu m$ [49], [69]. To ensure the results remain independent of the material's mean free path, these geometric parameters are expressed in terms of Knudsen numbers: $Kn_L = \Lambda/L_x = 0.01$, $Kn_t = \Lambda/L_y = 0.2$, $Kn_a = \Lambda/a = 1$, and $Kn_b = \Lambda/b = 10$. Heating powers of $P = 0.1\ W/m$ and $0.2\ W/m$ are applied to analyze the influence of heating power on thermal size effects.

Figure 5.2 shows the maximum temperature difference (ΔT_{max}) obtained with the FVDOM and Fourier methods. Although the proportionality constant (i.e., slope) depends on Kn_a, maximum temperature differences caused by localized heat generation show a linear relationship with heating power. Because of the linear nature of the problem, a dimensionless temperature can be defined as [69]

$$\theta = \frac{T - T_0}{P \times R_{1D,0}} \tag{5.2}$$

where, T_0 is the initial temperature of the domain and $R_{1D,0} = L_y/(L_x \times k_{bulk})$ denotes the 1D diffusive thermal resistance [48]. The dimensionless temperature remains unaffected by heating power and is utilized throughout the study to eliminate its influence on the results.

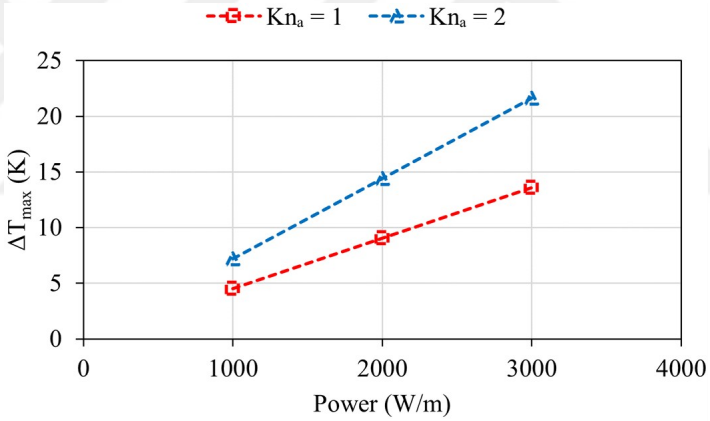

Figure 5.2. Maximum BTE and Fourier temperature difference, varying with heating power with ($Kn_L = 0.4$, $Kn_t = 0.8$, $Kn_b = 10$).

Figure 5.3 displays the dimensionless temperature profile along the vertical symmetry line shown in Figure 5.1, with results obtained from both the Fourier method and FVDOM. MC simulation results from a previous study [69] are also included for comparison.

The gray approximation is used in both methods for solving the phonon BTE. Compared to the MC method and FVDOM, the Fourier method consistently underestimates the temperature. The difference is due to the ballistic heat transport effects which occur when localized heating regions are smaller than the phonon mean free

path, which is not easily captured by Fourier's diffusion law.

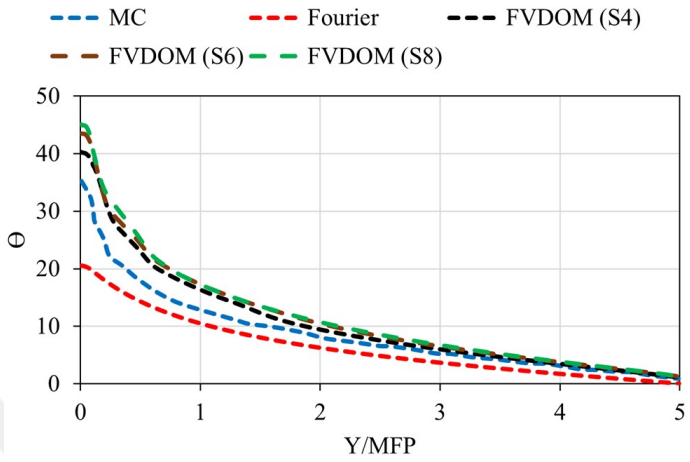

Figure 5.3. Dimensionless temperature distribution along the vertical symmetry line obtained from current FVDOM and MC [69] methods ($Kn_L = 0.01$, $Kn_t = 0.2$, $Kn_a = 1$, $Kn_b = 10$).

According to the MC method, temperatures are predicted 41.51% higher than those predicted by the Fourier method, whereas the FVDOM method predicts temperatures significantly higher. With the S6 quadrature instead of the S4 quadrature, the relative difference increases from 48.98% to 52.78%. Temperature predictions do not significantly differ when the number of directions is increased further with the S8 quadrature (40 directions). Both methods, MC and FVDOM, are influenced by the number of phonon directions in their discretization [71]. Due to the fact that the reference study does not provide details on the directional discretization, FVDOM results using the S6 quadrature are considered more accurate. Therefore, these results are used in the remaining analysis.

Thermal spreading resistance is observed when heat flows from a small cross-sectional area to a large cross-sectional area. A parameter like this is vital to the design and optimization of electronic systems, as it determines how well the device can dissipate heat. For example, the spreading resistance, which is determined by the geometry and thermal characteristics of the materials involved, affects the efficient heat transmission from a semiconductor chip [72]. By significantly reducing the spread-

ing resistance, a cap and thermal grease can enhance the electronic package's overall thermal performance.

In the past, thermal spreading resistance has been extensively studied using both analytical and numerical diffusion-based models based on the material's thermal properties and the system's geometry [73–75]. When thermal size effects are present the results of previous diffusion-based methods are no longer accurate.

Recent work investigates the thermal spreading resistance in GaN High Electron Mobility Transistors (HEMTs) with localized heating, where thermal size effects are important. Using hybrid Monte Carlo-diffusion simulations, a semi-empirical relationship for thermal spreading resistance was derived [48]. As discussed in this study, the thickness of the substrate and the dimensions of the heat source influence ballistic-diffusive heat conduction in GaN HEMTs. These findings provide valuable guidance for improving thermal performance and optimizing these devices. Moreover, phonon dispersion has been shown to affect the thermal spreading resistance of wide-bandgap (WBG) semiconductors when subjected to uniform heat flux, providing a useful tool for predicting junction temperatures and developing effective thermal management strategies for WBG devices [49]. These studies primarily consider localized heat flux boundary conditions when deriving the semi-empirical relation for thermal spreading resistance. However, volumetric self-heating regions are more prevalent in many thermal scenarios influenced by thermal size effects. Thus, these relationships need to be extended to account for localized volumetric heat generation to provide a more accurate representation of real-world conditions. Typically, the thermal spreading resistance is determined by the average temperature rise in the heat-generating region [69] like

$$R = \frac{\int_{\text{heating area}} (T - T_0)\, dV}{\dot{Q} \times L \times t}. \tag{5.3}$$

$L \times t$ represents the rectangle heat generation area with a power dissipation density of $\dot{Q}$. The total thermal spreading resistance is then defined to examine how the geometric parameters of the problem influence thermal size effects. Based on the

maximum temperature within the domain, it is determined as

$$R = \frac{T_{\max} - T_0}{P} = R_{1D,0} \times \theta_{\max}. \tag{5.4}$$

This resistance is computed using the FVDOM results ($R = R_{FVDOM}$) for the given problem. Following the approach from the previous study used heat flux boundary condition, the components of this resistance can be mathematically expressed as [48]

$$\frac{R_{\text{FVDOM}}}{R_{1D,0}} = \frac{R_F}{R_{1D,0}} \times \frac{R_{1D,t}}{R_{1D,0}} \times \left[\frac{R_{\text{FVDOM}}}{R_{1D,t}} \times \left(\frac{R_F}{R_{1D,0}} \right)^{-1} \right] \tag{5.5}$$

where, R_F denotes the diffusive thermal spreading resistance in the presence of a volumetric heat source. The diffusive thermal spreading resistance is derived using the analytical solution based on Fourier's law [73]

$$\begin{aligned} R_F = 2\sum_{m=1}^{\infty} A_m \frac{\cos\left(\frac{m\pi}{2}\right) \times \sin\left(\frac{m\pi a}{2L_x}\right)}{\frac{m\pi a}{L_x}} + 2\sum_{n=1}^{\infty} A_n \frac{\cos\left(\frac{n\pi b}{2L_y}\right) \times \sin\left(\frac{n\pi b}{2L_y}\right)}{\frac{n\pi b}{L_y}} \\ + 4\sum_{m=1}^{\infty}\sum_{n=1}^{\infty} A_{mn} \frac{\cos\left(\frac{m\pi}{2}\right) \times \sin\left(\frac{m\pi a}{2L_x}\right) \cos\left(\frac{n\pi b}{2L_y}\right) \times \sin\left(\frac{n\pi b}{2L_y}\right)}{\frac{m\pi a}{L_x} \times \frac{n\pi b}{L_y}} \end{aligned} \tag{5.6}$$

where the coefficients A_m, A_n and A_{mn} are obtained from the Fourier series expansions of boundary conditions in literature [73]. In Eq. 5.5, $R_{1D,t}$ represents the thermal resistance of the cross-plane ballistic effects calculated from [76]

$$R_{1D,t} = R_{1D,0}\Big(1 + \frac{2}{3}Kn_t\Big). \tag{5.7}$$

The last part of Eq. 5.5 includes the ballistic effects caused by the localized heat generation defined by

$$\left[\frac{R_{\text{FVDOM}}}{R_{1D,t}} \times \left(\frac{R_F}{R_{1D,0}} \right)^{-1} \right] = r_a \times r_b. \tag{5.8}$$

The resistance in Eq. 5.8, known as localized heating resistance, is the product of the ballistic thermal resistance linked to the length (r_a) and the thickness (r_b) of the heat generation region. The effects of localized self-heating decrease as the heat generation region becomes larger, causing Eq. 5.8 to approach unity. Since the heat generation region is small in this study, the resulting resistance contributes significantly to the localized heating resistance.

Four distinct Knudsen numbers are defined as follows: $Kn_L = \Lambda/L_x$, $Kn_t = \Lambda/L_y$, $Kn_a = \Lambda/a$, and $Kn_b = \Lambda/b$ [69], and these are varied to analyze the factors affecting the resistance in Figure 5.1. Initially, the domain thickness is reduced from $L_y = 40\Lambda$ to 2.5Λ ($Kn_t = 0.025$ to 0.4), while the other three geometry parameters (Kn_L, Kn_a, and Kn_b) are kept constant. The relationship between the maximum dimensionless temperatures (θ_{max}) and Kn_t is presented in Figure 5.4a. This figure reveals a linear correlation between Kn_t and θ_{max}, which is in agreement with Eq. 5.7 [76]. The slope of the plot exceeds $\frac{2}{3}$ due to the combined effects of boundary scattering and localized heating-induced thermal size effects in this case. Similar effects can also emerge from the lateral boundaries of the domain. To examine these effects on the localized heating resistance described in Eq. 5.8, Figure 5.4b is presented. It is observed that reducing the domain length (increasing Kn_L) and thickness L_y leads to an increase in this resistance. When the film thickness is further reduced, the resistance remains relatively constant, as the boundary scattering described in Eq. 5.7 becomes the dominant factor affecting the total resistance. The influence of size effects from the domain boundaries becomes negligible when the domain length exceeds 5Λ ($Kn_L < 0.2$).

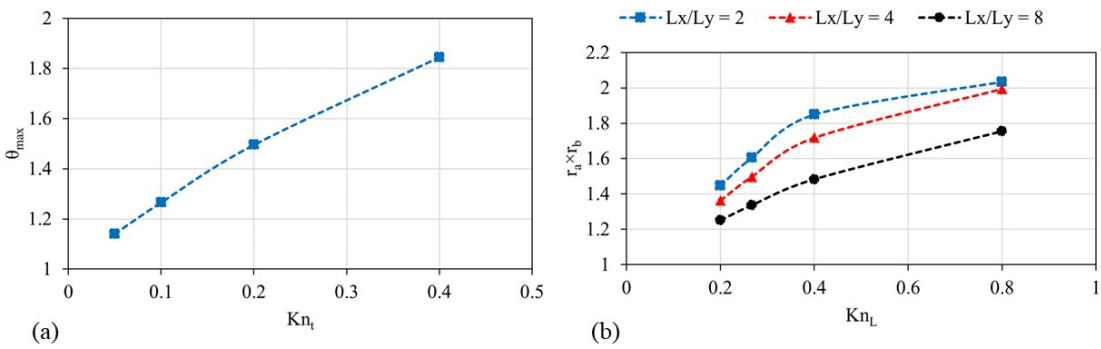

Figure 5.4. a) Maximum dimensionless temperature wrt. film thickness ($Kn_L = Kn_a = 0.5$) b) Localized heating resistance wrt. domain length ($Kn_a = 1$, $Kn_b = 10$) obtained from the current FVDOM simulations.

First, a large domain ($Kn_L = 0.01$) is modeled to examine the influence of the heat source length (Kn_a) and thickness (Kn_b) on localized heating resistance. Figure 5.5a shows the results when $Kn_b = 10$.

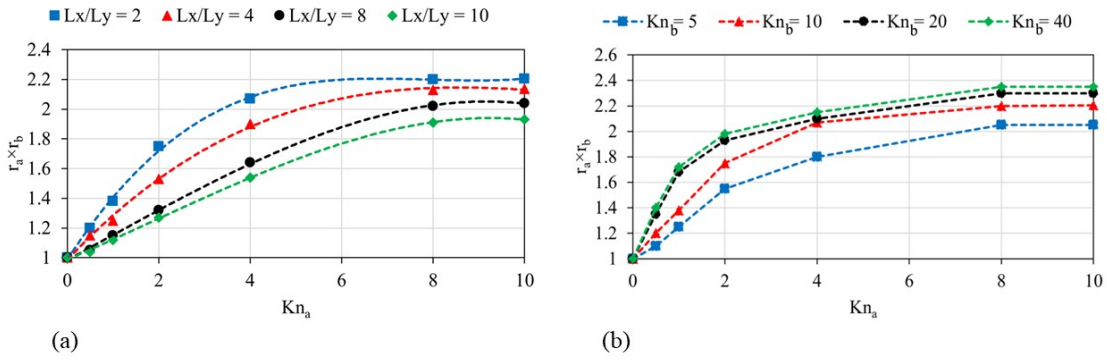

Figure 5.5. Residual thermal spreading resistance varying with heat generation a) length ($Kn_b = 10$, $Kn_L = 0.01$) and b) Residual thermal spreading resistance varying with heat generation length for different heat generation thicknesses.

The resistance decreases as Kn_a (the length of the heat source) decreases (i.e., the heat source becomes wider) and eventually approaches unity. However, if the heat source width is reduced ($Kn_a > 8$), the heat source behaves like a point source, causing the resistance to reach its maximum value of 2.2 and no longer change with Kn_a. The relationship here is not linear like the one in the previous problem with the heat flux [48]. Additionally, as shown in Figure 5.5a, the localized heating resistance is significantly influenced by the film thickness, which varies between $L_y = 80 - 16\mu m$. It is necessary to use a much thicker film in order to mitigate these effects. The next step is to examine the influence of the heat source thickness (Kn_b) on localized heating resistance. The domain is significantly thicker and wider to minimize boundary scattering effects. Figure 5.5b illustrates how the resistance varies with the heat generation length and thickness when a large domain is used. As Kn_b increases, the resistance increases. When ($Kn_b > 20$), the heat source behaves like a point source and no longer affects resistance. When Kn_a and Kn_b are large, the maximum resistance is observed.

Based on the simulation results obtained for large domains, the semi-empirical relation for the localized heating resistance is derived by performing a regression analysis, which quantifies the dependence of the resistance on the relevant parameters as

$$r_a \times r_b = \exp(0.128148) \times Kn_a^{0.19288} \times Kn_b^{0.102948}. \tag{5.9}$$

If the size scales of heat generation are known, the derived relation can be used to obtain the thermal spreading resistance, and can be applied to any material with a known phonon MFP. A similar result found in the literature is from the study [48], where a linear relationship $(1 + A_w Kn_w)$ was used to describe the resistance in a scenario with localized heat flux. A_w is the fitting parameter, and Kn_w is the heat flux boundary width. In addition, the previous study focused on the variation of resistance with domain size, whereas the current study deals with large domains. Consequently, comparisons can only be made for large domains with thin heat generation regions. In this case, the literature reports a resistance of $r_w = 1.6$, while in this study, it is $r_a \times r_b = 1.9$. It is likely that the higher resistance observed here is due to numerical errors, such as the smaller number of directions used in angular discretizing the gray BTE.

5.3. Conclusion

In this chapter, we investigated thermal spreading resistance in 2D domains with localized volumetric heat generation using the FVDOM solution to the gray phonon BTE. Further simulations could be conducted to establish a more comprehensive semi-empirical relation that incorporates boundary effects and depends on Kn_L, Kn_t, Kn_a, and Kn_b, along with estimated fitting parameters. The main conclusions are as follows:

- The domain's length and width, along with the heat generation regions, exhibit complex effects on the additional thermal spreading resistance.
- The findings are compared with resistances reported in related literature.
- The influence of geometrical parameters, such as the length and width of the domain and heat generation regions, on localized heating resistance is found to be non-linear, with significant effects occurring only within certain upper and lower limits.
- When $(K_{n_b} > 20)$ and $(K_{n_a} > 8)$, the heat source behaves like a point source and no longer affects the localized heating resistance, reaching the maximum resistance.

- A semi-empirical relationship between thermal spreading resistance, problem geometry, and material thermal properties is derived for large 2D domains with volumetric heat generation.
- This semi-empirical relationship provides a practical approach to calculating additional localized heating resistance, eliminating the need for computationally expensive sub-continuum modeling techniques.

6. APPLICATION TO REAL DEVICE

The objective of this chapter is to use and assess the numerical techniques developed in previous chapters using an actual device model. The KCM and FVDOM techniques are evaluated for their ability to accurately simulate the thermal behavior of AlGaN/GaN HFET (Heterostructure Field-Effect Transistor) devices. By doing this, we put the findings and observations about the benefits and drawbacks of each approach to the test in actual operational situations.

The KCM method is used for the first time to simulate a device with a real heat generation profile, allowing a direct comparison with the previously validated FVDOM framework. Using this comparison, we can gain a better understanding of how each method handles localized heating, temperature gradients, and device-level complexities. We also examine whether localized heating in HFETs can be accurately modeled using the concept of thermal spreading resistance. The accuracy and significance of this concept are investigated by comparing simulation results with predictions, especially when temperature-dependent phonon properties and size effects are present. Through this analysis, we aim to gain practical insights into both the modeling strategies and the thermal behavior of GaN-based devices.

6.1. Model Geometry and Thermophysical Properties

AlGaN/GaN HFETs, or HEMTs, are advanced semiconductor devices with immense potential for high-frequency and high-power applications. The device makes use of the unique interface between aluminum gallium nitride (AlGaN) and gallium nitride (GaN), where strong polarization products induce a high-density two-dimensional electron gas (2DEG) without intentional doping. Due to its high electron mobility and high current capacity, the 2DEG is capable of working efficiently under high voltage and frequency conditions, providing a significant advantage over conventional silicon or GaAs-based devices. Due to their high speed and robust power handling, AlGaN/GaN

HFETs are well suited to RF power amplifiers, radar systems, and power electronics. This chapter examines the size effects caused by localized heating in a real device by selecting a typical AlGaN/GaN HFET from the literature, as shown in Figure 6.1a.

As in Chapter 3, the device's side boundaries are subject to a temperature boundary condition. Using Eq. **??**, the normal and tangential components of the heat flux are determined. The device geometry and cutlines along the x- and y-directions, which will be used to plot the temperature distribution, are shown in Figure 6.1b.

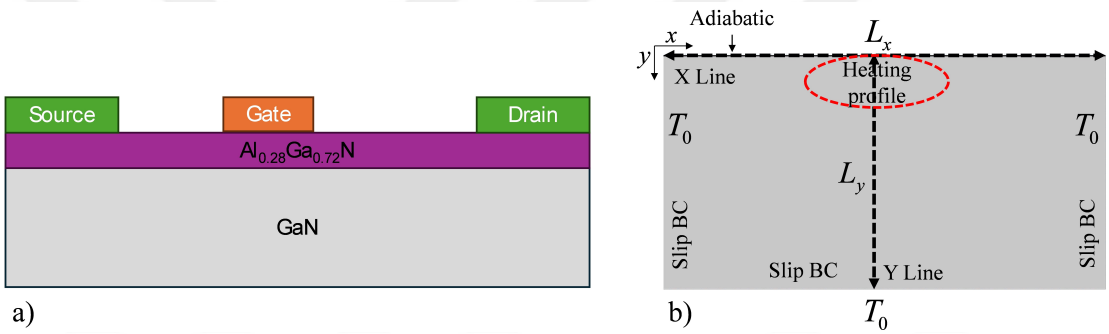

Figure 6.1. a) The schematic of the AlGaN/GaN HFET used for numerical simulations and b) simplified model.

A real heat generation profile is then used as the heat source in FVDOM and KCM simulations. The profile was derived from electrical simulation data reported in the literature [77]. Sentaurus Technology Computer-Aided Design (TCAD), which is frequently used for reliability evaluations and is known to generate channel temperatures equivalent to RF simulations for low-voltage devices, was utilized to perform electrical simulations under DC operating conditions [77]. Here, separate electron, hole, and lattice temperatures were modeled using a hydrodynamic transport model. The device initial temperature was set to 300 K, with 4 Ω Ohmic resistances at the source and drain and a Schottky gate with a 1.48 eV barrier height. The simulations were run at a power density of 4 W/mm under open channel biasing conditions ($V_G = 0$ V, $V_D = 6.5$ V). The contour of heat generation obtained from these simulations can be seen in Figure 6.2.

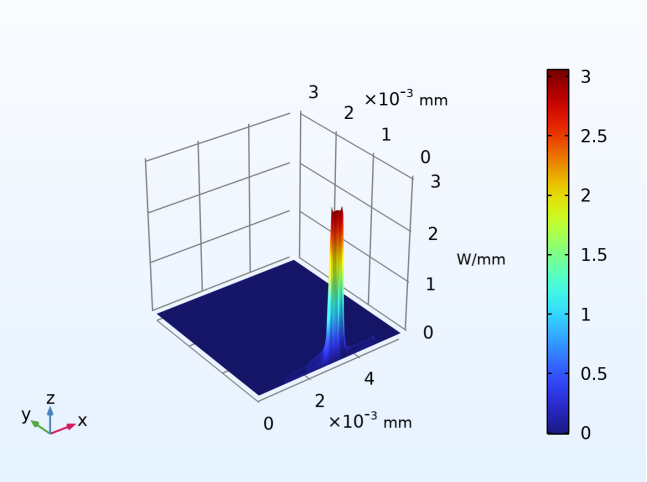

Figure 6.2. Realistic heat distribution applied in simulation models.

Before focusing on the details of KCM and FVDOM simulation with this heating profile, we need to estimate the phonon properties that are needed for GaN HEMT devices. In the previous chapter, we have used thermophysical properties of Silicon from the literature. In the following section ab initio simulations and their associated properties of GaN will be presented.

6.2. Ab-initio Simulations

To investigate the thermal transport properties of GaN, ab-initio calculations were performed using a combination of Density Functional Theory (DFT) via VASP, Phono3py for phonon transport, and the KCM solver for non-local effects. Figure 6.3 represents the steps followed to obtain thermal transport properties of wurtzite GaN via ab-initio simulations [78]. Detailed information on key phonon properties required for estimating phonon thermal transport behavior is provided in Appendix B.

The bulk thermal conductivity as a function of temperature is shown in Figure 6.4, which compares the findings of the current investigation utilizing two distinct supercell sizes with information from the literature, including both theoretical predictions and experimental data.

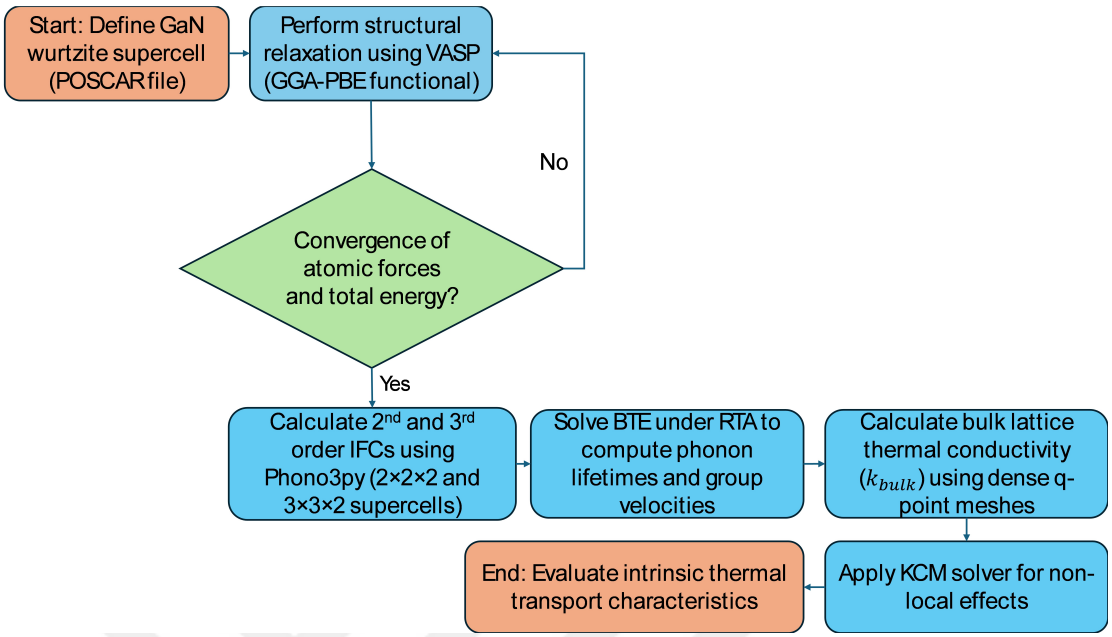

Figure 6.3. Flowchart for calculating phonon thermal transport properties of Wurtzite GaN using DFT simulations.

The computed thermal conductivity as a function of temperature using the 3×3×2 supercell is more in line with theoretical findings that have been published in the literature. Thus, in the upcoming simulations, this temperature-dependent thermal conductivity will be used for additional analysis.

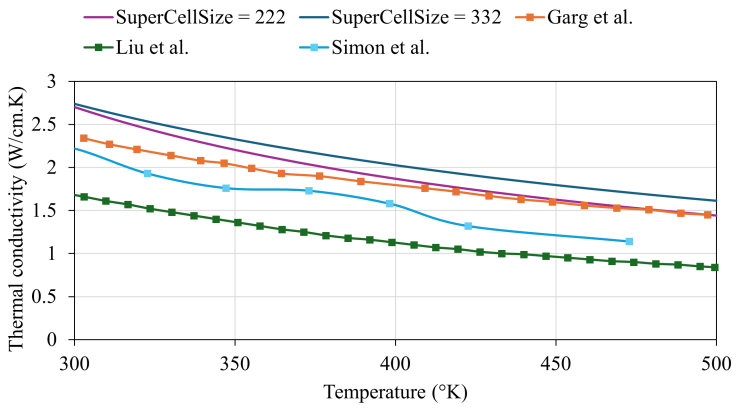

Figure 6.4. Wurtzite GaN bulk thermal conductivity obtained from the present study and literature (Garg et al. [79] , Liu et al. [80] , Simon et al. [81]).

The KCM technique was used to take spatially non-local effects in nanoscale heat transport into consideration. Both momentum-conserving (normal) and resis-

tive (Umklapp and impurity) phonon scattering processes are included in the model. The KCM solver was used to extract the non-local length scale l, a crucial parameter characterizing the spatial extent of collective phonon behavior, and simulate transport across finite lengths using temperature-dependent phonon lifetimes and velocities as inputs. As a function of temperature, the non-local length—an input parameter for Eq. 3.7—is computed and shown in Figure 6.5.

The non-local length starts at about 557 nm at 300 K and drops to 275 nm at 500 K. Given that the non-local length decreases with rising temperature, this trend is crucial for the thermal characterization of size effects. Consequently, at higher temperatures, size effects caused by boundary scattering lose their significance.

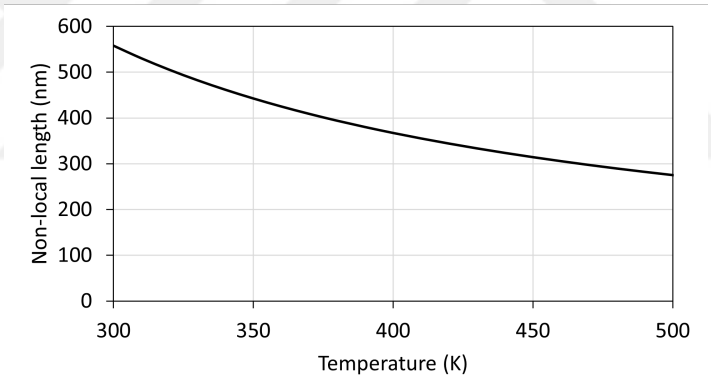

Figure 6.5. Wurtzite GaN nonlocal length as a function of temperature from ab-initio simulations.

Following DFT simulations of the wurtzite GaN, we examined the validity of KCM and FVDOM methods for predicting thin-film thermal conductivity. For this case, a similar validation approach to that used for silicon in Chapter 3 is used. The same geometry as shown in Figure 3.2 is used to investigate thickness-dependent thermal conductivity predictions using the FVDOM and KCM methods using the obtained phonon properties for wurtzite GaN. Like in Chapter 3, the L_y is ten times larger than L_x to remove the boundary scattering effects from the y direction. Table 6.1 lists the thermophysical properties of wurtzite GaN used in the thin film thermal conductivity predictions at 300 K.

Table 6.1. Thermophysical properties of GaN used for numerical simulations.

Property	**Value**
Nonlocal Length (l)	557 nm
Bulk thermal Conductivity (k)	273 W/mK

The predicted values of thermal conductivity for various thicknesses are compared with those obtained from FDTR experiments. Thickness dependent thermal conductivity of wurtzite GaN obtained from KCM and FVDOM solutions to the BTE phonon are shown in Figure 6.6, together with the experimental results.

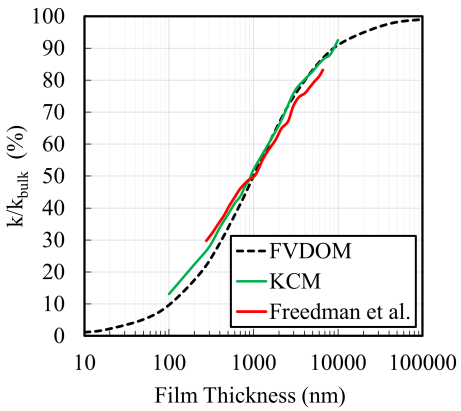

Figure 6.6. Non-dimensional thin film thermal conductivity of Wurtzite GaN obtained from the KCM and FVDOM simulations validated by the FDTR results of Freedman et al. [82].

Due to the sensitivity to mesh resolution of the KCM approach, we can only run our simulations in a thickness range of 0.1 to 10μm. The KCM and FVDOM results for GaN are in good agreement with the data from Freedman et al., however, minor variations at intermediate thicknesses might suggest sensitivity to input parameters like the phonon mean free path [82].

After identifying suitable thermophysical properties of wurtzite GaN through validation of thin film thermal conductivity predictions against FDTR experiments, these ab-initio-derived properties can now be applied in simulations of GaN HFET devices.

6.3. Results

6.3.1. KCM vs. FVDOM

In this part, we use an actual heating profile illustrated in Figure 6.2 to study thermal size effects due to localized heating in a realistic GaN HEMT device. The FVDOM and KCM approaches are both used in the analysis. Both models are given phonon properties derived from previous ab initio calculations. Here, we concentrate on simulations that use constant phonon properties because the FVDOM script can only handle constant properties and does not support temperature-dependent inputs. Both the bulk thermal conductivity and the nonlocal length (MFP) need to be given as input parameters, just like in the simulations in Chapter 3. The settings employed in these simulations are summarized in Table 6.1.

Using the device dimensions reported in the literature and shown in Figure 6.1, the heating profile (Figure 6.2) is interpolated to match this geometry and applied at the specified location within the GaN device. Table A.4 provides a summary of the numerical input parameters used to simulate the real GaN device.

The impact of the actual heating profile on thermal size effects caused by localized heating was then examined using the FVDOM and KCM approaches, both of which were applied using the specified geometric characteristics and boundary conditions. The element size and the ratio of the nonlocal length to the total domain length were kept the same as in Chapter 3 to guarantee constant accuracy. Figure 6.7 illustrates the resulting temperature contours in the localized heating zone, calculated from the FVDOM and KCM simulations, respectively. A comparison of these contours highlights the differences in heat spreading behavior captured by the two methods.

Both contours show a confined increase in temperature near the heat source, which is consistent with the profile of applied heat generation. The fact that the highest temperatures are found close to the domain's center-bottom region supports the idea

that heat is produced and concentrated there. Because of its angular discretization framework, FVDOM efficiently captures directional thermal transport in Figure 6.7a by producing more complex contour shapes with steeper gradients close to the hotspot. The results from KCM, on the other hand, are shown in Figure 6.7b, which exhibits a smoother, more symmetric heat spreading pattern, reflecting its emphasis on collective phonon behavior and diffusive transport.

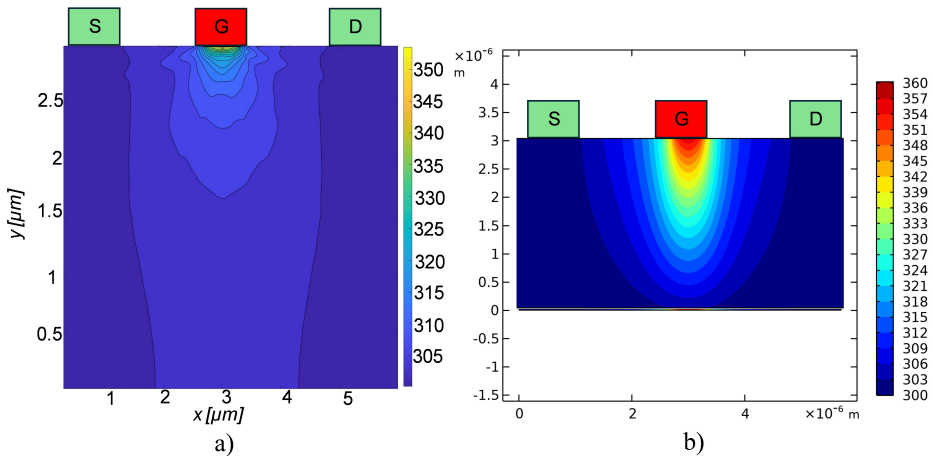

Figure 6.7. Temperature contours obtained with the realistic heating profile from (a) FVDOM and b) KCM methods.

In contrast to the KCM, which displays a more isotropic distribution in line with its collective transport assumptions, the FVDOM data demonstrate anisotropic heat spreading, most likely as a result of non-equilibrium phonon effects and interactions with boundaries. Both models display a drop in temperature near the device boundaries, verifying the application of fixed temperature boundary conditions and highlighting the role of boundaries in limiting lateral heat conduction. Figure 6.8 plots temperature profiles along the cutlines for both approaches to provide a more detailed look at the temperature distribution. These profiles emphasize the stronger localization of heat in the FVDOM simulations compared to the smoother gradients predicted by the KCM. Such distinctions underscore how model selection influences the interpretation of nanoscale heat transport behavior.

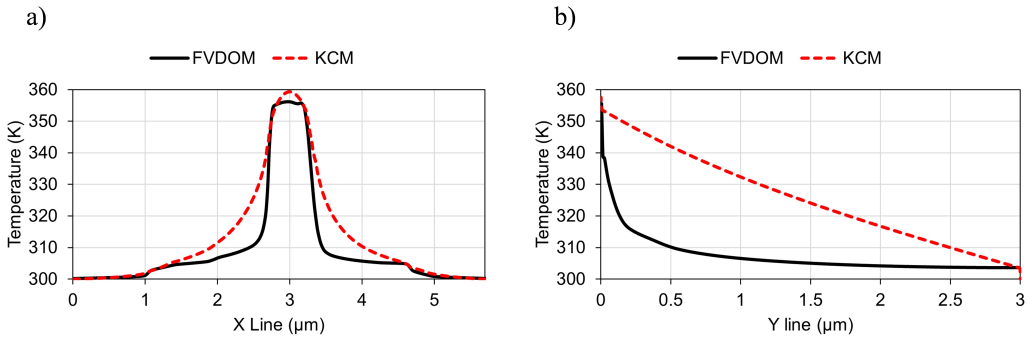

Figure 6.8. Temperature distribution along the (a) X-line and b) Y-line obtained from FVDOM and KCM methods.

These plots provide a more quantitative comparison between FVDOM and the KCM with respect to how each model captures heat localization and spread within the GaN device. In Figure 6.8a, both methods predict a peak in temperature around $x \approx 3\,\mu$m , which corresponds to the center of the heat generation zone. However, the KCM (red dashed line) shows a broader and smoother peak compared to the sharper and more localized profile observed in the FVDOM result (black line). This suggests that FVDOM captures directional and possibly ballistic aspects, resulting in more abrupt spatial temperature gradients, whereas KCM tends to mimic more diffusive and collective phonon transport behavior.

The temperature drop along the y-direction from the heat source upward is shown in Figure 6.8b. More substantial nonlocal effects or boundary influence in the vertical direction are suggested by the FVDOM result, which displays a sharper temperature gradient close to the heat source followed by a quick decrease. On the other hand, the KCM exhibits a smoother and more linear decay, which is in keeping with its collective phonon transport assumption.

The KCM technique produces a slightly higher peak temperature (about 360 K) than the FVDOM result (around 355 K), according to a comparison of the two results. This suggests that the KCM model predicts less effective heat spreading with the same boundary conditions and heat source. Overall, these comparisons reveal that while both methods capture the general shape and peak of the thermal distribution, FVDOM

provides more spatial resolution and highlights non-equilibrium effects, particularly near sharp temperature gradients.

Next, thermal spreading resistance—a key parameter in analyzing size-dependent thermal behavior—will be evaluated using the FVDOM method, along with the semi-empirical relation derived in Chapter 5, considering a realistic heat generation profile.

To achieve this, we first thoroughly simulated the FVDOM model using the heat generation profile shown in Figure 6.2. The maximum temperature was extracted from the simulation, a crucial step in determining the total thermal spreading resistance. Using Eqs. 5.5 to 5.7, each contributing term was calculated, leaving only the thermal spreading resistance due to localized heating as the unknown. Because the heating profile is non-rectangular, we made some necessary approximations in calculating the Knudsen numbers. Specifically, the heating profile was approximated as a heat flux boundary condition, given its small height. Additionally, the length of the heating region was taken as the maximum extent of the profile. With this thorough process and these assumptions, the thermal spreading resistance due to localized heating could be estimated by Eq. 5.8.

Next, we calculate this parameter using the semi-empirical relation (Eq. 5.9) derived from the FVDOM simulations. In this equation, the values of a and b must be defined to compute the Knudsen numbers. As we've discussed, the heating profile is approximated as a heat flux boundary condition, and the Knudsen numbers are determined accordingly. The product $r_a \times r_b$ is then calculated and importantly, compared with the thermal spreading resistance due to localized heating obtained from Eq. 5.5. The results obtained from both methods for calculating localized heating resistance ($r_a \times r_b$) are presented in Table 6.2.

As the Fourier solution cannot estimate localized heating induced size effects, the localized heating resistance will be equal to 1, which is lower than the semi-empirial relationship and FVDOM values. The results reveal that the FVDOM so-

lution yields a higher localized thermal resistance than the semi-empirical relation. The semi-empirical relation, used in this work to conveniently estimate localized thermal resistance based solely on the Knudsen numbers in the width and height directions of the heat source, has a significant drawback. This model, which assumes an idealized, semi-infinite domain with negligible phonon-boundary scattering, tends to severely underestimate the thermal resistance in confined or compact geometries. This underestimation highlights the urgent need for a more accurate model.

Table 6.2. Comparison of localized heating resistance obtained from FVDOM, Fourier simulations and semi-empirical relation.

Method	**Localized Heating Resistance**
FVDOM Simulation	1.42
Semi-Empirical Relation	1.34
Fourier	1

In contrast, when localized resistance is derived from a more comprehensive framework—one that decomposes total thermal resistance into components such as boundary-induced resistance, Fourier conduction, and localized heating resistance—it inherently incorporates the actual physics of the system. This includes effects like ballistic transport and phonon-boundary scattering. In compact domains where boundary effects are significant, such as the present case, this decomposition approach yields a more accurate and typically higher estimate of localized resistance. This is because the presence of nearby boundaries restricts the lateral spread of heat from the localized source, increasing thermal resistance. Therefore, for realistic modeling and design of micro- and nanoscale thermal systems, the resistance obtained from full-domain simulations and decomposition methods is generally more reliable and reflective of actual device behavior, providing a secure foundation for your work. However, in cases where the domain length and height are 10 times greater than the phonon mean free path, the semi-empirical relation provides a reasonable estimate of localized thermal resistance, eliminating the need for complex BTE simulations.

In the following section, the impact of temperature-dependent phonon properties on thermal size effects will be analyzed using the KCM approach.

6.3.2. KCM with Temperature Dependent Properties

Since the KCM model is implemented in COMSOL it allows to define the phonon properties as a function of temperature in order to examine the impact of temperature-dependent phonon properties on size effects induced by localized heating. The KCM method, in contrast to FVDOM, permits the inclusion of temperature-dependent properties, enabling a more realistic depiction of thermal transport behavior under various thermal settings. For this analysis, the temperature-dependent distributions of thermal conductivity and nonlocal length, illustrated in Figures 6.4 and 6.5 respectively, were utilized. For the FEM simulation, the same boundary conditions and a realistic heating profile were used as in the earlier examples. The resulting temperature contours are shown in Figure 6.9, which compares the cases with constant and temperature-dependent phonon properties.

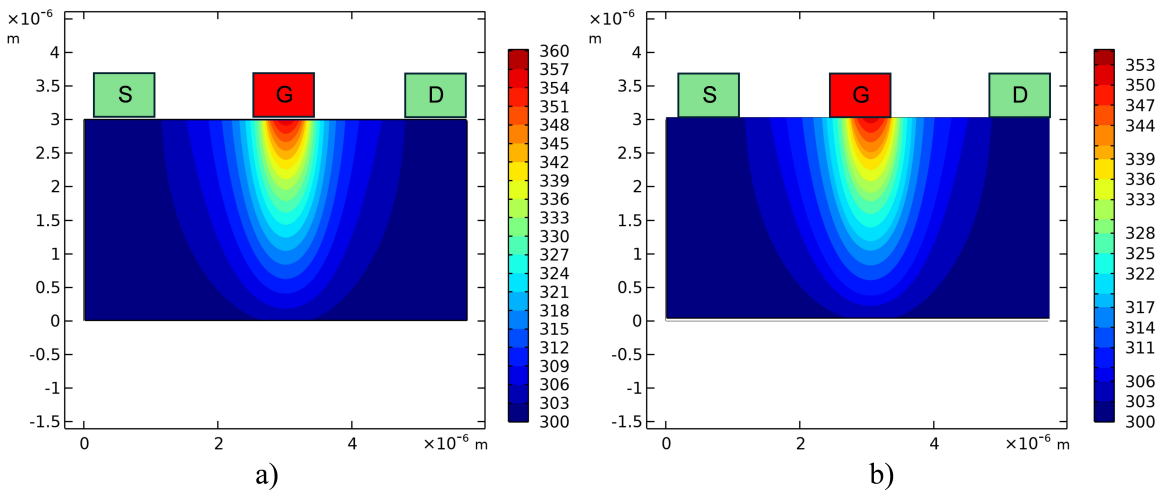

Figure 6.9. Temperature contours obtained from KCM method with the realistic heating profile for (a) constant and b) temperature-dependent properties.

The comparison reveals that the peak temperature in the case with constant phonon properties (Figure 6.9a) is noticeably higher (360 K) than in the case with

temperature-dependent properties (Figure 6.9b, 353 K). This shows that adding temperature-dependent behavior to the model improves heat spreading and keeps localized heating from being overestimated. Furthermore, ignoring the nonlocal length and temperature dependency of thermal conductivity can lead to an inaccurate depiction of thermal behavior, particularly in situations with substantial heat flux. Including these dependencies, as shown in Figure 6.9, allows the KCM to more accurately capture the thermal response of the material, making the simulation outcomes more physically reliable and relevant for device-level thermal analysis.

Temperature profiles along the X and Y directions are extracted and shown in Figure 6.10 in order to more thoroughly and quantitatively analyze the temperature distribution in both scenarios.

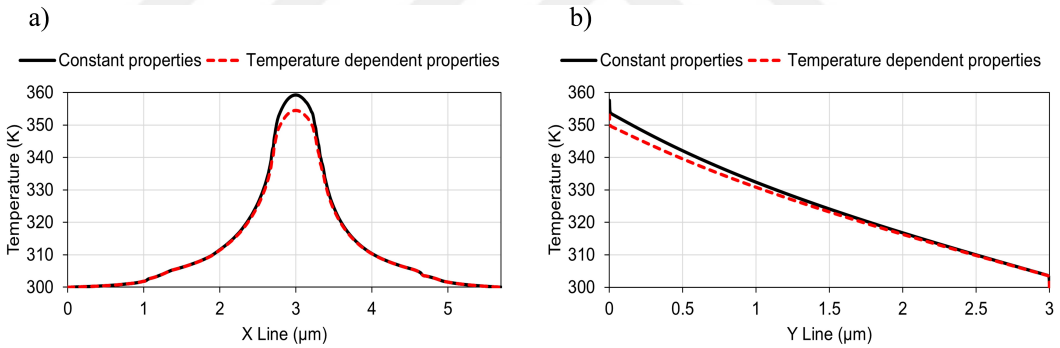

Figure 6.10. Temperature distribution along the (a) X-line and (b) Y-line obtained from KCM method for constant and temperature-dependent properties.

According to the temperature distributions, the peak temperature for the scenario with constant thermal properties is about 360 K, but when temperature-dependent properties are taken into account, it drops to about 354.5 K. Notably, the variation in temperature is most prominent near the hotspot region, with minimal differences observed farther from the heat source. Additionally, the temperature profiles along the Y-direction reveal a noticeable temperature jump in both cases, highlighting the presence of non-equilibrium thermal transport effects. In conclusion, incorporating temperature-dependent phonon properties in thermal simulations using the KCM approach significantly enhances accuracy by capturing reduced thermal conductivity

and localized heating effects, which are otherwise underestimated in constant-property models.

6.4. Conclusion

In this chapter, we present the results of our comprehensive FVDOM and KCM simulations on a typical AlGaN/GaN HEMT device. These simulations, conducted with a realistic heat generation profile, provide a thorough assessment of hotspot temperature and the increased thermal spreading resistance due to localized heating. We also delve into the effect of temperature-dependent phonon properties on thermal size effects. These are the key conclusions from this chapter, demonstrating the depth and rigor of our research:

- FVDOM offers higher spatial resolution and captures non-equilibrium and directional thermal transport effects more effectively, while KCM provides a smoother, more diffusive representation of heat spreading.
- The higher peak temperature predicted by KCM (approximately 9% higher) suggests reduced heat dissipation efficiency compared to FVDOM under identical conditions, emphasizing the importance of model selection in analyzing localized heating.
- Incorporating temperature-dependent phonon properties in the KCM model reduces the predicted peak temperature from approximately 360 K to 354.5 K, reflecting reduced size effects due to smaller MFP of heat carriers.
- The temperature difference is most significant near the hotspot region, while both constant and temperature-dependent cases show a temperature jump along the Y-direction, indicating the persistence of non-equilibrium transport and highlighting the importance of modeling temperature-dependent behavior in high heat flux scenarios.
- By comparing the thermal spreading resistance from the full-domain FVDOM simulation with that estimated using the semi-empirical relation, it is evident that the semi-empirical model slightly underpredicts localized resistance in confined

domains. Thus, this model is used for obtaining fast results where simulations are not available.

7. CONCLUSIONS AND FUTURE RESEARCH

This thesis presents a comprehensive investigation into thermal-size effects and localized heating in micro- and nano-scale systems. It uses the Kinetic Collective Model (KCM) and the gray Finite Volume Discrete Ordinates Method (FVDOM) to solve the phonon Boltzmann Transport Equation (BTE). The methodologies, detailed across three key chapters, were applied to analyze various aspects of heat transfer in semiconductors. Importantly, the research extends beyond fundamental simulation methods to explore practical device-level implications, making the findings directly relevant to the field. The following are the conclusions from each section of this thesis:

After validating KCM with Fourier solution for domains without size effects in chapter 3, chapter 4's comparative analysis of KCM and FVDOM focused on their capabilities in capturing thermal-size effects in systems with localized heating. KCM was shown to be a powerful tool for extracting thermophysical properties from ab initio simulations and is compatible with standard finite element methods. However, its strong coupling between angular and spatial discretization results in significant sensitivity to phonon mean free paths, requiring extremely refined meshes to achieve accurate temperature distributions—particularly for materials with long mean free paths, such as GaN. In contrast, FVDOM, with its computational efficiency even with relatively coarse meshes, offers a practical solution for certain applications, instilling confidence in its application.

Chapter 5 shifted focus to the phenomenon of thermal spreading resistance in two-dimensional domains. Utilizing FVDOM, a semi-empirical correlation was developed to relate spreading resistance to geometric and material parameters under localized heating. The analysis revealed that the effects of geometry on resistance are highly non-linear and become significant only within certain dimensional thresholds. Notably, once Knudsen numbers exceed specific limits $\mathrm{Kn_b} > 20 \quad \text{and} \quad \mathrm{Kn_a} > 8$, heat sources effectively act as point sources, capping the resistance. The resulting semi-empirical

relation provides a practical alternative to full-scale simulations for large domains, offering a balance between accuracy and computational cost.

In Chapter 6, the methods were applied to a real-world device: an AlGaN/GaN HEMT structure. Using realistic heat generation profiles, simulations explored hotspot behavior and spreading resistance, emphasizing the role of temperature-dependent phonon properties. FVDOM captured spatial thermal gradients and non-equilibrium transport more precisely, whereas KCM, while more diffusive, predicted higher peak temperatures, indicating lower heat dissipation efficiency. Incorporating temperature-dependent properties improved KCM's accuracy, reducing the peak temperature and better representing localized heating. Moreover, the comparison between FVDOM results and the semi-empirical relation highlighted the limitations of the latter in confined domains, where boundary scattering becomes significant.

Future investigations may focus on the following areas:

- Expanding simulations to fully three-dimensional domains and more realistic device geometries (beyond idealized 2D domains) will improve the practical relevance of the models, particularly in applications involving non-uniform or layered materials.
- Given the high computational cost of KCM due to its sensitivity to spatial discretization, future work could explore adaptive mesh refinement algorithms that optimize mesh density in critical regions (e.g., near hotspots) while keeping it coarse elsewhere, thereby reducing resource usage without sacrificing accuracy.
- Although substrate properties are not directly included in the semi-empirical model, when combined with independent substrate simulations, the correlation improves thermal modeling by taking heat spreading and substrate conduction into account. TCAD tools, SPICE thermal networks, or FEA platforms such as COMSOL can all implement it with specific substrate parameters.
- Data-driven methods could be used to predict thermal transport properties or to create surrogate models that replicate BTE-based simulations at a fraction of the

computational cost, enabling faster design iterations.

- While this thesis is computational, future work could include experimental validation (e.g., using thermoreflectance or Raman thermometry) to benchmark model accuracy and improve confidence in simulation results.

REFERENCES

1. Campbell, S. A., *The Science and Engineering of Microelectronic Fabrication*, Oxford University Press, Oxford, 2001.

2. Chatterjee, B., C. Dundar, T. E. Beechem, E. Heller, D. Kendig, H. Kim, N. Donmezer and S. Choi, "Nanoscale Electro-Thermal Interactions in AlGaN/GaN High Electron Mobility Transistors", *Journal of Applied Physics*, Vol. 127, No. 4, p. 044502, 2020.

3. O'Connor, P. D. T., "Arrhenius and Electronics Reliability", *Quality and Reliability Engineering International*, Vol. 5, No. 4, pp. 255–255, 1989.

4. Zhang, L. and T. Treurniet, "On the Challenges of Thermal Characterization of High-Power, High-Brightness LED Packages", *Electronics Cooling*, Vol. 14, No. 2, p. 10, 2008.

5. Tang, W., J. Sebot, M. Iyengar and K. Vaidyanathan, *Thermal Management of Microelectronic Devices: Challenges and Solutions*, Tech. rep., Intel Corporation, Santa Clara, USA, 2021.

6. Kendig, D., A. Tay and A. Shakouri, "Thermal Analysis of Advanced Microelectronic Devices Using Thermoreflectance Thermography", *22nd International Workshop on Thermal Investigations of ICs and Systems (THERMINIC)*, pp. 115–120, Budapest, Hungary, 2016.

7. Mathew, J. and S. Krishnan, "A Review on Transient Thermal Management of Electronic Devices", *Journal of Electronic Packaging*, Vol. 144, No. 1, p. 010801, 2022.

8. Perpiñà, X., M. Vellvehi and X. Jordà, *Thermal Issues in Microelectronics*, Royal Society of Chemistry, London, 2015.

9. Asheghi, M., Y. K. Leung, S. S. Wong and K. E. Goodson, "Phonon-Boundary Scattering in Thin Silicon Layers", *Applied Physics Letters*, Vol. 71, No. 13, pp. 1798–1800, 1997.

10. Hosseinzadeh Sani, M. and S. Khosroabadi, "Improving Thermal Effects and Reduction of Self-Heating Phenomenon in AlGaN/GaN/Si Based HEMT", *Journal of Electronic Materials*, Vol. 50, No. 4, pp. 2295–2304, 2021.

11. Solet, V. K. and S. K. Pandey, "Ab Initio Study of Phononic Thermal Conduction in ScAgC Half-Heusler", *The European Physical Journal B*, Vol. 96, No. 5, p. 53, 2023.

12. Kittel, C. and P. McEuen, *Introduction to Solid State Physics*, John Wiley and Sons, Hoboken, 2018.

13. Kushwaha, A. K., "Lattice Dynamical Properties of Group-Iii Nitrides an (A= B, Al, Ga and In) in Zinc-Blende Phase", *International Journal of Thermophysics*, Vol. 37, No. 3, p. 30, 2016.

14. Shin, S., Q. Wang, J. Luo and R. Chen, "Advanced Materials for High-Temperature Thermal Transport", *Advanced Functional Materials*, Vol. 30, No. 8, p. 1904815, 2020.

15. Guo, Y., M. Bescond, Z. Zhang, M. Luisier, M. Nomura and S. Volz, "Quantum Mechanical Modeling of Anharmonic Phonon-Phonon Scattering in Nanostructures", *Physical Review B*, Vol. 102, No. 19, p. 195412, 2020.

16. Jiang, P., L. Lindsay and Y. K. Koh, "Role of Low-Energy Phonons with Mean-Free-Paths > 0.8 μm in Heat Conduction in Silicon", *Journal of Applied Physics*, Vol. 119, No. 24, p. 245705, 2016.

17. Vermeersch, B., J. Carrete and N. Mingo, "Cross-Plane Heat Conduction in Thin Films with Ab Initio Phonon Dispersions and Scattering Rates", *Applied Physics*

Letters, Vol. 108, No. 19, p. 193104, 2016.

18. Hu, Y., T. Feng, X. Gu, Z. Fan, X. Wang, M. Lundstrom, S. S. Shrestha and H. Bao, "Unification of Nonequilibrium Molecular Dynamics and the Mode-Resolved Phonon Boltzmann Equation for Thermal Transport Simulations", *Physical Review B*, Vol. 101, No. 15, p. 155308, 2020.

19. Ahmed, B. A., F. Ahmed and A. S. Hakeem, "Joule Heating in Two-Dimensional Materials Based Transistors", *Research and Development in Material Science*, Vol. 10, No. 4, pp. 1173–1175, 2019.

20. Tang, X., R. Bonner, T. Desai and A. Fan, "A 2-D Numerical Study of Microscale Phase Change Material Thermal Storage for GaN Transistor Thermal Management", *27th Annual IEEE Semiconductor Thermal Measurement and Management Symposium*, pp. 27–34, San Jose, CA, USA, 2011.

21. Huang, D., Q. Sun, Z. Liu, S. Xu, R. Yang and Y. Yue, "Ballistic Thermal Transport at Sub-10 nm Laser-Induced Hot Spots in GaN Crystal", *Advanced Science*, Vol. 10, No. 2, p. 2204777, 2023.

22. Tang, Z.-L., Y. Shen, H.-L. Li and B.-Y. Cao, "Topology Optimization for Near-Junction Thermal Spreading of Electronics in Ballistic-Diffusive Regime", *IScience*, Vol. 26, No. 7, p. 107179, 2023.

23. Jeong, C., S. Datta and M. Lundstrom, "Thermal Conductivity of Bulk and Thin-Film Silicon: a Landauer Approach", *Journal of Applied Physics*, Vol. 111, No. 9, p. 093708, 2012.

24. Schmidt, A. J., X. Chen and G. Chen, "Pulse Accumulation, Radial Heat Conduction, and Anisotropic Thermal Conductivity in Pump-Probe Transient Thermoreflectance", *Review of Scientific Instruments*, Vol. 79, No. 11, p. 114902, 2008.

25. Braun, J. L., C. H. Baker, A. Giri, M. Elahi, K. Artyushkova, T. E. Beechem,

P. M. Norris, Z. C. Leseman, J. T. Gaskins and P. E. Hopkins, "Size Effects on the Thermal Conductivity of Amorphous Silicon Thin Films", *Physical Review B*, Vol. 93, No. 14, p. 140201, 2016.

26. Cahill, D. G., "Thermal Conductivity Measurement from 30 to 750 K: the 3ω Method", *Review of Scientific Instruments*, Vol. 61, No. 2, pp. 802–808, 1990.

27. Shoemaker, D. C., Y. Song, A. Karim, P. Ghanizadeh, N. Donmezer, J. H. Park, D. W. Jeon, H. K. Lee, J. K. Mun and S. Choi, "Decentralization of the Heating in Multi-Finger α-Ga2o3 Ultra-Wide Bandgap Electronics", *IEEE Electron Device Letters*, Vol. 46, No. 2, pp. 266–269, 2025.

28. Cahill, D. G., W. K. Ford, K. E. Goodson, G. D. Mahan, A. Majumdar, H. J. Maris, R. Merlin and S. R. Phillpot, "Nanoscale Thermal Transport", *Journal of Applied Physics*, Vol. 93, No. 2, pp. 793–818, 2003.

29. Jiang, J.-W., B.-S. Wang and J.-S. Wang, "Molecular Dynamics Simulation for Heat Transport in Thin Diamond Nanowires", *Physical Review B*, Vol. 83, No. 23, p. 235432, 2011.

30. Sheng, Y., Y. Hu, Z. Fan and H. Bao, "Size Effect and Transient Phonon Transport Mechanism in Approach-To-Equilibrium Molecular Dynamics Simulations", *Physical Review B*, Vol. 105, No. 7, p. 075301, 2022.

31. Wang, J.-S., J. Wang and N. Zeng, "Nonequilibrium Green's Function Approach to Mesoscopic Thermal Transport", *Physical Review B*, Vol. 74, No. 3, p. 033408, 2006.

32. Li, W.-X., K.-Q. Chen, W. Duan, J. Wu and B.-L. Gu, "Phonon Transport and Thermal Conductivity in Dielectric Quantum Wire", *Journal of Physics D: Applied Physics*, Vol. 36, No. 23, p. 3027, 2003.

33. Cepellotti, A. and N. Marzari, "Boltzmann Transport in Nanostructures as a Fric-

tion Effect", *Nano Letters*, Vol. 17, No. 8, pp. 4675–4682, 2017.

34. Li, R., J.-X. Wang, E. Lee and T. Luo, "Physics-Informed Deep Learning for Solving Phonon Boltzmann Transport Equation with Large Temperature Non-Equilibrium", *Npj Computational Materials*, Vol. 8, No. 1, p. 29, 2022.

35. Saurav, S. and S. Mazumder, "Extraction of Thermal Conductivity Using Phonon Boltzmann Transport Equation Based Simulation of Frequency Domain Thermo-Reflectance Experiments", *International Journal of Heat and Mass Transfer*, Vol. 204, No. 1, p. 123871, 2023.

36. Chen, K.-Q., X.-H. Wang and B.-Y. Gu, "Localized Folded Acoustic Phonon Modes in Coupled Superlattices with Structural Defects", *Physical Review B*, Vol. 61, No. 18, p. 12075, 2000.

37. Hopkins, P. E. and P. M. Norris, "Contribution of Ballistic Electron Transport to Energy Transfer During Electron-Phonon Nonequilibrium in Thin Metal Films", *Journal of Heat Transfer*, Vol. 131, No. 4, p. 043208, 2009.

38. Ziman, J. M., *Electrons and Phonons: the Theory of Transport Phenomena in Solids*, Oxford University Press, Oxford, 2001.

39. Sverdrup, P. G., S. Sinha, M. Asheghi, S. Uma and K. E. Goodson, "Measurement of Ballistic Phonon Conduction Near Hotspots in Silicon", *Applied Physics Letters*, Vol. 78, No. 21, pp. 3331–3333, 2001.

40. Sinha, S., E. Pop, R. W. Dutton and K. E. Goodson, "Non-Equilibrium Phonon Distributions in Sub-100 nm Silicon Transistors", *Journal of Heat Transfer*, Vol. 128, No. 7, pp. 638–647, 2006.

41. Peterson, R., "Direct Simulation of Phonon-Mediated Heat Transfer in a Debye Crystal", *Nanoscale and Microscale Thermophysical Engineering*, Vol. 116, No. 4, pp. 815–822, 1994.

42. Mazumder, S. and A. Majumdar, "Monte Carlo Study of Phonon Transport in Solid Thin Films Including Dispersion and Polarization", *Journal of Heat Transfer*, Vol. 123, No. 4, pp. 749–759, 2001.

43. Wong, B. T., M. Francoeur and M. P. Mengüç, "A Monte Carlo Simulation for Phonon Transport within Silicon Structures at Nanoscales with Heat Generation", *International Journal of Heat and Mass Transfer*, Vol. 54, No. 9-10, pp. 1825–1838, 2011.

44. Wang, T. and J. Y. Murthy, "Solution of the Phonon Boltzmann Transport Equation Employing Rigorous Implementation of Phonon Conservation Rules", *ASME International Mechanical Engineering Congress and Exposition*, Vol. 3, pp. 463–471, Chicago, USA, 2006.

45. Mittal, A. and S. Mazumder, "Monte Carlo Study of Phonon Heat Conduction in Silicon Thin Films Including Contributions of Optical Phonons", *Journal of Heat Transfer*, Vol. 132, No. 5, pp. 052402–1, 2010.

46. Mittal, A., *Prediction of Non-Equilibrium Heat Conduction in Crystalline Materials Using the Boltzmann Transport Equation for Phonons*, Ph.D. Thesis, The Ohio State University, 2011.

47. Shao, C., T. Hori and J. Shiomi, "P-Trans: a Monte Carlo Ray-Tracing Software to Simulate Phonon Transport in Arbitrary Nanostructures", *Computer Physics Communications*, Vol. 276, No. 1, p. 108361, 2022.

48. Hua, Y.-C., H.-L. Li and B.-Y. Cao, "Thermal Spreading Resistance in Ballistic-Diffusive Regime for GaN HEMTs", *IEEE Transactions on Electron Devices*, Vol. 66, No. 8, pp. 3296–3301, 2019.

49. Shen, Y., Y.-C. Hua, H.-L. Li, S. L. Sobolev and B.-Y. Cao, "Spectral Thermal Spreading Resistance of Wide-Bandgap Semiconductors in Ballistic-Diffusive

Regime", *IEEE Transactions on Electron Devices*, Vol. 69, No. 6, pp. 3047–3054, 2022.

50. Pop, E., "Monte Carlo Transport and Heat Generation in Semiconductors", *Annual Review of Heat Transfer*, Vol. 17, pp. 385–423, 2014.

51. Chandrasekhar, S., *Radiative Transfer*, Dover Publications Inc., New York, 1960.

52. Lathrop, K. D. and B. G. Carlson, *Discrete Ordinates Angular Quadrature of the Neutron Transport Equation*, Tech. rep., Los Alamos National Lab. (LANL), Los Alamos, NM, USA, 1964.

53. Modest, M. F., S. Mazumder, M. Modest and S. Mazumder, *Fundamentals of Thermal Radiation*, Elsevier, Merced, USA, 2003.

54. Jendoubi, S., H. S. Lee and T.-K. Kim, "Discrete Ordinates Solutions for Radiatively Participating Media in a Cylindrical Enclosure", *Journal of Thermophysics and Heat Transfer*, Vol. 7, No. 2, pp. 213–219, 1993.

55. Joshi, A. A. and A. Majumdar, "Transient Ballistic and Diffusive Phonon Heat Transport in Thin Films", *Journal of Applied Physics*, Vol. 74, No. 1, pp. 31–39, 1993.

56. De Tomas, C., A. Cantarero, A. F. Lopeandia and F. X. Alvarez, "From Kinetic to Collective Behavior in Thermal Transport on Semiconductors and Semiconductor Nanostructures", *Journal of Applied Physics*, Vol. 115, No. 16, p. 164314, 2014.

57. De Tomas, C., A. Cantarero, A. F. Lopeandia and F. X. Alvarez, "Enhancing of Optic Phonon Contribution in Hydrodynamic Phonon Transport", *Journal of Applied Physics*, Vol. 118, No. 13, p. 134305, 2015.

58. Guyer, R. A. and J. Krumhansl, *Solution of the Linearized Phonon Boltzmann Equation*, APS, New York, USA, 1966.

59. Beardo, A., S. Alajlouni, L. Sendra, J. Bafaluy, A. Ziabari, Y. Xuan, J. Camacho, A. Shakouri and F. X. Alvarez, "Hydrodynamic Thermal Transport in Silicon at Temperatures Ranging from 100 to 300 K", *Physical Review B*, Vol. 105, No. 16, p. 165303, 2022.

60. Alvarez, P. T., *Thermal Transport in Semiconductors: First Principles and Phonon Hydrodynamics*, Springer, New York, USA, 2018.

61. Sendra, L., A. Beardo, P. Torres, J. Bafaluy, F. X. Alvarez and J. Camacho, "Derivation of a Hydrodynamic Heat Equation from the Phonon Boltzmann Equation for General Semiconductors", *Physical Review B*, Vol. 103, No. 14, p. L140301, 2021.

62. Beardo, A., M. Calvo-Schwarzwälder, J. Camacho, T. G. Myers, P. Torres, L. Sendra, F. X. Alvarez and J. Bafaluy, "Hydrodynamic Heat Transport in Compact and Holey Silicon Thin Films", *Physical Review Applied*, Vol. 11, No. 3, p. 034003, 2019.

63. Zeng, L., K. C. Collins, Y. Hu, M. N. Luckyanova, A. A. Maznev, S. Huberman, V. Chiloyan, J. Zhou, X. Huang, K. A. Nelson and G. Chen, "Measuring Phonon Mean Free Path Distributions by Probing Quasiballistic Phonon Transport in Grating Nanostructures", *Scientific Reports*, Vol. 5, No. 1, p. 17131, 2015.

64. Hua, Y.-C. and B.-Y. Cao, "The Effective Thermal Conductivity of Ballistic-Diffusive Heat Conduction in Nanostructures with Internal Heat Source", *International Journal of Heat and Mass Transfer*, Vol. 92, No. 1, pp. 995–1003, 2016.

65. Volz, S., R. Carminati, P. Chantrenne, S. Dilhaire, S. Gomez, N. Trannoy and G. Tessier, *Microscale and Nanoscale Heat Transfer*, Springer, New York, USA, 2007.

66. Singh, D., *Frequency and Polarization Resolved Phonon Transport in Carbon and*

Silicon Nanostructures, Ph.D. Thesis, Purdue University, 2011.

67. Donmezer, F., *Multiscale Electro-Thermal Modeling of AlGaN/GaN Heterostructure Field Effect Transistors*, Ph.D. Thesis, Georgia Institute of Technology, 2013.

68. Meydando, T., A. Abdolhosseinzadeh, E. Goktepe, M. V. Milošević and N. Donmezer, "Laser-Induced Thermal Size Effects in Micro-Raman Thermal Conductivity Measurements", *Applied Physics Letters*, Vol. 126, No. 5, 2025.

69. Li, H.-L., Y. Shen, Y.-C. Hua, S. L. Sobolev and B.-Y. Cao, "Hybrid Monte Carlo-Diffusion Studies of Modeling Self-Heating in Ballistic-Diffusive Regime for Gallium Nitride HEMTs", *Journal of Electronic Packaging*, Vol. 145, No. 1, p. 011203, 2023.

70. Fiveland, W. A., "The Selection of Discrete Ordinate Quadrature Sets for Anisotropic Scattering", *Fundamentals of Radiation Heat Transfer*, Vol. 160, pp. 89–96, 1991.

71. Donmezer, F. N., D. Singh, W. James, A. Christensen, S. Graham and J. Y. Murthy, "Lattice Boltzmann and Discrete Ordinates Methods for Phonon Transport Modeling: a Comparative Study", *ASME International Mechanical Engineering Congress and Exposition*, Vol. 64008, pp. 333–343, Denver, USA, 2011.

72. Ellison, G. N., *Thermal Computations for Electronic Equipment*, Krieger, Malabar, 1984.

73. Azarifar, M. and N. Donmezer, "A Multiscale Analytical Correction Technique for Two-Dimensional Thermal Models of AlGaN/GaN HEMTs", *Microelectronics Reliability*, Vol. 74, No. 1, pp. 82–87, 2017.

74. Bagnall, K. R., Y. S. Muzychka and E. N. Wang, "Application of the Kirchhoff Transform to Thermal Spreading Problems with Convection Boundary Conditions", *IEEE Transactions on Components, Packaging and Manufacturing Technology*, Vol. 4, No. 3, pp. 408–420, 2013.

75. Razavi, M., Y. S. Muzychka and S. Kocabiyik, "Review of Advances in Thermal Spreading Resistance Problems", *Journal of Thermophysics and Heat Transfer*, Vol. 30, No. 4, pp. 863–879, 2016.

76. Hua, Y.-C. and B.-Y. Cao, "Slip Boundary Conditions in Ballistic-Diffusive Heat Transport in Nanostructures", *Nanoscale and Microscale Thermophysical Engineering*, Vol. 21, No. 3, pp. 159–176, 2017.

77. Dundar, C., D. Kara and N. Donmezer, "The Effects of Gate-Connected Field Plates on Hotspot Temperatures of AlGaN/GaN HEMTs", *IEEE Transactions on Electron Devices*, Vol. 67, No. 1, pp. 57–62, 2019.

78. Laaksonen, K., M. G. Ganchenkova and R. M. Nieminen, "Vacancies in Wurtzite GaN and AlN", *Journal of Physics: Condensed Matter*, Vol. 21, No. 1, p. 015803, 2008.

79. Garg, J., T. Luo and G. Chen, "Spectral Concentration of Thermal Conductivity in GaN—A First-Principles Study", *Applied Physics Letters*, Vol. 112, No. 25, p. 252101, 2018.

80. Liu, W., A. A. Balandin, C. Lee and H.-Y. Lee, "Increased Thermal Conductivity of Free-Standing Low-Dislocation-Density GaN Films", *Physica Status Solidi (a)*, Vol. 202, No. 12, pp. R135–R137, 2005.

81. Simon, R. B., J. Anaya and M. Kuball, "Thermal Conductivity of Bulk GaN—Effects of Oxygen, Magnesium Doping, and Strain Field Compensation", *Applied Physics Letters*, Vol. 105, No. 20, p. 202105, 2014.

82. Freedman, J. P., J. H. Leach, E. A. Preble, Z. Sitar, R. F. Davis and J. A. Malen, "Universal Phonon Mean Free Path Spectra in Crystalline Semiconductors at High Temperature", *Scientific Reports*, Vol. 3, No. 1, p. 2963, 2013.

83. Whitman, N. H., T. S. Palmer, P. A. Greaney, S. A. Hosseini, D. E. Burkes

and D. J. Senor, "Gray Phonon Transport Prediction of Thermal Conductivity in Lithium Aluminate with Higher-Order Finite Elements on Meshes with Curved Surfaces", *Journal of Computational and Theoretical Transport*, Vol. 50, No. 5, pp. 483–506, 2021.

84. Torres, P., A. Torelló, J. Bafaluy, J. Camacho, X. Cartoixà and F. X. Alvarez, "First Principles Kinetic-Collective Thermal Conductivity of Semiconductors", *Physical Review B*, Vol. 95, No. 16, p. 165407, 2017.

85. Perdew, J. P., E. R. McMullen and A. Zunger, "Density-Functional Theory of the Correlation Energy in Atoms and Ions: a Simple Analytic Model and a Challenge", *Physical Review a*, Vol. 23, No. 6, p. 2785, 1981.

86. Giannozzi, P., S. Baroni, N. Bonini, M. Calandra, R. Car, C. Cavazzoni, D. Ceresoli, G. L. Chiarotti, M. Cococcioni, I. Dabo, A. Dal Corso, S. de Gironcoli, S. Fabris, G. Fratesi, R. Gebauer, U. Gerstmann, C. Gougoussis, A. Kokalj, M. Lazzeri, L. Martin-Samos, N. Marzari, F. Mauri, R. Mazzarello, S. Paolini, A. Pasquarello, L. Paulatto, C. Sbraccia, S. Scandolo, G. Sclauzero, A. P. Seitsonen, A. Smogunov, P. Umari and R. M. Wentzcovitch, "QUANTUM ESPRESSO: a Modular and Open-Source Software Project for Quantum Simulations of Materials", *Journal of Physics: Condensed Matter*, Vol. 21, No. 39, p. 395502, 2009.

87. Kohn, W. and L. J. Sham, "Self-Consistent Equations Including Exchange and Correlation Effects", *Physical Review*, Vol. 140, No. 4A, p. A1133, 1965.

88. Hohenberg, P. and W. Kohn, "Inhomogeneous Electron Gas", *Physical Review*, Vol. 136, No. 3B, p. B864, 1964.

89. Zhu, Y., J. Xie, A. Pei, B. Liu, Y. Wu, D. Lin, J. Li, H. Wang, H. Chen, J. Xu, A. Yang, C.-L. Wu, H. Wang, W. Chen and Y. Cui, "Fast Lithium Growth and Short Circuit Induced by Localized-Temperature Hotspots in Lithium Batteries", *Nature Communications*, Vol. 10, No. 1, p. 2067, 2019.

90. Xu, S., Y. Xu, J. Zhang, J. Gao, X. Wang, X. Zhang and Y. Yue, "Ballistic Transport Enhanced Heat Convection at Nanoscale Hotspots", *Journal of Applied Physics*, Vol. 136, No. 16, p. 164306, 2024.

91. Zhang, C., Z. Xin, Q. Lou and H. Liang, *Effects of Heating Strategies and Ballistic Transport on the Transient Thermal Conduction in 3D FinFETs*, Tech. rep., Cornell University, New York,USA, 2025.

92. Luo, X. and R. Hu, "Chip Packaging: Encapsulation of Nitride LEDs", *Nitride Semiconductor Light-Emitting Diodes (LEDs)*, pp. 441–481, Elsevier, Wuhan, China, 2014.

93. Ashcroft, N. W. and N. D. Mermin, *Solid State*, Holt, Rinehart and Winston, New York, 1976.

94. Balandin, A. A., "Thermal Properties of Graphene and Nanostructured Carbon Materials", *Nature Materials*, Vol. 10, No. 8, pp. 569–581, 2011.

95. Balandin, A. A., S. Ghosh, W. Bao, I. Calizo, D. Teweldebrhan, F. Miao and C. N. Lau, "Superior Thermal Conductivity of Single-Layer Graphene", *Nano Letters*, Vol. 8, No. 3, pp. 902–907, 2008.

96. Koh, Y. K., S. L. Singer, W. Kim, J. M. O. Zide, H. Lu, D. G. Cahill, A. Majumdar and A. C. Gossard, "Comparison of the 3ω Method and Time-Domain Thermoreflectance for Measurements of the Cross-Plane Thermal Conductivity of Epitaxial Semiconductors", *Journal of Applied Physics*, Vol. 105, No. 5, p. 054303, 2009.

97. Jiang, P., X. Qian and R. Yang, "Tutorial: Time-Domain Thermoreflectance (TDTR) for Thermal Property Characterization of Bulk and Thin Film Materials", *Journal of Applied Physics*, Vol. 124, No. 16, p. 161103, 2018.

98. Choudhary, K., K. F. Garrity, A. C. E. Reid, B. DeCost, A. J. Biacchi, A. R. Hight Walker, Z. Trautt, J. Hattrick-Simpers, A. G. Kusne, A. Centrone, A. Davy-

dov, J. Jiang, R. Pachter, G. Cheon, E. Reed, A. Agrawal, X. Qian, V. Sharma, H. Zhuang, S. V. Kalinin, B. G. Sumpter, G. Pilania, P. Acar, S. Mandal, K. Haule, D. Vanderbilt, K. Rabe and F. Tavazza, "The Joint Automated Repository for Various Integrated Simulations (JARVIS) for Data-Driven Materials Design", *Npj Computational Materials*, Vol. 6, No. 1, p. 173, 2020.

99. Bao, H., J. Chen, X. Gu and B. Cao, "A Review of Simulation Methods in Micro/nanoscale Heat Conduction", *ES Energy & Environment*, Vol. 1, No. 1, pp. 16–55, 2018.

APPENDIX A: NUMERICAL IMPLEMENTATION AND PARAMETERS

This appendix provides numerical simulation details, including input parameters and software implementation. Tables A.1-A.4 summarize all information used in COMSOL and MATLAB simulations across the four chapters.

Table A.1. Model geometry, material properties, and boundary conditions used for KCM verification simulations.

Property list		Case				
		1	2	3		
Geometry characteristics	Length (μm)	500	500	500	Heat generation	200
	Height (μm)	1000	1000	1000		200
Boundary conditions		Top boundary = 310K & Eq. (3.9)	Top boundary = heat flux & Eq. (3.9)	Top boundary = adiabatic & Eq. (3.9)		
Material properties	Nonlocal length (nm)	185	185	185		
	Thermal conductivity (W/m.K)	150	150	150		
Equations		3.7 & 3.8	3.7 & 3.8	3.7 & 3.8		
Mesh details	Quadrilateral	536576	536576	618223		
	Edge elements	3096	3096	3782		

Table A.2. Model geometry, material properties, and boundary conditions used for KCM performance analysis.

Property list		Solution method							
		FVDOM				KCM			
		Case							
		1	2			1	2		
Geometry characteristics	Length (μm)	0.5	0.5	Heat generation	0.2	0.5	0.5	Heat generation	0.2
	Height (μm)	1	1		0.2	1	1		0.2
Boundry conditions		Top boundary = 310K	Top boundary = adiabatic			Top boundary = 310K & Eq. (3.9)	Top boundary = adiabatic & Eq. (3.9)		
Material properties	Nonlocal length = MFP (nm)	185	185			185	185		
	Thermal conductivity (W/m.K)	150	150			150	150		
Equations		4.15	4.15			3.7 & 3.8	3.7 & 3.8		
Mesh details	Quadrilateral	24000	24000			826826	2072576		
	Edge elements	-	-			3846	6920		
S_N quadrature set		S_8	S_8			-	-		

Table A.3. Model geometry, material properties, and boundary conditions used for simulations of developing semi-empirical relation for localized heating resistance.

Geometry characteristics	**Length (μm)**	**160**	**Heat generation**	**1.6**
	Height (μm)	8		0.16
Boundry conditions		Top boundary = adiabatic		
Material properties	Phonon MFP (nm)	1612		
	Thermal conductivity (W/m.K)	253		
Equations		4.15		
S_N quadrature set		S_6		
Mesh details	Quadrilateral	320000		

Table A.4. Model geometry, material properties, and boundary conditions used for real device simulation.

Property list		**Solution method**	
		FVDOM	KCM
Geometry characteristics	Length (μm)	5.7	5.7
	Height (μm)	3	3
Boundry conditions		Bottom boundary = adiabatic	Bottom boundary = adiabatic & Eq. (3.9)
Material properties	Nonlocal length = MFP (nm)	557	557
	Thermal conductivity (W/m.K)	273	273
Equations		4.15	3.7 & 3.8
Mesh details	Quadrilateral	171000	2820096
	Edge elements	-	7056
S_N quadrature set		S_8	-

The numerical simulations using the KCM approach were carried out in COMSOL Multiphysics, taking advantage of its flexible PDE solving capabilities. Specifically, the transport and energy equations governing the system were implemented and solved using the Coefficient-Form PDE module, which allows for a systematic formulation of coupled partial differential equations. Within the COMSOL interface, three distinct dependent variables were defined to represent the coupled system of equations, enabling the software to construct and solve these equations in matrix form. This setup, illustrated in Figure A.1, ensures that the complex interactions between energy transport, boundary conditions, and material properties are accurately captured within the numerical framework.

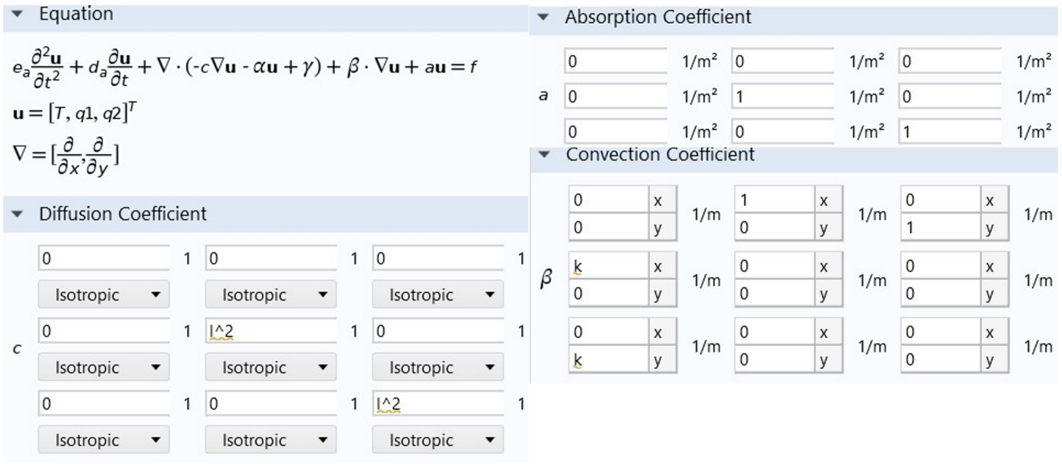

Figure A.1. COMSOL interface for implementing the equations of the KCM model.

MATLAB software was used to implement the FVDOM solution, which used an iterative solver for the discretized form of the phonon BTE. We used the developed code to study size effects caused by boundary scattering and localized heating. The code based on FVDOM is implemented and presented below.

```
clc;
close all;
clear all;

% solver settings
tol = 1e-10;          % solver tolerance
maxiter = 100000;     % maximum solver iterations
EC_Tol=1e-10;         % tolerance for conservation of scattering matrix
ludroptol = 1e-3;
setup.droptol=1e-3;   % drop tolerance for partial lu decomposition
that preconditions the gmres solver
initialgmrestol = 1e-4;   % initial tolerance for the gmres solver
gmrestolmultiplier = 1e-3; % ratio of solver strength

% boundary conditions
```

```
Tleft = 300;   % Tavl temperature at left boundary
Tright = 300;  % Tavr " right "
Ttop = 310;    % Tavt " top "
Tbottom = 300; % Tavb " bottom "
% Tbotf = Tbottom;

% domain size
lx = 1e-6;  % domain size in the x direction [m]
ly = 1e-6;  % domain size in the y direction [m]

scheme = 'LUS';

cLight = 299792458;  % speed of light [m/s]

% mesh structure
Nx = 100;   % number of cells in the x direction
Ny = 100;   % number of cells in the y direction
dx = lx/Nx; % cell spacing in the x direction
dy = ly/Ny; % " in the y direction
x = dx*((1:Nx)-1/2);    % x cell centroid coordinates
y = dy*((Ny:-1:1)-1/2); % y cell centroid coordinates
xi = dx*(0:Nx);    % x cell face coordinates
yi = dy*(Ny:-1:0); % y cell face coordinates
[X,Y] = meshgrid(x,y);     % matrix of cell centroid coordinates
[Xi,Yi] = meshgrid(xi,yi); % matrix of cell face coordinates

% material properties (thermal)
% Si
conductivity = 150;      % [W/m/K]
mfp = 185e-9;            % phonon mean free path [m]
```

```
q = zeros(Ny,Nx);
GenField=flip(q);
G=sum(sum(GenField*dy*dx));   % total generation [W/m]
disp(['Total generation: ' num2str(G) ' W/m']);

% calculate other phonon properties
btbCv = 3.570714116574253e+07;    % load specific heats
btbomega = 3.834591198065119e+13; % load frequency
btbvg = 3*conductivity/btbCv/mfp; % calculate group velocity
Pgg = (btbvg^2)*(btbCv^2)/(3*conductivity*btbomega^2);   % calculate
scattering matrix (using "conductivity")
Pgg = btbCv*btbvg/btbomega/btbomega/mfp; % calculate scattering matrix
(using "mfp")
bands = length(btbomega);  % set the number of bands

% select ordinate set
ord = OrdinatesSN('6');       % Sn quadratures, options are 3,6, and 8
directions = ord.nDirections; % set number of directions

nGI = directions*bands;  % number of angular degrees of freedom
Nc = Nx*Ny;              % number of spatial degrees of freedom

disp([num2str(nGI*Nc) ' degrees of freedom. (' num2str(directions) '
directions, ' num2str(bands) ' bands, ' num2str(Nc) ' cells)']);

Tleft(1,1:Ny) = Tleft;     % left temperature
Tright(1,1:Ny) = Tright;   % right temperature
Ttop(1,1:Nx) = Ttop;       % bottom temperature
Tbottom(1,1:Nx) = Tbottom; % top temperature

Cv = reshape(ones(directions,1)*btbCv',nGI,1); % Cv=btbCv; extend
```

```
specific heats to directions
eleft = Cv*Tleft;     % set left boundary energy
etop = Cv*Ttop;       % set top boundary energy
ebottom = Cv*Tbottom; % set bottom boundary energy
eright = Cv*Tright;   % set right boundary energy

% set top reflection on or off
topReflection = false;
bottomReflection = false;
leftReflection = false;

% form scattering matrix
% cg = btbCv.*btbvg./btbomega;
% conductivity = 1/3*sum(btbvg.*(Agg\cg)); % W/m/K
Agg = Pgg*diag(btbomega./btbCv);
K = (kron(diag(btbomega)*Pgg*diag(btbomega./btbCv),
diag(ones(directions,1)))-kron(diag(btbomega)*(Pgg*btbomega/sum(btbCv)*
ones(1,bands)),ones(directions,1)*ord.dWeights'));
% K is in units of 1/s

% check scattering matrix for energy conservation properties
if (norm(K*Cv) > EC_Tol*norm(K,'fro')*norm(Cv) ||
norm(kron(ones(bands,1),ord.dWeights)'*K) > EC_Tol*norm(K))
error('Logic error: Scattering matrix is non-conservative.');
end

% generate coefficents
aEW = kron(btbvg/dx,ord.dvVectors(:,1));
aNS = kron(btbvg/dy,ord.dvVectors(:,2));
pNS = kron(ones(bands,1),ord.dvVectors(:,2))>0;
nNS = kron(ones(bands,1),ord.dvVectors(:,2))<0;
```

```
pEW = kron(ones(bands,1),ord.dvVectors(:,1))>0;
nEW = kron(ones(bands,1),ord.dvVectors(:,1))<0;

switch(scheme)
    case 'UDS'
    % UDS
    Lww = zeros(bands*directions,1);
    Lw = aEW.*pEW; %1/s
    Lss = zeros(bands*directions,1);
    Ls = aNS.*pNS;
    Lee = zeros(bands*directions,1);
    Le = -aEW.*nEW;
    Lnn = zeros(bands*directions,1);
    Ln = -aNS.*nNS;
    Lp = aEW.*pEW-aEW.*nEW+aNS.*pNS-aNS.*nNS;

    case 'QUICK'
    % QUICK SCHEME
    Lww = -aEW.*pEW/8;
    Lw = 7*aEW.*pEW/8+3*aEW.*nEW/8;
    Lee = aEW.*nEW/8;
    Le = -3*aEW.*pEW/8-7*aEW.*nEW/8;
    Lss = -aNS.*pNS/8;
    Ls = 7*aNS.*pNS/8+3*aNS.*nNS/8;
    Lnn = aNS.*nNS/8;
    Ln = -3*aNS.*pNS/8-7*aNS.*nNS/8;
    Lp = 3*aEW.*pEW/8-3*aEW.*nEW/8+3*aNS.*pNS/8-3*aNS.*nNS/8;
    Lsr = aNS.*pNS;

    case 'LUS'
    % LUS
```

```
    Lww =-0.5*aEW.*pEW;
    Lw = 2*aEW.*pEW; %1/s
    Lss = -0.5*aNS.*pNS;
    Ls = 2*aNS.*pNS;
    Le = -2*aEW.*nEW;
    Lee = +0.5*aEW.*nEW;
    Lnn = +0.5*aNS.*nNS;
    Ln = -2*aNS.*nNS;
    Lp = 1.5*aEW.*pEW-1.5*aEW.*nEW+1.5*aNS.*pNS-1.5*aNS.*nNS;
end

% set generation for each band
Gp = cell(bands,1);
for i=1:bands
Gp{i} = sparse(Ny,Nx);%GenField  % set most bands to zero generation
end
% put generation into highest band only
Gp{bands} = GenField;

disp('Setup and Factorization');
tic;
Ait = cell(nGI,1);   % coefficient matrix for each band and direction
Bit = cell(nGI,1);   % scattering matrix for each band and direction
Bbdit = cell(nGI,1); % right hand side matrix
Brefl1 = zeros(nGI,1); % reflection coefficient
BBrefl1 = zeros(nGI,1);
Trefl1 = zeros(nGI,1);
TTrefl1 = zeros(nGI,1);
lBrefl1 = zeros(nGI,1); % reflection coefficient
lBBrefl1 = zeros(nGI,1);
lRefl = cell(nGI,1);
```

```
Refl = cell(nGI,1);

% boundary matrices
bS = spdiags(reshape(sparse(Ny*ones(1,Nx),1:Nx,1,Ny,Nx)',Nc,1),0,Nc,Nc)
bSS = spdiags(reshape(sparse((Ny-1)*ones(1,Nx),1:Nx,1,Ny,Nx)',Nc,1),
0,Nc,Nc);
bN = spdiags(reshape(sparse(ones(1,Nx),1:Nx,1,Ny,Nx)',Nc,1),0,Nc,Nc);
bNN = spdiags(reshape(sparse(2*ones(1,Nx),1:Nx,1,Ny,Nx)',Nc,1),0,Nc,Nc)
bE = spdiags(reshape(sparse(1:Ny,Nx*ones(1,Ny),1,Ny,Nx)',Nc,1),0,Nc,Nc)
bEE = spdiags(reshape(sparse(1:Ny,(Nx-1)*ones(1,Ny),1,Ny,Nx)',Nc,1)
,0,Nc,Nc);
bW = spdiags(reshape(sparse(1:Ny,ones(1,Ny),1,Ny,Nx)',Nc,1),0,Nc,Nc);
bWW = spdiags(reshape(sparse(1:Ny,2*ones(1,Ny),1,Ny,Nx)',Nc,1),0,Nc,Nc)

% LU decomposition matrices
L = cell(nGI,1);
U = cell(nGI,1);

if (topReflection)
    topReflContr = zeros(1,Nx);
    topreflCoef = 1;
    Trefl2 = ord.dWeights.*(ord.dvVectors(:,2)>=0);
    Trefl = bN;
    TTrefl = bNN;
    topfourierAdj = -1;
else
    topReflContr = ones(1,Nx);
    topreflCoef = 0;
    Trefl2 = zeros(directions,1);
    Trefl = sparse(Nc,Nc);
    TTrefl = sparse(Nc,Nc);
```

```
    topfourierAdj = 1;
end

if (bottomReflection)
    bottomReflContr = zeros(1,Nx);
    bottomreflCoef = 1;
    Brefl2 = ord.dWeights.*(ord.dvVectors(:,2)<=0);
    Brefl = bS;
    BBrefl = bSS;
    bottomfourierAdj = -1;
else
    bottomReflContr = ones(1,Nx);
    bottomreflCoef = 0;
    Brefl2 = zeros(directions,1);
    Brefl = sparse(Nc,Nc);
    BBrefl = sparse(Nc,Nc);
    bottomfourierAdj = 1;
end

if (leftReflection)
    leftReflContr = zeros(1,Ny);
    leftreflCoef = 1;
    Lrefl2 = ord.dWeights.*(ord.dvVectors(:,1)<=0);
    Lrefl = bE;
    LLrefl = bEE;
    leftfourierAdj = -1;
else
    leftReflContr = ones(1,Ny);
    leftreflCoef = 0;
    Lrefl2 = zeros(directions,1);
    Lrefl = sparse(Nc,Nc);
```

```
    LLrefl = sparse(Nc,Nc);
    leftfourierAdj = 1;
end

for n=1:nGI
    % can be a parallel loop... parfor
    % construct matrices
    band = floor((n-1)/directions)+1; % find band

    % construct coefficient matrix
    Lew = spdiags(ones(Nx,1)*[-Lww(n) -Lw(n) K(n,n)+Lp(n) -Le(n)
    -Lee(n)],[-2 -1 0 1 2],Nx,Nx);
    Iew = eye(Ny);
    Lns = spdiags(ones(Ny,1)*[-Lnn(n) -Ln(n) -Ls(n) -Lss(n)]
    ,[-2 -1 1 2],Ny,Ny);
    Ins = eye(Nx);
    Ait{n} = kron(Iew,Lew)+kron(Lns,Ins);

    % reflection coefficient
    Brefl1(n) = bottomreflCoef*(Ls(n)+Lss(n))/(1-sum(ord.dWeights.*
    (ord.dvVectors(:,2)>0)));
    BBrefl1(n) = bottomreflCoef*Lss(n)/(1-sum(ord.dWeights.*
    (ord.dvVectors(:,2)>0)));

    Trefl1(n) = topreflCoef*(Ln(n)+Lnn(n))/(1-sum(ord.dWeights.*
    (ord.dvVectors(:,2)<0)));
    TTrefl1(n) = topreflCoef*Lnn(n)/(1-sum(ord.dWeights.*
    (ord.dvVectors(:,2)<0)));

    Lrefl1(n) = leftreflCoef*(Lw(n)+Lww(n))/(1-sum(ord.dWeights.*
    (ord.dvVectors(:,1)<0)));
```

```
  LLrefl1(n) = leftreflCoef*Lww(n)/(1-sum(ord.dWeights.*
  (ord.dvVectors(:,1)<0)));

  Refl{n} = Brefl1(n)*Brefl + BBrefl1(n)*BBrefl + Trefl1(n)*Trefl +
  TTrefl1(n)*TTrefl + Lrefl1(n)*Lrefl + LLrefl1(n)*LLrefl;

  % construct right hand sides
  % A*e = b
  % b = eoff*Bit + Brefl*efull + Bbdit
  % Bit is a vector that is used to calculate scattering terms
  given the off diagonal energies
  % Bbdit is a vector of boundary terms and generation terms

  Bit{n} = -[K(n,1:(n-1)) 0 K(n,(n+1):nGI)]';
  BoundMat = sparse([ones(1,Nx),1:Ny,Ny*ones(1,Nx),1:Ny,2*ones(1,Nx),
  1:Ny,(Ny-1)*ones(1,Nx),1:Ny],...
  [1:Nx,ones(1,Ny),1:Nx,Nx*ones(1,Ny),1:Nx,2*
  ones(1,Ny),1:Nx,(Nx-1)*ones(1,Ny)],...
  [(Ln(n)+Lnn(n))*etop(n)*topReflContr,...%top
  (Lw(n)+Lww(n))*eleft(n)*leftReflContr,...%left
  (Ls(n)+Lss(n))*ebottom(n)*bottomReflContr,...%bottom
  (Le(n)+Lee(n))*eright(n,:),...%right
  Lnn(n)*etop(n)*topReflContr,...
  Lww(n)*eleft(n)*leftReflContr,...
  Lss(n)*ebottom(n)*bottomReflContr,... %bottom
  Lee(n)*eright(n,:)],Ny,Nx);

Bir=0;

  % include generation term
  Bbdit{n} = reshape(BoundMat'+Gp{band}',Nc,1);
```

```
    [L{n},U{n}] = lu(Ait{n});
end
toc;
% clear Lew Lns Iew Ins ;

% we want to make the initial guess a fully diffusive temperature
% gradient...  should make a function that returns that for the
% temperatures at the boundaries
% construct diffusive coefficient matrix

DiffDx = spdiags(dy/dx*ones(Nx,1)*[-1 2 -1],[-1 0 1],Nx,Nx);
DiffIx = speye(Nx);
DiffDy = spdiags(dx/dy*ones(Ny,1)*[-1 2 -1],[-1 0 1],Ny,Ny);
DiffIy = speye(Ny);
DiffA = kron(DiffIy,DiffDx)+kron(DiffDy,DiffIx);  % Interiror
coeffmatrix for all nodes
% construct diffusive boundary modifications
DiffBM = sparse([ones(1,Nx),1:Ny,Ny*ones(1,Nx),1:Ny],...
[1:Nx,ones(1,Ny),1:Nx,Nx*ones(1,Ny)],...
[dx/dy*ones(1,Nx)*(1),...            % top
dy/dx*ones(1,Ny)*(1),...             % left
dx/dy*ones(1,Nx)*(1),...             % remove -1 for prescribed temp.
dy/dx*ones(1,Ny)*(1)]);
% GenMat = sparse(Ny,Nx);
GenMat = GenField*dx*dy/conductivity;
% modify coefficient matrix for the boundaries
DiffA = DiffA+spdiags(reshape(DiffBM',Nc,1),0,Nc,Nc);

% construct right hand sides
DiffB = sparse([ones(1,Nx),1:Ny,Ny*ones(1,Nx),1:Ny],...
[1:Nx,ones(1,Ny),1:Nx,Nx*ones(1,Ny)],...
```

```
[2*Tbottom*dx/dy.*ones(1,Nx),...  % top 2*Tbottom*dx/dy*ones(1,Nx)
==> Prescribed temp.
2*Tleft*dy/dx.*ones(1,Ny),...  % left 2*Tleft*dy/dx*ones(1,Ny)
==> Prescribed temp.
2*Ttop*dx/dy.*ones(1,Nx),...   % bottom ones for prescribed temp.
2*Tright*dy/dx.*ones(1,Ny)]);  % right 2*Tright*dy/dx*ones(1,Ny)
==> Prescribed temp.
% include generation term
DiffB=reshape(DiffB'+GenMat',Nc,1);
% solve
Tinit=DiffA\DiffB;

disp(num2str(max(Tinit)));

% clear DiffA DiffB DiffBM GenMat;

% SOLVER

% partial iterative solver (solve each direction and band at a time,
% scattering term is a source)
% must have a way of evaluating convergence. sum the change in e
each time as soon as the maximum relative change for any direction is
less than some tolerance, we stop
disp('Iterative Solver');
r = zeros(maxiter,1);               % convergence history
% gmrestol = initialgmrestol;
tic;
% initialize with diffusive temperature gradient
einit=reshape(Tinit*Cv',nGI*Nc,1);
e=einit;
fullB = vertcat(Bbdit{:});  % construct full right hand side
```

```
(for calculating residual)
bnorm = norm(fullB);        % take the norm, don't need to do this
every time
iterations = 0;             % initialize iteration count
B0 = sparse([],[],[],Nc,1); % zero matrix for reflection calculations
% create a progress bar for watching progress
h = waitbar(0,'Initializing...','Name','Solving...','CreateCancelBtn',
'setappdata(gcbf,''canceling'',1)');
setappdata(h,'canceling',0);

for i=1:maxiter           % begin outer loop
    for j=1:10            % begin inner loop
        for band=1:bands  % loop over bands
            BR = B0;      % initialize reflection term
            lBR = B0;
        % calculate reflection term
        % this loop can be inside or outside the direction loop. seems
        % to be faster outside, even though the energies are not
        % updated each direction.
        for k=1:directions
        BR = BR + Brefl2(k)*e(((band-1)*Nc*directions)+
        (((k-1)*Nc+1):(k*Nc))) + Lrefl2(k)*e(((band-1)*Nc*directions)+
        (((k-1)*Nc+1):(k*Nc)));

        end

        for direction=1:directions          % loop over directions
        n = (band-1)*directions+direction;  % set n index (nGI)


        % calculate right hand side (based on reflection,
```

```
        % boundaries, and scattering
        B = scatter(K,e,n) + Bbdit{n} + Refl{n}*BR;
        % solve with preconditioned gmres
        e(((n-1)*Nc+1):(n*Nc)) = U{n}\(L{n}\B);
%       if (flag ~= 0)
%       warning('GMRES failed.');
%       delete(h);
%       return;
%                   end
            end
        end
    end

    T=calcT(e, Nc, nGI, ord.dWeights, directions, bands, Nx, Ny, btbCv);
    Titers(i) = max(max(T));

    % calculate residual (only do this every outer iteration)
    r(i) = norm(AemultR4(e,Ait,Bit,Brefl2,Refl,Bir,bands,directions,Nc)
    -fullB)/bnorm;
    gmrestol=r(i);
    %disp(['Residual norm is ' num2str(r)]);
    if (r(i)<tol)                   % check convergence
        break;                      % if converged, exit loop
    end

    if (i>1 && r(i) >= r(i-1))      % check stagnation
        warning('Convergence stagnated.');
        break;
    end
    if getappdata(h,'canceling')    % check cancelation box
        warning('Solver cancelled, solution may not be converged.');
```

```
        break;
    end
    % calculate progress, and update progress bar
    prog = (log(r(1))-log(r(i)))/(log(r(1))-log(tol));
    waitbar(prog,h,['Progress: ' num2str(round(prog*1000)/10) '%,
    Rnorm=' num2str(r(i))]);
    disp(num2str(Titers(i)));
end


if (i==maxiter)
    warning('Maximum number of iterations reached, solution may not
    be converged.');
end
toc;
delete(h);      % delete progress bar window
clear L U;
disp(['Solver exited with ' num2str(10*i) ' iterations and residual
norm of ' num2str(r(i))]);
e=reshape(e,Nc,nGI)';  % reshape energy vector for easy postprocessing

% POST PROCESSING

% let's calculate the flux leaving the domain.
% first, just calculate flux at all points...
qx = (btbvg'*reshape((ord.dWeights.*ord.dvVectors(:,1))'*
reshape(e,directions,bands*Nc),bands,Nc))';
qy = (btbvg'*reshape((ord.dWeights.*ord.dvVectors(:,2))'*
reshape(e,directions,bands*Nc),bands,Nc))';
qx = reshape(qx,Nx,Ny)';
qy = reshape(qy,Nx,Ny)';
```

```
meanxheatflux = mean(qx((Ny/2),:))
meanxheatfluxbottom = mean(qx((1),:))

eWeighted=ord.dWeights'*reshape(e,directions,bands*Nc);
eTotal = squeeze(sum(reshape(eWeighted,bands,Nx,Ny),1));
T=eTotal'/sum(btbCv);
phononT=reshape((reshape(eWeighted,bands,Nc)./repmat(btbCv,1,Nc))'
,Nx,Ny,bands);

Result=vec2mat(Tinit,Nx);
Result2=vec2mat(T,Nx);

disp(['delta_T_max = ' num2str(abs((max(Result2(:)))-
(max(Result(:)))))]);

% calculating thermal conductivity
disp(['k1 = ' num2str((meanxheatflux*lx)/10) ' W/m/K']);
disp(['k1/k_bulk (%) = ' num2str((meanxheatflux*lx)*100/
(10*conductivity))' %']);
```

APPENDIX B: PHONON THERMAL TRANSPORT PROPERTIES

This section presents key phonon properties derived from first-principles calculations based on DFT and lattice dynamics. Harmonic phonon computations were performed to calculate group velocities and phonon dispersion relations using interatomic force constants obtained from DFT. Furthermore, the phonon BTE was solved to determine thermal conductivity, considering three-phonon scattering processes to account for anharmonic effects. Phonon frequencies, group velocities, and the number of triplets of three-phonon interactions are reported for each q-point. The bulk thermal conductivity and nonlocal length are displayed as a function of temperature, illustrating the inherent phonon-transport behavior anticipated using ab initio techniques.

```
q-point: ( 0.00  0.00  0.00)
Boundary mean free path (millimetre): 1000.000
Number of triplets: 28
Frequency     group velocity (x, y, z)     |gv|
  -0.000   (   0.000    0.000    0.000)    0.000
   0.000   (   0.000    0.000    0.000)    0.000
   0.000   (   0.000    0.000    0.000)    0.000
   4.029   (   0.000    0.000    0.000)    0.000
   4.029   (   0.000   -0.000    0.000)    0.000
   9.839   (   0.000    0.000    0.000)    0.000
  15.910   (   0.000    0.000    0.000)    0.000
  16.613   (   0.000   -0.000    0.000)    0.000
  16.613   (  -0.000    0.000   -0.000)    0.000
  16.757   (  -0.000   -0.000    0.000)    0.000
  16.757   (   0.000   -0.000   -0.000)    0.000
  20.193   (   0.000    0.000    0.000)    0.000
======================= Grid point 1 (2/28) =======================
```

```
q-point: ( 0.17  0.00  0.00)
Boundary mean free path (millimetre): 1000.000
Number of triplets: 48
Frequency     group velocity (x, y, z)     |gv|
   2.101   (  27.628   15.951    0.000)   31.902
   2.141   (  33.156   19.142    0.000)   38.285
   4.169   (  57.415   33.148    0.000)   66.297
   4.478   (  11.506    6.643    0.000)   13.286
   5.409   (  33.559   19.376    0.000)   38.751
   9.358   ( -12.120   -6.998    0.000)   13.995
  16.125   (   6.404    3.697    0.000)    7.395
  16.858   (   4.406    2.544    0.000)    5.088
  17.101   (   8.667    5.004    0.000)   10.008
  17.552   (  20.378   11.765    0.000)   23.530
  18.464   (  42.498   24.536    0.000)   49.072
  20.004   (  -5.296   -3.058    0.000)    6.116
====================== Grid point 2 (3/28) ======================
q-point: ( 0.33  0.00  0.00)
Boundary mean free path (millimetre): 1000.000
Number of triplets: 52
Frequency     group velocity (x, y, z)     |gv|
   3.544   (  13.255    7.653    0.000)   15.306
   4.209   (  25.480   14.711    0.000)   29.422
   5.311   (  11.067    6.390    0.000)   12.779
   7.109   (   4.506    2.601    0.000)    5.203
   7.633   (  39.082   22.564    0.000)   45.128
   8.958   (   9.568    5.524    0.000)   11.048
  16.756   (  11.175    6.452    0.000)   12.904
  16.914   (  -2.947   -1.701    0.000)    3.403
  17.672   (   6.560    3.787    0.000)    7.575
  18.895   (   9.541    5.508    0.000)   11.017
```

```
  19.692   (   3.723    2.149    0.000)    4.298
  20.831   (  19.725   11.388    0.000)   22.776
======================= Grid point 3 (4/28) =======================
q-point: (-0.50  0.00  0.00)
Boundary mean free path (millimetre): 1000.000
Number of triplets: 32
Frequency     group velocity (x, y, z)     |gv|
   3.955   (  -0.000   -0.000    0.000)    0.000
   5.272   (   0.000    0.000    0.000)    0.000
   5.747   (   0.000    0.000    0.000)    0.000
   6.763   (   0.000    0.000    0.000)    0.000
   9.204   (   0.000    0.000    0.000)    0.000
   9.530   (  -0.000   -0.000    0.000)    0.000
  16.730   (  -0.000   -0.000    0.000)    0.000
  17.301   (  -0.000   -0.000    0.000)    0.000
  17.902   (  -0.000   -0.000    0.000)    0.000
  18.767   (   0.000    0.000    0.000)    0.000
  20.428   (   0.000    0.000    0.000)    0.000
  21.200   (  -0.000   -0.000    0.000)    0.000
======================= Grid point 8 (5/28) =======================
q-point: ( 0.17  0.17  0.00)
Boundary mean free path (millimetre): 1000.000
Number of triplets: 48
Frequency     group velocity (x, y, z)     |gv|
   3.706   (  16.623   28.793    0.000)   33.247
   3.828   (  17.017   29.474    0.000)   34.033
   5.352   (  10.613   18.382    0.000)   21.226
   6.486   (  22.699   39.316    0.000)   45.398
   6.679   (   9.515   16.480    0.000)   19.029
   8.816   (  -3.366   -5.830    0.000)    6.732
  16.558   (   6.173   10.692    0.000)   12.346
```

```
  17.417   (   5.370    9.302    0.000)   10.741
  17.615   (   6.957   12.049    0.000)   13.913
  18.430   (   8.341   14.446    0.000)   16.681
  19.683   (  -3.792   -6.569    0.000)    7.585
  20.124   (  13.378   23.171    0.000)   26.756
======================= Grid point 9 (6/28) =======================
q-point: ( 0.33  0.17  0.00)
Boundary mean free path (millimetre): 1000.000
Number of triplets: 72
Frequency     group velocity (x, y, z)     |gv|
   4.931   (  -7.749   31.093    0.000)   32.044
   5.199   (  10.444   17.108    0.000)   20.044
   6.170   (  -4.115   18.798    0.000)   19.243
   6.803   (  -1.923   -7.138    0.000)    7.393
   8.438   (  23.239    3.257    0.000)   23.466
   9.035   (  10.731   -6.600    0.000)   12.599
  17.265   (   5.371   10.813    0.000)   12.073
  17.597   ( -11.857   20.947    0.000)   24.070
  18.182   (  -2.365   10.816    0.000)   11.071
  18.744   (  -1.322   -6.236    0.000)    6.375
  19.758   (  14.777   -4.909    0.000)   15.571
  20.753   (   6.587  -13.143    0.000)   14.702
======================= Grid point 15 (7/28) =======================
q-point: ( 0.33  0.33  0.00)
Boundary mean free path (millimetre): 1000.000
Number of triplets: 28
Frequency     group velocity (x, y, z)     |gv|
   6.048   (  -6.147  -10.646    0.000)   12.293
   6.048   (   6.147   10.646    0.000)   12.293
   6.231   (   0.000    0.000    0.000)    0.000
   7.311   (  -0.000   -0.000    0.000)    0.000
```

```
   8.385   (  -2.881   -4.991    0.000)    5.763
   8.385   (   2.881    4.991    0.000)    5.763
  17.949   (  -5.721   -9.908    0.000)   11.441
  17.949   (   5.721    9.908    0.000)   11.441
  18.889   (   0.000    0.000    0.000)    0.000
  19.017   (  -0.530   -0.918    0.000)    1.059
  19.017   (   0.530    0.918    0.000)    1.059
  19.962   (  -0.000   -0.000    0.000)    0.000
======================= Grid point 43 (8/28) =======================
q-point: ( 0.00  0.00  0.17)
Boundary mean free path (millimetre): 1000.000
Number of triplets: 21
Frequency     group velocity (x, y, z)     |gv|
   1.188   (   0.000    0.000   36.198)   36.198
   1.188   (   0.000   -0.000   36.198)   36.198
   2.788   (   0.000   -0.000   82.638)   82.638
   3.934   (  -0.000   -0.000   -6.139)    6.139
   3.934   (  -0.000    0.000   -6.139)    6.139
   9.302   (   0.000    0.000  -30.202)   30.202
  16.616   (   0.000    0.000    0.173)    0.173
  16.616   (   0.000    0.000    0.173)    0.173
  16.740   (  -0.000   -0.000   -1.027)    1.027
  16.740   (   0.000   -0.000   -1.027)    1.027
  17.000   (  -0.000    0.000   62.441)   62.441
  20.688   (  -0.000    0.000   25.615)   25.615
======================= Grid point 44 (9/28) =======================
q-point: ( 0.17  0.00  0.17)
Boundary mean free path (millimetre): 1000.000
Number of triplets: 63
Frequency     group velocity (x, y, z)     |gv|
   2.427   (  24.186   13.964   18.506)   33.503
```

```
   2.919   (  17.928   10.351   35.562)   41.149
   4.416   (  11.948    6.898   -4.158)   14.409
   4.587   (  51.347   29.645   26.736)   65.039
   5.313   (  32.093   18.529   -5.768)   37.503
   8.983   (  -7.101   -4.100  -21.559)   23.066
  16.787   (   0.454    0.262   34.543)   34.547
  16.858   (   4.706    2.717    0.110)    5.435
  17.073   (   8.325    4.807   -1.727)    9.767
  17.502   (  18.905   10.915   -2.335)   21.954
  18.502   (  39.032   22.535    5.675)   45.426
  20.343   (  -8.670   -5.005   17.413)   20.086
======================== Grid point 45 (10/28) ========================
q-point: ( 0.33  0.00  0.17)
Boundary mean free path (millimetre): 1000.000
Number of triplets: 63
Frequency     group velocity (x, y, z)     |gv|
   3.743   (  12.309    7.106   11.767)   18.452
   4.217   (  18.561   10.716    1.685)   21.499
   5.247   (  10.670    6.160   -4.098)   12.984
   6.637   (  -0.021   -0.012  -25.664)   25.664
   7.906   (  39.027   22.532   15.900)   47.787
   9.129   (  14.982    8.650    7.145)   18.717
  16.968   (   5.279    3.048   12.186)   13.626
  16.970   (  -1.747   -1.009    3.476)    4.019
  17.627   (   6.471    3.736   -2.778)    7.972
  18.602   (   6.418    3.705  -14.023)   15.861
  19.942   (   2.800    1.617   11.147)   11.606
  20.721   (  19.115   11.036   -6.167)   22.917
======================== Grid point 46 (11/28) ========================
q-point: (-0.50  0.00  0.17)
Boundary mean free path (millimetre): 1000.000
```

```
Number of triplets: 39
Frequency     group velocity (x, y, z)     |gv|
   4.126   (  -0.000   -0.000   10.209)   10.209
   5.047   (  -0.000   -0.000  -12.219)   12.219
   5.660   (  -0.000   -0.000   -5.479)    5.479
   6.274   (   0.000    0.000  -26.639)   26.639
   9.442   (   0.000    0.000   13.224)   13.224
   9.782   (  -0.000   -0.000   12.365)   12.365
  16.842   (  -0.000   -0.000    6.770)    6.770
  17.272   (  -0.000   -0.000   -1.243)    1.243
  17.856   (  -0.000   -0.000   -2.987)    2.987
  18.541   (  -0.000   -0.000  -13.319)   13.319
  20.444   (   0.000    0.000    1.218)    1.218
  21.130   (  -0.000   -0.000   -4.381)    4.381
====================== Grid point 51 (12/28) ======================
q-point: ( 0.17  0.17  0.17)
Boundary mean free path (millimetre): 1000.000
Number of triplets: 63
Frequency     group velocity (x, y, z)     |gv|
   3.828   (  11.093   19.214    8.061)   23.606
   4.011   (  16.036   27.775   10.803)   33.842
   5.309   (  10.766   18.647   -2.742)   21.706
   6.348   (   5.757    9.972  -19.140)   22.337
   6.826   (  22.307   38.637   19.583)   48.722
   8.808   (   1.773    3.070   -1.420)    3.819
  16.869   (   2.161    3.743   17.191)   17.726
  17.415   (   5.528    9.576   -0.120)   11.058
  17.595   (   7.097   12.293   -0.934)   14.225
  18.247   (   6.049   10.478   -8.990)   15.073
  19.914   (  -3.892   -6.742   11.328)   13.745
  20.056   (  12.715   22.024   -3.339)   25.649
```

```
====================== Grid point 52 (13/28) ======================
q-point: ( 0.33  0.17  0.17)
Boundary mean free path (millimetre): 1000.000
Number of triplets: 108
Frequency     group velocity (x, y, z)     |gv|
   4.824   (   2.832   16.952  -10.337)   20.057
   5.180   (  -0.623   25.410    4.420)   25.799
   6.004   (  -6.745    7.718  -14.069)   17.407
   6.434   (   0.003    5.477  -14.963)   15.934
   8.730   (  21.967    4.048   16.049)   27.505
   9.307   (  10.891   -5.277   12.931)   17.711
  17.193   (   1.503    6.914   -3.321)    7.816
  17.694   (  -7.408   18.715    4.402)   20.604
  18.055   (  -4.540    5.995   -7.790)   10.827
  18.587   (   1.617    2.491   -6.878)    7.491
  19.894   (  10.238   -6.481    6.737)   13.864
  20.684   (   7.122  -11.780   -4.112)   14.367
====================== Grid point 58 (14/28) ======================
q-point: ( 0.33  0.33  0.17)
Boundary mean free path (millimetre): 1000.000
Number of triplets: 30
Frequency     group velocity (x, y, z)     |gv|
   5.582   (  -5.179   -8.970  -24.386)   26.495
   5.582   (   5.179    8.970  -24.386)   26.495
   6.334   (   0.000    0.000    6.155)    6.155
   7.262   (   0.000    0.000   -3.130)    3.130
   8.747   (  -2.757   -4.775   18.045)   18.869
   8.747   (   2.757    4.775   18.045)   18.869
  17.675   (  -4.370   -7.568  -14.120)   16.606
  17.675   (   4.370    7.568  -14.120)   16.606
  18.980   (   0.000    0.000    5.593)    5.593
```

```
  19.150   (  -1.071   -1.855    6.036)    6.405
  19.150   (   1.071    1.855    6.036)    6.405
  19.910   (  -0.000   -0.000   -3.305)    3.305
======================= Grid point 86 (15/28) =======================
q-point: ( 0.00  0.00  0.33)
Boundary mean free path (millimetre): 1000.000
Number of triplets: 28
Frequency     group velocity (x, y, z)     |gv|
   2.244   (   0.000   -0.000   30.211)   30.211
   2.244   (   0.000    0.000   30.211)   30.211
   3.628   (  -0.000   -0.000  -13.471)   13.471
   3.628   (   0.000    0.000  -13.471)   13.471
   5.112   (   0.000    0.000   63.995)   63.995
   8.180   (  -0.000    0.000  -38.853)   38.853
  16.627   (   0.000    0.000    0.601)    0.601
  16.627   (  -0.000    0.000    0.601)    0.601
  16.699   (   0.000    0.000   -1.460)    1.460
  16.699   (   0.000   -0.000   -1.460)    1.460
  19.243   (   0.000    0.000   69.978)   69.978
  21.336   (   0.000    0.000    8.672)    8.672
======================= Grid point 87 (16/28) =======================
q-point: ( 0.17  0.00  0.33)
Boundary mean free path (millimetre): 1000.000
Number of triplets: 66
Frequency     group velocity (x, y, z)     |gv|
   3.107   (  19.159   11.062   22.450)   31.519
   3.868   (  18.165   10.487   24.146)   31.984
   4.194   (  13.297    7.677  -10.285)   18.480
   4.980   (  26.871   15.514  -11.562)   33.112
   5.809   (  30.901   17.841   42.245)   55.297
   8.147   (   3.087    1.782  -30.039)   30.249
```

```
  16.873   (   5.465    3.155    0.968)    6.385
  17.001   (   7.478    4.318   -2.589)    9.015
  17.428   (  15.803    9.124    0.991)   18.274
  17.523   (  12.387    7.152    3.765)   14.790
  19.250   (   9.287    5.362   41.006)   42.385
  20.765   ( -13.462   -7.772    4.396)   16.154
======================= Grid point 88 (17/28) =======================
q-point: ( 0.33  0.00  0.33)
Boundary mean free path (millimetre): 1000.000
Number of triplets: 68
Frequency     group velocity (x, y, z)     |gv|
   4.204   (  10.609    6.125   16.013)   20.161
   4.400   (   5.060    2.921   10.804)   12.283
   5.044   (   9.906    5.719   -8.891)   14.487
   5.735   (  -4.248   -2.453  -28.911)   29.325
   8.497   (  35.815   20.678   19.325)   45.648
   9.238   (  23.223   13.408   -1.442)   26.854
  17.121   (   1.112    0.642    5.801)    5.941
  17.407   (  -4.554   -2.629   13.901)   14.863
  17.501   (   5.839    3.371   -5.098)    8.453
  18.166   (   0.210    0.121  -12.737)   12.739
  20.236   (   2.355    1.360    6.761)    7.287
  20.520   (  15.302    8.834   -5.452)   18.491
======================= Grid point 89 (18/28) =======================
q-point: (-0.50  0.00  0.33)
Boundary mean free path (millimetre): 1000.000
Number of triplets: 42
Frequency     group velocity (x, y, z)     |gv|
   4.539   (  -0.000   -0.000   14.922)   14.922
   4.688   (   0.000    0.000   -7.432)    7.432
   5.366   (  -0.000   -0.000  -27.308)   27.308
```

```
   5.406   (  -0.000   -0.000  -10.507)   10.507
   9.886   (  -0.000   -0.000   12.771)   12.771
  10.110   (  -0.000   -0.000    6.715)    6.715
  17.123   (  -0.000   -0.000   10.304)   10.304
  17.287   (   0.000    0.000    3.325)    3.325
  17.707   (  -0.000   -0.000   -6.527)    6.527
  18.024   (  -0.000   -0.000  -17.654)   17.654
  20.523   (   0.000    0.000    4.057)    4.057
  20.938   (  -0.000   -0.000   -7.375)    7.375
======================= Grid point 94 (19/28) =======================
q-point: ( 0.17  0.17  0.33)
Boundary mean free path (millimetre): 1000.000
Number of triplets: 66
Frequency     group velocity (x, y, z)     |gv|
   4.221   (   2.465    4.269   16.509)   17.230
   4.431   (  13.888   24.054   14.461)   31.315
   5.165   (  11.267   19.515   -6.684)   23.504
   5.620   (   0.836    1.448  -24.918)   24.974
   7.559   (  19.995   34.632   24.393)   46.842
   8.664   (   9.728   16.849   -8.458)   21.215
  17.349   (  -0.975   -1.690    7.278)    7.535
  17.409   (   5.402    9.357   -0.252)   10.807
  17.636   (   4.742    8.213    6.080)   11.265
  17.990   (   2.934    5.083   -6.335)    8.636
  20.016   (   8.750   15.155    2.271)   17.646
  20.199   (  -3.950   -6.842    4.676)    9.180
======================= Grid point 95 (20/28) =======================
q-point: ( 0.33  0.17  0.33)
Boundary mean free path (millimetre): 1000.000
Number of triplets: 108
Frequency     group velocity (x, y, z)     |gv|
```

```
   4.498   (   3.142    4.262   -6.183)    8.140
   5.180   (  -2.833   -2.005  -19.995)   20.294
   5.541   (  -7.170   22.457    4.878)   24.073
   6.122   (  -2.275   22.228   -8.020)   23.740
   9.270   (  19.128    3.923   15.883)   25.170
   9.633   (  12.728   -1.949    5.922)   14.173
  17.125   (  -1.794   -0.645   -0.002)    1.907
  17.577   (  -0.278   -3.749  -12.060)   12.633
  17.999   (  -8.521   18.968    6.063)   21.660
  18.402   (   0.101   13.856   -5.367)   14.859
  20.108   (   6.450   -7.822    6.559)   12.075
  20.515   (   7.372   -9.520   -6.193)   13.540
======================= Grid point 101 (21/28) =======================
q-point: ( 0.33  0.33  0.33)
Boundary mean free path (millimetre): 1000.000
Number of triplets: 34
Frequency     group velocity (x, y, z)     |gv|
   4.810   (  -3.087   -5.346  -20.855)   21.750
   4.810   (   3.087    5.346  -20.855)   21.750
   6.586   (  -0.000   -0.000    9.165)    9.165
   7.114   (  -0.000   -0.000   -6.238)    6.238
   9.272   (  -1.682   -2.913   12.967)   13.396
   9.272   (   1.682    2.913   12.967)   13.396
  17.242   (  -2.295   -3.974  -11.239)   12.139
  17.242   (   2.295    3.974  -11.239)   12.139
  19.217   (   0.000    0.000    8.862)    8.862
  19.302   (  -0.883   -1.529    3.191)    3.647
  19.302   (   0.883    1.529    3.191)    3.647
  19.754   (  -0.000   -0.000   -6.564)    6.564
======================= Grid point 129 (22/28) =======================
q-point: ( 0.00  0.00 -0.50)
```

```
Boundary mean free path (millimetre): 1000.000
Number of triplets: 14
Frequency     group velocity (x, y, z)     |gv|
   3.071   (   0.000    0.000  -21.972)   21.972
   3.071   (  -0.000    0.000  -21.972)   21.972
   3.071   (  -0.000    0.000   21.972)   21.972
   3.071   (   0.000    0.000   21.972)   21.972
   6.846   (  -0.000    0.000  -47.069)   47.069
   6.846   (   0.000    0.000   47.069)   47.069
  16.655   (  -0.000    0.000   -1.185)    1.185
  16.655   (   0.000    0.000   -1.185)    1.185
  16.655   (   0.000   -0.000    1.185)    1.185
  16.655   (   0.000    0.000    1.185)    1.185
  20.957   (  -0.000    0.000  -34.389)   34.389
  20.957   (   0.000    0.000   34.389)   34.389
====================== Grid point 131 (23/28) ======================
q-point: ( 0.17  0.00 -0.50)
Boundary mean free path (millimetre): 1000.000
Number of triplets: 42
Frequency     group velocity (x, y, z)     |gv|
   3.753   (  15.619    9.018  -17.624)   25.217
   3.753   (  15.619    9.018   17.624)   25.217
   4.514   (  22.613   13.056  -17.480)   31.422
   4.514   (  22.613   13.056   17.480)   31.422
   7.094   (  14.490    8.366  -37.225)   40.813
   7.094   (  14.490    8.366   37.225)   40.813
  16.923   (   6.449    3.723   -2.161)    7.754
  16.923   (   6.449    3.723    2.161)    7.754
  17.482   (  16.666    9.622   -2.929)   19.466
  17.482   (  16.666    9.622    2.929)   19.466
  20.428   ( -10.555   -6.094  -26.489)   29.158
```

```
  20.428   ( -10.555   -6.094   26.489)   29.158
======================= Grid point 133 (24/28) =======================
q-point: ( 0.33  0.00 -0.50)
Boundary mean free path (millimetre): 1000.000
Number of triplets: 42
Frequency     group velocity (x, y, z)     |gv|
   4.685   (   9.684    5.591  -13.737)   17.713
   4.685   (   9.684    5.591   13.737)   17.713
   4.918   (  -3.581   -2.068  -21.815)   22.203
   4.918   (  -3.581   -2.068   21.815)   22.203
   9.016   (  30.238   17.458  -12.406)   37.054
   9.016   (  30.238   17.458   12.406)   37.054
  17.317   (   4.033    2.329   -6.312)    7.844
  17.317   (   4.033    2.329    6.312)    7.844
  17.798   (  -5.789   -3.342  -11.239)   13.076
  17.798   (  -5.789   -3.342   11.239)   13.076
  20.387   (   7.560    4.365   -3.654)    9.463
  20.387   (   7.560    4.365    3.654)    9.463
======================= Grid point 135 (25/28) =======================
q-point: (-0.50  0.00 -0.50)
Boundary mean free path (millimetre): 1000.000
Number of triplets: 26
Frequency     group velocity (x, y, z)     |gv|
   4.729   (   0.000    0.000  -11.186)   11.186
   4.729   (  -0.000   -0.000   11.186)   11.186
   5.010   (  -0.000   -0.000  -14.229)   14.229
   5.010   (   0.000    0.000   14.229)   14.229
  10.159   (  -0.000   -0.000   -3.790)    3.790
  10.159   (   0.000    0.000    3.790)    3.790
  17.448   (  -0.000   -0.000   -9.697)    9.697
  17.448   (  -0.000   -0.000    9.697)    9.697
```

```
  17.531   (   0.000    0.000  -12.308)   12.308
  17.531   (  -0.000   -0.000   12.308)   12.308
  20.701   (   0.000    0.000   -7.011)    7.011
  20.701   (  -0.000   -0.000    7.011)    7.011
====================== Grid point 145 (26/28) ======================
q-point: ( 0.17  0.17 -0.50)
Boundary mean free path (millimetre): 1000.000
Number of triplets: 42
Frequency     group velocity (x, y, z)     |gv|
   4.791   (   3.584    6.208   -6.945)    9.981
   4.791   (   3.584    6.208    6.945)    9.981
   4.926   (   7.643   13.239   -3.765)   15.744
   4.926   (   7.643   13.239    3.765)   15.744
   8.247   (  15.716   27.222  -18.017)   36.230
   8.247   (  15.716   27.222   18.017)   36.230
  17.404   (   3.973    6.881   -0.027)    7.945
  17.404   (   3.973    6.881    0.027)    7.945
  17.839   (   0.904    1.566   -4.542)    4.889
  17.839   (   0.904    1.566    4.542)    4.889
  20.173   (   0.555    0.961   -5.249)    5.365
  20.173   (   0.555    0.961    5.249)    5.365
====================== Grid point 147 (27/28) ======================
q-point: ( 0.33  0.17 -0.50)
Boundary mean free path (millimetre): 1000.000
Number of triplets: 72
Frequency     group velocity (x, y, z)     |gv|
   4.582   (  -1.455   -4.167  -12.164)   12.940
   4.582   (  -1.455   -4.167   12.164)   12.940
   5.840   (  -4.652   25.301   -9.973)   27.591
   5.840   (  -4.652   25.301    9.973)   27.591
   9.632   (  15.752    1.639   -6.121)   16.978
```

```
   9.632   (  15.752    1.639    6.121)   16.978
  17.240   (  -1.883   -5.522   -7.599)    9.580
  17.240   (  -1.883   -5.522    7.599)    9.580
  18.215   (  -4.119   18.299   -6.650)   19.901
  18.215   (  -4.119   18.299    6.650)   19.901
  20.312   (   6.402   -8.395   -6.484)   12.390
  20.312   (   6.402   -8.395    6.484)   12.390
======================= Grid point 159 (28/28) =======================
q-point: ( 0.33  0.33 -0.50)
Boundary mean free path (millimetre): 1000.000
Number of triplets: 20
Frequency     group velocity (x, y, z)     |gv|
   4.452   (  -0.000   -0.000    0.000)    0.000
   4.452   (   0.000    0.000    0.000)    0.000
   6.875   (   0.000    0.000   -8.706)    8.706
   6.875   (  -0.000   -0.000    8.706)    8.706
   9.485   (  -0.000   -0.000    0.000)    0.000
   9.485   (   0.000    0.000   -0.000)    0.000
  17.054   (  -0.000   -0.000   -0.000)    0.000
  17.054   (   0.000    0.000    0.000)    0.000
  19.351   (   0.000    0.000   -0.000)    0.000
  19.351   (   0.000    0.000    0.000)    0.000
  19.505   (  -0.000   -0.000   -8.911)    8.911
  19.505   (  -0.000   -0.000    8.911)    8.911
=================== End of collection of collisions ===================
-------- Thermal conductivity (W/m-k) with tetrahedron method ---------
#  T(K)        xx         yy         zz
  300.0     255.108    255.108    310.849
  310.0     246.514    246.514    299.872
  320.0     238.496    238.496    289.679
  330.0     230.997    230.997    280.185
```

340.0	223.968	223.968	271.319
350.0	217.365	217.365	263.020
360.0	211.150	211.150	255.233
370.0	205.288	205.288	247.911
380.0	199.750	199.750	241.013
390.0	194.509	194.509	234.501
400.0	189.541	189.541	228.343
410.0	184.826	184.826	222.510
420.0	180.343	180.343	216.977
430.0	176.077	176.077	211.720
440.0	172.010	172.010	206.719
450.0	168.130	168.130	201.954
460.0	164.424	164.424	197.410
470.0	160.879	160.879	193.070
480.0	157.487	157.487	188.921
490.0	154.236	154.236	184.951
500.0	151.117	151.117	181.148
510.0	148.124	148.124	177.500
520.0	145.249	145.249	174.000
530.0	142.483	142.483	170.637
540.0	139.822	139.822	167.404
550.0	137.260	137.260	164.293
560.0	134.790	134.790	161.297
570.0	132.409	132.409	158.410
580.0	130.110	130.110	155.627
590.0	127.891	127.891	152.940
600.0	125.747	125.747	150.346
610.0	123.673	123.673	147.840
620.0	121.668	121.668	145.417
630.0	119.727	119.727	143.072
640.0	117.847	117.847	140.803

650.0	116.025	116.025	138.606
660.0	114.259	114.259	136.477
670.0	112.547	112.547	134.413
680.0	110.885	110.885	132.411
690.0	109.272	109.272	130.468
700.0	107.705	107.705	128.582
710.0	106.183	106.183	126.750
720.0	104.703	104.703	124.970
730.0	103.264	103.264	123.239
740.0	101.864	101.864	121.557
750.0	100.502	100.502	119.920
760.0	99.176	99.176	118.326
770.0	97.884	97.884	116.775
780.0	96.626	96.626	115.264
790.0	95.400	95.400	113.792
800.0	94.205	94.205	112.358

T[k]	NL-param[nm]
300	557.8965135
310	530.2605531
320	505.2335576
330	482.4753825
340	461.7002409
350	442.6666561
360	425.169492
370	409.0335902
380	394.1086588
390	380.2651431
400	367.3908688
410	355.3883008
420	344.1722906

```
430 333.6682178
440 323.8104483
450 314.5410502
460 305.8087181
470 297.5678702
480 289.7778855
490 282.4024579
500 275.4090469
510 268.7684084
520 262.4541932
530 256.4426017
540 250.7120861
550 245.2430932
560 240.0178406
570 235.0201227
580 230.2351407
590 225.6493546
600 221.2503523
610 217.0267359
620 212.96802
630 209.0645431
640 205.3073878
650 201.6883114
660 198.199683
670 194.8344276
680 191.5859772
690 188.4482253
700 185.4154876
710 182.4824661
720 179.6442165
730 176.8961192
```

740 174.2338533

750 171.6533724

760 169.1508833

770 166.7228263

780 164.3658575

790 162.0768329

800 159.8527931

APPENDIX C: COPYRIGHT PERMISSIONS

AIP PUBLISHING LICENSE
TERMS AND CONDITIONS

Jul 10, 2025

This Agreement between Amir Abdolhosseinzadeh/ Bogazici University ("You") and AIP Publishing ("AIP Publishing") consists of your license details and the terms and conditions provided by AIP Publishing and Copyright Clearance Center.

License Number	6065431094328
License date	Jul 10, 2025
Licensed Content Publisher	AIP Publishing
Licensed Content Publication	Journal of Applied Physics
Licensed Content Title	Nanoscale electro-thermal interactions in AlGaN/GaN high electron mobility transistors
Licensed Content Author	Chatterjee, Bikramjit; Dundar, Canberk
Licensed Content Date	Jan 23, 2020
Licensed Content Volume	127
Licensed Content Issue	4
Type of Use	Thesis/Dissertation
Requestor type	Student
Format	Print and electronic

Figure C.1. First page of copyright permission for Figure 1.1 and 1.13.

Portion	Figure/Table
Number of figures/tables	2
Will you be translating?	No
Title of new work	Comprehensive Study of Simplified Models for Thermal Size Effects Induced by Localized Heating in Crystalline Solids
Institution name	Bogazici university
Expected presentation date	Aug 2025
Portions	FIG. 1. FIG. 6.
The Requesting Person / Organization to Appear on the License	Amir Abdolhosseinzadeh/ Bogazici University
Requestor Location	Boğaziçi Üniversitesi Güney Kampüsü Makina Mühendisliği Bölümü Istanbul, Besiktas 34342 Turkey
Billing Type	Invoice
Billing Address	Bogazici university Boğaziçi Üniversitesi Güney Kampüsü Makina Mühendisliği Bölümü Istanbul, Turkey 34342
Total	0.00 USD
Terms and Conditions	

Figure C.2. Second page of copyright permission for Figure 1.1 and 1.13.

AIP PUBLISHING LICENSE
TERMS AND CONDITIONS

Jul 13, 2025

This Agreement between Amir Abdolhosseinzadeh ("You") and AIP Publishing ("AIP Publishing") consists of your license details and the terms and conditions provided by AIP Publishing and Copyright Clearance Center.

License Number	6066910392520
License date	Jul 13, 2025
Licensed Content Publisher	AIP Publishing
Licensed Content Publication	Applied Physics Letters
Licensed Content Title	Phonon-boundary scattering in thin silicon layers
Licensed Content Author	Asheghi, M.; Leung, Y. K.
Licensed Content Date	Sep 29, 1997
Licensed Content Volume	71
Licensed Content Issue	13
Type of Use	Thesis/Dissertation
Requestor type	Student
Format	Print and electronic
Portion	Figure/Table

Figure C.3. First page of copyright permission for Figure 1.2 (a).

Number of figures/tables	1
Will you be translating?	No
Title of new work	Comprehensive Study of Simplified Models for Thermal Size Effects Induced by Localized Heating in Crystalline Solids
Institution name	Bogazici university
Expected presentation date	Aug 2025
Portions	FIG. 2
The Requesting Person / Organization to Appear on the License	Amir Abdolhosseinzadeh
Requestor Location	Mr. Amir Abdolhosseinzadeh Boğaziçi Üniversitesi Güney Kampüsü Makina Mühendisliği Bölümü Istanbul, Besiktas 34342 Turkey
Billing Type	Invoice
Billing Address	Bogazici university Boğaziçi Üniversitesi Güney Kampüsü Makina Mühendisliği Bölümü Istanbul, Turkey 34342
Total	0.00 USD

Terms and Conditions

AIP Publishing -- Terms and Conditions: Permissions Uses

Figure C.4. Second page of copyright permission for Figure 1.2 (a).

SPRINGER NATURE LICENSE
TERMS AND CONDITIONS

Jul 13, 2025

This Agreement between Amir Abdolhosseinzadeh ("You") and Springer Nature ("Springer Nature") consists of your license details and the terms and conditions provided by Springer Nature and Copyright Clearance Center.

License Number	6066910760076
License date	Jul 13, 2025
Licensed Content Publisher	Springer Nature
Licensed Content Publication	Journal of Electronic Materials
Licensed Content Title	Improving Thermal Effects and Reduction of Self-heating Phenomenon in AlGaN/GaN/Si Based HEMT
Licensed Content Author	Mojtaba Hosseinzadeh Sani et al
Licensed Content Date	Feb 1, 2021
Type of Use	Thesis/Dissertation
Requestor type	academic/university or research institute
Format	print and electronic
Portion	figures/tables/illustrations
Number of figures/tables/illustrations	1

Figure C.5. First page of copyright permission for Figure 1.2 (b).

Will you be translating?	no
Circulation/distribution	1 - 29
Author of this Springer Nature content	no
Title of new work	Comprehensive Study of Simplified Models for Thermal Size Effects Induced by Localized Heating in Crystalline Solids
Institution name	Bogazici university
Expected presentation date	Aug 2025
Portions	Fig. 5
The Requesting Person / Organization to Appear on the License	Amir Abdolhosseinzadeh
Requestor Location	Mr. Amir Abdolhosseinzadeh Boğaziçi Üniversitesi Güney Kampüsü Makina Mühendisliği Bölümü Istanbul, Besiktas 34342 Turkey
Billing Type	Invoice
Billing Address	Bogazici university Boğaziçi Üniversitesi Güney Kampüsü Makina Mühendisliği Bölümü Istanbul, Turkey 34342
Total	0.00 USD
Terms and Conditions	

Figure C.6. Second page of copyright permission for Figure 1.2 (b).

JOHN WILEY AND SONS LICENSE
TERMS AND CONDITIONS

Jul 13, 2025

This Agreement between Amir Abdolhosseinzadeh ("You") and John Wiley and Sons ("John Wiley and Sons") consists of your license details and the terms and conditions provided by John Wiley and Sons and Copyright Clearance Center.

License Number	6066990880399
License date	Jul 13, 2025
Licensed Content Publisher	John Wiley and Sons
Licensed Content Publication	Wiley Books
Licensed Content Title	Kittel's Introduction to Solid State Physics, 9th Edition, Global Edition
Licensed Content Author	Charles Kittel
Licensed Content Date	Jun 1, 2018
Licensed Content Pages	1
Type of use	Dissertation/Thesis
Requestor type	University/Academic
Format	Print and electronic
Portion	Figure/table

Figure C.7. First page of copyright permission for Figure 1.4.

Number of figures/tables	1
Will you be translating?	No
Title of new work	Comprehensive Study of Simplified Models for Thermal Size Effects Induced by Localized Heating in Crystalline Solids
Institution name	Bogazici university
Expected presentation date	Aug 2025
Portions	Figure 8a
The Requesting Person / Organization to Appear on the License	Amir Abdolhosseinzadeh
Requestor Location	Mr. Amir Abdolhosseinzadeh Boğaziçi Üniversitesi Güney Kampüsü Makina Mühendisliği Bölümü Istanbul, Besiktas 34342 Turkey
Publisher Tax ID	EU826007151
Total	0.00 USD

Terms and Conditions

TERMS AND CONDITIONS

This copyrighted material is owned by or exclusively licensed to John Wiley & Sons, Inc. or one of its group companies (each a"Wiley Company") or handled on behalf of a society with which a Wiley Company has exclusive publishing rights in relation to a particular work (collectively "WILEY"). By clicking "accept" in connection with completing this licensing transaction, you agree that the following terms and conditions apply to this transaction (along with the billing and payment terms and conditions established by the Copyright Clearance Center Inc., ("CCC's Billing and Payment terms and conditions"), at

Figure C.8. Second page of copyright permission for Figure 1.4.

SPRINGER NATURE LICENSE
TERMS AND CONDITIONS

Jul 13, 2025

This Agreement between Amir Abdolhosseinzadeh ("You") and Springer Nature ("Springer Nature") consists of your license details and the terms and conditions provided by Springer Nature and Copyright Clearance Center.

License Number	6066991079532
License date	Jul 13, 2025
Licensed Content Publisher	Springer Nature
Licensed Content Publication	International Journal of Thermophysics
Licensed Content Title	Lattice Dynamical Properties of Group-III Nitrides AN (A = B, Al, Ga and In) in Zinc-Blende Phase
Licensed Content Author	A. K. Kushwaha
Licensed Content Date	Jan 29, 2016
Type of Use	Thesis/Dissertation
Requestor type	academic/university or research institute
Format	print and electronic
Portion	figures/tables/illustrations
Number of figures/tables/illustrations	1

Figure C.9. First page of copyright permission for Figure 1.5.

Will you be translating?	no
Circulation/distribution	1 - 29
Author of this Springer Nature content	no
Title of new work	Comprehensive Study of Simplified Models for Thermal Size Effects Induced by Localized Heating in Crystalline Solids
Institution name	Bogazici university
Expected presentation date	Aug 2025
Portions	Fig. 2
The Requesting Person / Organization to Appear on the License	Amir Abdolhosseinzadeh
Requestor Location	Mr. Amir Abdolhosseinzadeh Boğaziçi Üniversitesi Güney Kampüsü Makina Mühendisliği Bölümü Istanbul, Besiktas 34342 Turkey
Billing Type	Invoice
Billing Address	Bogazici university Boğaziçi Üniversitesi Güney Kampüsü Makina Mühendisliği Bölümü Istanbul, Turkey 34342
Total	0.00 USD
Terms and Conditions	

Figure C.10. Second page of copyright permission for Figure 1.5.

JOHN WILEY AND SONS LICENSE
TERMS AND CONDITIONS

Jul 10, 2025

This Agreement between Amir Abdolhosseinzadeh ("You") and John Wiley and Sons ("John Wiley and Sons") consists of your license details and the terms and conditions provided by John Wiley and Sons and Copyright Clearance Center.

License Number	6065440241489
License date	Jul 10, 2025
Licensed Content Publisher	John Wiley and Sons
Licensed Content Publication	Advanced Functional Materials
Licensed Content Title	Advanced Materials for High-Temperature Thermal Transport
Licensed Content Author	Renkun Chen, Jian Luo, Qingyang Wang, et al
Licensed Content Date	Sep 15, 2019
Licensed Content Volume	30
Licensed Content Issue	8
Licensed Content Pages	23
Type of use	Dissertation/Thesis
Requestor type	University/Academic

Figure C.11. First page of copyright permission for Figure 1.6.

Format	Print and electronic
Portion	Figure/table
Number of figures/tables	1
Will you be translating?	No
Title of new work	Comprehensive Study of Simplified Models for Thermal Size Effects Induced by Localized Heating in Crystalline Solids
Institution name	Bogazici university
Expected presentation date	Aug 2025
Portions	Figure 1
The Requesting Person / Organization to Appear on the License	Amir Abdolhosseinzadeh
Requestor Location	Mr. Amir Abdolhosseinzadeh Boğaziçi Üniversitesi Güney Kampüsü Makina Mühendisliği Bölümü Istanbul, Besiktas 34342 Turkey
Publisher Tax ID	EU826007151
Total	0.00 USD

Terms and Conditions

TERMS AND CONDITIONS

This copyrighted material is owned by or exclusively licensed to John Wiley & Sons, Inc. or one of its group companies (each a"Wiley Company") or handled on behalf of a society

Figure C.12. Second page of copyright permission for Figure 1.6.

American Physical Society
Reuse and Permissions License

13-Jul-2025

This license agreement between the American Physical Society ("APS") and Amir Abdolhosseinzadeh ("You") consists of your license details and the terms and conditions provided by the American Physical Society and SciPris.

Licensed Content Information

License Number:	**RNP/25/JUL/093425**
License date:	13-Jul-2025
DOI:	10.1103/PhysRevB.102.195412
Title:	Quantum mechanical modeling of anharmonic phonon-phonon scattering in nanostructures
Author:	Yangyu Guo et al.
Publication:	Physical Review B
Publisher:	American Physical Society
Cost:	USD $ 0.00

Request Details

Does your reuse require significant modifications: No

Specify intended distribution locations:	Turkey
Reuse Category:	Reuse in a thesis/dissertation
Requestor Type:	Student
Items for Reuse:	Figures/Tables
Number of Figure/Tables:	1
Figure/Tables Details:	Fig. 9.
Format for Reuse:	Print and Electronic
Total number of print copies:	Up to 1000

Information about New Publication:

University/Publisher:	Bogazici university
Title of dissertation/thesis:	Comprehensive Study of Simplified Models for Thermal Size Effects Induced by Localized Heating in Crystalline Solids
Author(s):	Amir Abdolhosseinzadeh
Expected completion date:	Aug. 2025

License Requestor Information

Name:	Amir Abdolhosseinzadeh
Affiliation:	Individual
Email Id:	amir.abdolhosseinzadeh@std.bogazici.edu.tr
Country:	Turkey

Figure C.13. Copyright permission for Figure 1.7.

American Physical Society
Reuse and Permissions License

13-Jul-2025

This license agreement between the American Physical Society ("APS") and Amir Abdolhosseinzadeh ("You") consists of your license details and the terms and conditions provided by the American Physical Society and SciPris.

Licensed Content Information

License Number:	**RNP/25/JUL/093423**
License date:	13-Jul-2025
DOI:	10.1103/PhysRevB.93.140201
Title:	Size effects on the thermal conductivity of amorphous silicon thin films
Author:	Jeffrey L. Braun et al.
Publication:	Physical Review B
Publisher:	American Physical Society
Cost:	USD $ 0.00

Request Details

Does your reuse require significant modifications: No

Specify intended distribution locations:	Turkey
Reuse Category:	Reuse in a thesis/dissertation
Requestor Type:	Student
Items for Reuse:	Figures/Tables
Number of Figure/Tables:	1
Figure/Tables Details:	Fig. 3.
Format for Reuse:	Print and Electronic
Total number of print copies:	Up to 1000

Information about New Publication:

University/Publisher:	Bogazici university
Title of dissertation/thesis:	Comprehensive Study of Simplified Models for Thermal Size Effects Induced by Localized Heating in Crystalline Solids
Author(s):	Amir Abdolhosseinzadeh
Expected completion date:	Aug. 2025

License Requestor Information

Name:	Amir Abdolhosseinzadeh
Affiliation:	Individual
Email Id:	amir.abdolhosseinzadeh@std.bogazici.edu.tr
Country:	Turkey

Figure C.14. Copyright permission for Figure 1.8.

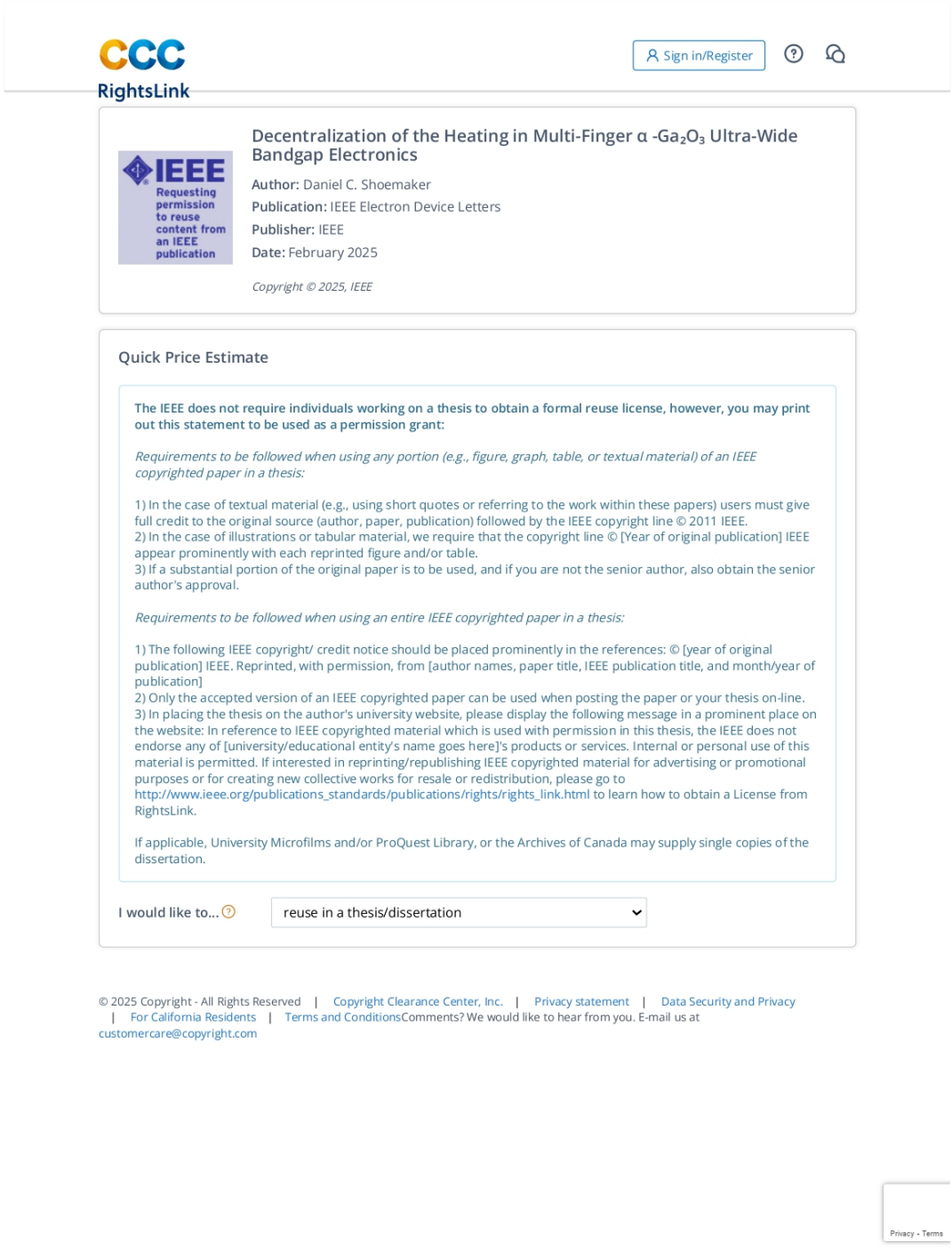

RightsLink

Sign in/Register

Decentralization of the Heating in Multi-Finger α -Ga_2O_3 Ultra-Wide Bandgap Electronics

Author: Daniel C. Shoemaker
Publication: IEEE Electron Device Letters
Publisher: IEEE
Date: February 2025

Copyright © 2025, IEEE

Quick Price Estimate

The IEEE does not require individuals working on a thesis to obtain a formal reuse license, however, you may print out this statement to be used as a permission grant:

Requirements to be followed when using any portion (e.g., figure, graph, table, or textual material) of an IEEE copyrighted paper in a thesis:

1) In the case of textual material (e.g., using short quotes or referring to the work within these papers) users must give full credit to the original source (author, paper, publication) followed by the IEEE copyright line © 2011 IEEE.
2) In the case of illustrations or tabular material, we require that the copyright line © [Year of original publication] IEEE appear prominently with each reprinted figure and/or table.
3) If a substantial portion of the original paper is to be used, and if you are not the senior author, also obtain the senior author's approval.

Requirements to be followed when using an entire IEEE copyrighted paper in a thesis:

1) The following IEEE copyright/ credit notice should be placed prominently in the references: © [year of original publication] IEEE. Reprinted, with permission, from [author names, paper title, IEEE publication title, and month/year of publication]
2) Only the accepted version of an IEEE copyrighted paper can be used when posting the paper or your thesis on-line.
3) In placing the thesis on the author's university website, please display the following message in a prominent place on the website: In reference to IEEE copyrighted material which is used with permission in this thesis, the IEEE does not endorse any of [university/educational entity's name goes here]'s products or services. Internal or personal use of this material is permitted. If interested in reprinting/republishing IEEE copyrighted material for advertising or promotional purposes or for creating new collective works for resale or redistribution, please go to http://www.ieee.org/publications_standards/publications/rights/rights_link.html to learn how to obtain a License from RightsLink.

If applicable, University Microfilms and/or ProQuest Library, or the Archives of Canada may supply single copies of the dissertation.

I would like to... reuse in a thesis/dissertation

© 2025 Copyright - All Rights Reserved | Copyright Clearance Center, Inc. | Privacy statement | Data Security and Privacy | For California Residents | Terms and ConditionsComments? We would like to hear from you. E-mail us at customercare@copyright.com

Figure C.15. Copyright permission for Figure 1.9.

American Physical Society
Reuse and Permissions License

13-Jul-2025

This license agreement between the American Physical Society ("APS") and Amir Abdolhosseinzadeh ("You") consists of your license details and the terms and conditions provided by the American Physical Society and SciPris.

Licensed Content Information

License Number:	**RNP/25/JUL/093426**
License date:	13-Jul-2025
DOI:	10.1103/PhysRevB.105.075301
Title:	Size effect and transient phonon transport mechanism in approach-to-equilibrium molecular dynamics simulations
Author:	Yufei Sheng et al.
Publication:	Physical Review B
Publisher:	American Physical Society
Cost:	USD $ 0.00

Request Details

Does your reuse require significant modifications: No

Specify intended distribution locations:	Turkey
Reuse Category:	Reuse in a thesis/dissertation
Requestor Type:	Student
Items for Reuse:	Figures/Tables
Number of Figure/Tables:	1
Figure/Tables Details:	FIG. 1.
Format for Reuse:	Print and Electronic
Total number of print copies:	Up to 1000

Information about New Publication:

University/Publisher:	Bogazici university
Title of dissertation/thesis:	Comprehensive Study of Simplified Models for Thermal Size Effects Induced by Localized Heating in Crystalline Solids
Author(s):	Amir Abdolhosseinzadeh
Expected completion date:	Aug. 2025

License Requestor Information

Name:	Amir Abdolhosseinzadeh
Affiliation:	Individual
Email Id:	amir.abdolhosseinzadeh@std.bogazici.edu.tr
Country:	Turkey

Figure C.16. Copyright permission for Figure 1.11.

ELSEVIER LICENSE
TERMS AND CONDITIONS

Jul 13, 2025

This Agreement between Amir Abdolhosseinzadeh ("You") and Elsevier ("Elsevier") consists of your license details and the terms and conditions provided by Elsevier and Copyright Clearance Center.

License Number	6067040604423
License date	Jul 13, 2025
Licensed Content Publisher	Elsevier
Licensed Content Publication	International Journal of Heat and Mass Transfer
Licensed Content Title	Extraction of thermal conductivity using phonon Boltzmann Transport Equation based simulation of frequency domain thermo-reflectance experiments
Licensed Content Author	Siddharth Saurav,Sandip Mazumder
Licensed Content Date	1 May 2023
Licensed Content Volume	204
Licensed Content Issue	n/a
Licensed Content Pages	1
Start Page	123871
End Page	0

Figure C.17. First page of copyright permission for Figure 1.12.

Type of Use	reuse in a thesis/dissertation
Portion	figures/tables/illustrations
Number of figures/tables/illustrations	1
Format	both print and electronic
Are you the author of this Elsevier article?	No
Will you be translating?	No
Title of new work	Comprehensive Study of Simplified Models for Thermal Size Effects Induced by Localized Heating in Crystalline Solids
Institution name	Bogazici university
Expected presentation date	Aug 2025
Portions	Fig. 9
The Requesting Person / Organization to Appear on the License	Amir Abdolhosseinzadeh
Requestor Location	Mr. Amir Abdolhosseinzadeh Boğaziçi Üniversitesi Güney Kampüsü Makina Mühendisliği Bölümü Istanbul, Besiktas 34342 Turkey
Publisher Tax ID	GB 494 6272 12
Total	0.00 USD

Figure C.18. Second page of copyright permission for Figure 1.12.

American Physical Society
Reuse and Permissions License

10-Jul-2025

This license agreement between the American Physical Society ("APS") and Amir Abdolhosseinzadeh ("You") consists of your license details and the terms and conditions provided by the American Physical Society and SciPris.

Licensed Content Information

License Number:	**RNP/25/JUL/093348**
License date:	10-Jul-2025
DOI:	10.1103/PhysRevB.105.165303
Title:	Hydrodynamic thermal transport in silicon at temperatures ranging from 100 to 300 K
Author:	Albert Beardo et al.
Publication:	Physical Review B
Publisher:	American Physical Society
Cost:	USD $ 0.00

Request Details

Does your reuse require significant modifications: No

Specify intended distribution locations:	Turkey
Reuse Category:	Reuse in a thesis/dissertation
Requestor Type:	Student
Items for Reuse:	Figures/Tables
Number of Figure/Tables:	1
Figure/Tables Details:	Fig. 2.
Format for Reuse:	Print and Electronic
Total number of print copies:	Up to 1000

Information about New Publication:

University/Publisher:	Bogazici university
Title of dissertation/thesis:	Comprehensive Study of Simplified Models for Thermal Size Effects Induced by Localized Heating in Crystalline Solids
Author(s):	Amir Abdolhosseinzadeh
Expected completion date:	Aug. 2025

License Requestor Information

Name:	Amir Abdolhosseinzadeh
Affiliation:	Individual
Email Id:	amir.abdolhosseinzadeh@std.bogazici.edu.tr
Country:	Turkey

Figure C.19. Copyright permission for Figure 1.14.